Universidad de Las Palmas de Gran Canaria | *Universitat de les Illes Balears* | *Université de Liège (coordinateur)* | *Université de Bretagne Occidentale Brest* | *Université de Corse Pascal Paoli*

Université Pierre et Marie Curie Paris VI | *Universidade Nova de Lisboa* | *Universitat Politècnica de Catalunya* | *Universidade Tècnica de Lisboa*

Diplôme d'études approfondies européen en modélisation de l'environnement marin

SOCRATES/ERASMUS

Simulation of annual cycles of phytoplankton, zooplankton and nutrients using a mixed layer model coupled with a biological model

Charles Troupin

2005 - 2006

Diploma Eruditionum Altarum

DEA

europaeum

Universidad de Las Palmas de Gran Canaria | *Universitat de les Illes Balears* | *Université de Liège (coordinateur)* | *Université de Bretagne Occidentale Brest* | *Université de Corse Pascal Paoli*

Université Pierre et Marie Curie Paris VI | *Universidade Nova de Lisboa* | *Universitat Politècnica de Catalunya* | *Universidade Tècnica de Lisboa*

Diplôme d'études approfondies européen en modélisation de l'environnement marin

SOCRATES/ERASMUS

Simulation of annual cycles of phytoplankton, zooplankton and nutrients using a mixed layer model coupled with a biological model

---

Charles Troupin

2005 - 2006

Diploma Eruditionum Altarum

DEA

europaeum

Committee members

Dr. Pablo Sangrà Inciarte (promotor),
Universidad de Las Palmas de Gran Canaria
Prof. Jean-Marie Beckers, Université de Liège
Prof. Éric Delhez, Université de Liège
Dr. Joaquin Tintoré Subirana,
Universitat de les Illes Balears

Abstract

In oceanography, the *mixed layer* refers to the near surface part of the water column where physical and biological variables are distributed quasi homogeneously. Its depth depends on conditions at the air-sea interface (heat and freshwater fluxes, wind stress) and on the characteristics of the flow (stratification, shear), and has a strong influence on biological dynamics.

The aim of this work is to model the behaviour of the mixed layer in waters situated to the south of Gran Canaria island, as well as the annual biological cycles (nutrients, planktons, detritus) which depend on it.

To this end the one dimensional version of the ROMS (*Regional Ocean Modelling System*) model is applied. The model consists of a physical model coupled with a biological one, with a mixed layer sub-model (*K-Profile Parameterization*).

Initialization is done using mean profiles established from *in situ* data, forcing is from monthly means of heat fluxes, surface temperature, wind stress and heat flux sensitivity to sea surface temperature. These physical parameters are extracted from climatic databases and averaged over a 10-year period. Their annual variations are interpreted in order to physically predict the resulting behaviour of the mixed layer.

The model is tested by means of a sensitivity analysis with respect to the forcing conditions, as well as through a comparison with other models for the case of idealized situations.

Simulations are then performed, underlining, in summer, a strong stratification and a shallow mixed layer under the effect of the important heat fluxes; in late winter, a deep mixed layer due to convective mixing, causing an injection of nutrients into the *euphotic layer* and a phytoplankton bloom in February. *Sverdrup critital depth* theory is applied in the interpretation of these observations.

Finally the model validation is achieved either through *in situ* data, or through climatic data, bringing to light a qualitative and quantitative agreement between model results and reality, for the physical variables as well as the biological ones.

Résumé

En océanographie, la *couche de mélange* désigne la partie de la colonne d'eau proche de la surface et dans laquelle les variables physiques et biologiques sont distribuées de manière quasi-homogène. Sa profondeur dépend des conditions à l'interface air-mer (flux de chaleurs et d'eau douce, tension du vent) et des caractéristiques de l'écoulement (stratification, cisaillement), et a influence importante sur la dynamique biologique.

L'objectif de ce travail est de modéliser le comportement de cette couche de mélange dans les eaux situées au sud de l'île de Gran Canaria, ainsi que les cycles annuels biologiques (nutriments, planctons, détritus) qui en dépendent.

À cet effet la version à une dimension du modèle ROMS (*Regional Ocean Modelling System*) est utilisée. Elle consiste en un modèle physique couplé à un modèle biologique, avec un sous-modèle de couche de mélange (*K-Profile Parameterization*).

L'initialisation est réalisée à partir de profils moyens construits grâce à des données *in situ*, le forçage à partir de moyennes mensuelles de flux de chaleur, de température de surface, de tension du vent et de sensibilité du flux de chaleur net par rapport à la température de surface. Ces grandeurs physiques sont extraites de bases de données climatiques et moyennées sur une période de dix ans. Leurs variations annuelles sont interprétées de manière à prédire physiquement le comportement de la couche de mélange qui en résulte.

Le modèle est testé par une analyse de sensibilité par rapport aux conditions de forçage ainsi que par une comparaison avec d'autres modèles dans le cas de situations idéalisées.

Les simulations sont ensuite effectuées, mettant en évidence, en été, une forte stratification et une couche de mélange peu profonde sous l'effet des importants flux de chaleur; à la fin de l'hiver, une couche de mélange profonde due au mélange convectif, provoquant une injection de nutriments dans la *couche euphotique* et un bloom de phytoplancton en février. La théorie de la *profondeur critique de Sverdrup* est appliquée pour interpréter ces observations.

Enfin, la validation du modèle est réalisée d'une part grâce à des données *in situ*, d'autre part grâce à des données climatiques, révélant un accord qualitatif et quantitatif entre les résultats du modèle et la réalité, aussi bien pour les variables physiques que biologiques.

Aknowledgements

With these few lines, I would like to give my sincere thanks to the people who make possible I wrote all the other lines of this work:

The two persons who helped me to carry out this overseas project: Dr. Salim Djenidi, who made contacts with my promotor and solved all the practical problems I could encounter through the preparation of this work, and Prof. Pablo Sangrà Inciarte, who accepted to receive me at the University of Las Palmas de Gran Canaria, made me feel at home in the physics department, and supervised me with interest during several months.

My friends, colleagues and professors at the University of Liège, for giving me the taste of physics in general and of environment modelling in particular. I cannot name them all here, but I am sure they will recognize themselves.

The Socrates-Erasmus program, which each year allows numerous students to live a rewarding experience and provides useful funding.

My friends I always felt by my side, disregarding thousands of kilometres between us.

Finally, my whole family, who brought me all the support I needed during these months and gave me to opportunity to carry on my studies abroad. Without them, I know that all this adventure would have stayed a dream.

Agradecimientos

Con estas pocas líneas, quería dar las gracias a toda la gente que hizo posible que escribiese todas las otras líneas de este trabajo:

A las dos personas que me ayudaron con este proyecto en el extranjero: Dr. Salim Djenidi, quien contactó con mi promotor y solucionó todos los problemas prácticos que me han podido surgir durante la preparación de este trabajo, y Prof. Pablo Sangrà Inciarte, que aceptó acogerme en la Universidad de Las Palmas de Gran Canaria; me hizo sentir como en casa, y quien además me supervisó con gran interés durante toda mi estancia.

Mis amigos, compañeros de trabajo y profesores de la Universidad de Lieja, quienes me mostraron lo interesante que es la física en general y la modelización del medio ambiente en particular. No puedo nombrar a todos, pero estoy seguro que ellos se reconocerán.

Al programa Sócrates-Erasmus, que cada año permite que numerosos estudiantes vivan esta provechosa experiencia y proporciona un fondo útil.

A mis amigos, que siempre he sentido a mi lado, a pesar de los miles de kilómetros entre nosotros.

Por fin, a toda mi familia, que me dio el apoyo necesario y la oportunidad de seguir mis estudios en el extranjero. Sin ellos, sé que toda esta aventura habría quedado en un sueño.

To our friend Jean Portier, who introduced us to the physics of turbulence with enthusiasm and patience, but unfortunately left us too early.

Contents

Chapter 1

INTRODUCTION

1.1 Aim of the study

The main purpose of this work is to model the annual behaviour of the ocean surface layer and the cycle of phytoplankton, zooplankton and nutrients to the south of Gran Canaria island with to ROMS 1D model.

Chapter 2 introduces the model and its physical, biological and numerical components. The mixing scheme is examined in details, in order to display the physical processes under the numerous equations.

In chapter 3, more practical aspects of the model are treated, as we establish the initialization and the forcing through the boundary conditions. The main features of the climatic context are also outlined, preparing the way to the results interpretation.

We then perform testing and sensitivity analysis in chapter 4: testing is carried out with idealized experiment (wind deepening, heating/cooling), in order to compare the temporal evolution of the mixed layer with results brought by other models; the sensitivity is analysed by perturbing the forcing parameters one after each other and examining the corresponding variation of the mixed layer.

Once this preliminary work is done, we simulate the behaviour of the physical (temperature, salinity, mixed layer depth) and biological (nitrate, ammonium, phytoplankton, zooplankton, large and small detritus, chlorophyll a and oxygen) in chapter 5.

Chapter 6 is dedicated to the model validation, by means of comparisons with *in situ* vertical profiles from cruises in the studied region and with data we could extract from oceanographic databases and from the literature.

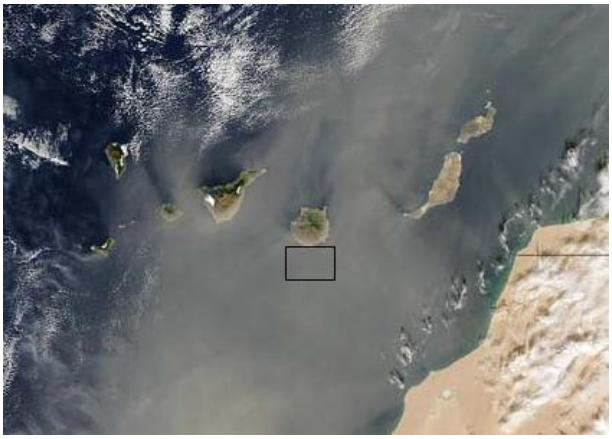

Figure 1.1: *Localisation of the region of interest for the simulations.*

1.2 Physical and biological contexts

As the present work consists only in the study of the properties of a water column with the help of a one-dimension model, we limit ourselves to present the main features of the physical and biological processes that occur in the archipelago.

1.2.1 Atmospheric and oceanic backgrounds

Large scale

The region of interest shows two large-scale mean flows: the *Canary Current* and the *Trade Winds*.

The Canary Current is the eastern boundary current of the North Atlantic subtropical gyre (fig.1.2). It flows southward along the coast of Africa from Morocco to Mauritania and is associated with coastal upwelling [1]. This current flows with a predominantly southwestward direction through the Canaries archipelago, with mean speeds of $0.05\,m/s$.

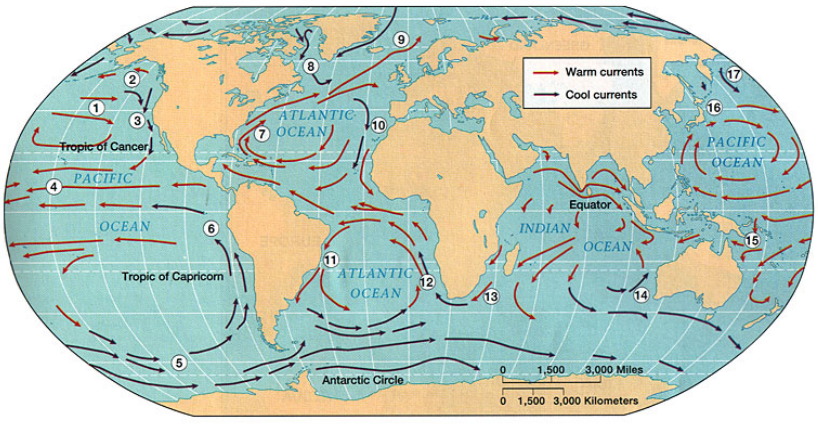

Figure 1.2: *Oceanic surface circulation.*

The Trade Winds are north-easterly in the Northern Hemisphere, where they begin as north-northeast winds at about latitude $30°N$ in January and latitude $35°N$ in July,

[1] Source: American Meteorological Society Glossary of Meteorology

gradually veering to northeast and east-northeast as they approach the equator. Their southern limit is a few degrees north of the equator. They are characterized by great constancy of direction and, to a lesser degree, speed [1].

In the Canary region, they have a well defined seasonal periodicity, with maximum intensity during spring and summer and average value between 5 and 10 m/s.

Mesoscale

Regions in the south of the islands are wind-sheltered, leading to presence of warm wakes, observable in sea surface temperature satellite images. These warm wakes have an extent of many tens of kilometres [Basterretxea et al. (2002)].

Moreover, the perturbation of the Canary Current by the presence of the islands generates eddies in the wake of the obstacle (fig. 1.3) [Arístegui et al. (2004), Sangrà (1995)].

Here are the characteristic values for the eddies in the wake of Gran Canaria:

- size comparable to the Gran Canaria radius (50 km),
- depth up to several hundred meters,
- period between two eddies ranging between several days and a few weeks (based on satellite and field observations) [Arístegui et al. (1994)],
- can last more than seven months.

Figure 1.3: *Von Kármán Vortex street generated in the wake of the islands.*

Another significant feature is the presence of coastal upwelling filaments, able to export organic matter from the African coast into the surface Canary waters [Barton et al. (1998)].

Climatic characteristics

The climate in the south of the islands is characterized by weak precipitations through to whole year, with a maximum in winter. Trade Winds have their maximal intensity in summer.

The climatic background will be considered in details in the section 3.3.

1.2.2 Biology

The waters around the Canaries archipelago are typically oligotrophic [1]. Mean chlorophyll concentrations are low ($< 0.5\, mg\, Chl\, m^{-3}$) for most of the year [Arístegui et al. (1997)].

An interesting topic is the coupling between the physical and the biological processes. For instance, we can mention:

- the existence of seasonal sharp thermocline, which limits the vertical flux of nutrients from deep waters to the euphotic zone, then limiting phytoplankton growth;
- the thermocline weakening during winter time, as the result of surface cooling. During this short convective mixing period takes place the *phytoplankton bloom*: mixing makes nutrients available for the phytoplankton, which can grow faster and build up a biomass pool [Arístegui et al. (2001)];
- the pump of nutrients into the surface waters due to the Island cyclonic eddies, creating large mesoscale variability in the archipelago region. This mesoscale variability may influence the distribution and productivity of plankton communities [Arístegui et al. (1997)].

1.3 The mixing processes

The general purpose of a model is to only consider the relevant factor of a determinate phenomenon in order to simplify it to the maximum. In this section we want to concentrate on the ingredients necessary to model the mixing process, without writing any equations.

Mixing generation

The main question to be answered is the following:

What could induce (or inhibit) a mixing of the fluid?

Wind

The wind is acting directly on the air-sea interface by transferring momentum from the atmosphere to the ocean, causing two major effects: firstly, the shearing, which consist of a variation of the current velocity with respect to the depth; secondly, the generation of surface waves, whose period and amplitude will depend on the intensity of the wind and the area where it blows.

[1] From the Greek *Oligo*: small, little, few; and *trophe*: nutrients, food. Refers to water lacking in plant nutrients and having a large amount of dissolved oxygen throughout.

Waves breaking

Waves breakings constitute a mechanical mean of mixing that enhances the air-sea exchanges (fig. 1.4):

- bubbles of air are brought into the sea,
- spray and droplets are thrown into the air,
- turbulence and mixing are enhanced by an energy input.

Figure 1.4: *Mixing by wave breaking.*

Convection

The *convection* is the process by which a fluid particle undergoes a movement whose origin is a difference between its density and the density of the surrounding fluid. Thus, to find what is responsible for convection, we have to look for phenomenons that are able modify the local density of the fluid.

- a heat supply,
- a freshwater supply, which can arise from precipitations or supply from a river,
- local temperature and salinity variations.

Heating, induced by the sun, will increase the fluid temperature near the surface and decrease its density, preventing the fluid to sink. We can then expect the convection to have a diurnal cycle, with a destabilizing step taking place during the night and a stabilizing step during the day.

Stratification

In a homogeneous fluid, a modification of the fluid particle density will result in a vertical motion due to the buoyancy: the particle will either ascend or sink. But in more realistic situation, density varies with depth and creates situation favourable or unfavourable to these vertical motions.

Typically, it can be shown that in the case of a stably stratified fluid, *i.e.* the density increases with depth, a particle will undergo an oscillating motion, of which the frequency is directly related to the stratification.

We can easily figure out that a particle immersed in a more dense fluid will need more energy to a downward motion. Eventually, we conclude that stratification will act either as a brake or as an enhancement of the mixing process, thus it will have to be taken into account in the mixing model.

1.3.1 Importance of mixing processes

Mixing is related to many other important processes:

- the exchange of mass, momentum, energy and heat between the atmosphere and the ocean;
- mixing due to wind forcing, inducing upwelling with nutrient rich water. This nutrient supply may create a phytoplankton grow, followed by an increase in zooplankton concentration, finally leading to a fish abundance;
- in the carbon cycle: the carbon is fixed in the oceanic mixed layer by the organisms;
- in acoustic: the wave propagation is affected by vertical gradient of T, so that the mixed layer modifies the characteristics of sound transmission.

1.4 The oceanic mixed layer (OML)

Since one of the main purposes of the present work is to simulate the behaviour of the OML, the description of its properties and structure will allow us to build the physical background necessary to understand its modelling.

1.4.1 Definition and characteristics of the OML

The OML is a region adjacent to the air-sea interface, which responds directly to surface forcing [Kantha (2000)] and characterized by the presence of a well-mixed fluid, *i.e.* the temperature and salinity variations are fairly uniform from the surface down to a depth generally ranging from 10 to 200 meters. Below it are found rapidly changing regions of temperature, salinity and density: the thermo-, halo- and pycno-clines.

It is mixed from both the top and the bottom:

- at the top, mixing is achieved by wind stress, waves breaking and buoyancy flux,
- at the bottom, large eddies create entrainment that mixes the denser fluid from below into the OML.

1.4.2 OML structure

The OML can be divided into four parts [Kantha (2000)]:

1. the molecular sublayer ($\mathcal{O}(1\,mm)$): it is a skin layer through which properties are exchanged via molecular processes.
2. the wave sublayer ($\mathcal{O}(2-6\,m)$): in this region, the turbulent processes dominate, driven by momentum and energy exchange between the atmosphere and the ocean.
3. the main bulk ($\mathcal{O}(10-40\,m)$).
4. the interfacial layer or entrainment sublayer ($\mathcal{O}(5-10\,m)$), where large eddies are acting and generating entrainment.

1.4.3 Modelling the OML

Modelling the evolution of the mixed layer under the influence of external forcing is an essential part of this work. As we have seen previously, many factors may play a role in the process. is to have a model which reaches a compromise between the physics reality and numerical limitations in the resolution of the equations.

Actually two kinds of mixed layer models exist: the *integrated* ones, and the *bulk* ones. We present here their characteristics.

Integrated (slab) models

The governing equations are integrated over the mixed layer depth, so that the momentum and heat balances of the entire MLD under the action of momentum and buoyancy fluxes at the ocean surface can be considered. The problem consists in parameterizing entrainment deepening and shallowing in terms of surface momentum and buoyancy flux. The entrainment parameters need to be adjusted for different situation, no universal parameterization exists.

Among these slab models, we can mention:

- the shear instability model: when strongly sheared, the buoyancy interface becomes instable, turbulence is generated and the ML deepens just enough to restore neutral stability, dictated by a *bulk Richardson number* criterion, to the interface,

$$\mathrm{Ri}_b = \frac{\Delta\rho g\, h}{\rho_w(\Delta U_j \Delta U_j)} \geq \mathrm{Ri}_{cr.},$$

  the problem consisting in determining an appropriate value for $\mathrm{Ri}_{cr.}$.

- the Miles-Howard criterion for a sheared stably stratified flow, bringing into play a *gradient Richardson number* (also see section 2.2.3):

$$\mathrm{Ri}_g = \frac{\frac{\partial b}{\partial z}}{\left(\frac{\partial u}{\partial z}\right)^2 + \left(\frac{\partial v}{\partial z}\right)^2} \geq 0.25$$

- the convective adjustment, which restores neutral stability to the fluid in the mixed layer under the action of surface buoyancy destabilizing flux:

$$\frac{\partial \rho}{\partial z} \geq 0.$$

Diffusion (or differential) models

In the diffusion models, the turbulent mixing and diffusion in the MLD are directly parameterized, meaning that the governing equation are kept under their differential form. This parameterization can come from theorical and observational knowledge of the surface layers and contain empirical or semi-empirical formulation for turbulent diffusion, or can be based on modelling of turbulence quantities by appealing to turbulence at the second or the third moment level [Kantha (2000)].

Among models of this category, we can cite:

- the $k-\omega$ model [Kolmogorov (1942], which deals with the turbulent kinetic energy k and ω, defined as the rate of dissipation of energy per unit volume and time. These two variables are determined by resolving two partial differential equations.
- the $k-\varepsilon$ model [Jones and Launder (1972)], which uses two partial differential equations for k, and ε, the turbulence dissipation rate.
- the *Mellor-Yamada level 2.5 closure scheme* [Mellor and Yamada (1974)]: this model computes the vertical eddy viscosity and diffusivity as

$$\begin{aligned} K_v &= \sqrt{2k}\,\ell\, S_M \\ K_\rho &= \sqrt{2k}\,\ell\, S_H, \end{aligned}$$

  where k is the turbulent kinetic energy, ℓ is a limited turbulent length scale, ρ is potential density, and S_M and S_H are stability functions for momentum and scalars.

  The variables k and $k\ell$ are obtained by resolving a set of two partial differential equations. The MLD is computed as the depth where the local turbulent kinetic energy reaches a predetermined value.

A comparison of turbulence closure models can be found in [Warner et al. (2005)].

Chapter 2

Description of the ROMS 1D model

R.O.M.S. stands for Regional Ocean Modelling System. It is a free-surface, hydrostatic, primitive equation ocean model that uses stretched, terrain-following coordinates in the vertical and orthogonal curvilinear coordinates in the horizontal. This model was developed at the U.C.L.A. to study the California current. It is now used in a large range of applications, from regional to basin and even global simulations. For further details about the model, [Marchesiello et al. (2001)], [Shchepetkin and McWilliams (2005)] can be consulted.

The one-dimension model [1] used is the present work is derived from the previous one: the mixing closure sub-model, the treatment of vertical advection and diffusion are compatible with the UCLA ROMS 3D model [Penven].

This section is dedicated to describe the model as provided on the website. In the chapter 5, we will make a few modifications in order to be closer to the real conditions of the Canary Islands region. We successively describe the physical, mixing closure and biological models.

2.1 The physical model

The model is one-dimensional, *i.e.* horizontal variations are neglected. Mathematically, this assumption means that partial derivatives with respect to the horizontal coordinates vanish:

$$\boxed{\frac{\partial .}{\partial x} = 0, \quad \frac{\partial .}{\partial y} = 0}$$

with the $x-$, and $y-$axes directed eastward and northward, respectively.

The equations are written in a cartesian frame, assuming *hydrostatic* and *f-plane approximations*. The hydrostatic approximation is valid if the vertical length scale is negligible with respect to the horizontal length scale and results in the balance between the vertical gradient of pressure and the term $-\rho\, g$. The f-plane approximation consists in assuming a constant value for the Coriolis parameter and is hence valid when displacements in the northward direction are not too large.

[1] Available at `http://www.brest.ird.fr/personnel/ppenven/roms1d/index.html`.

Continuity equation

The continuity equation expresses the mass conservation in a continuum and can be written as

$$\frac{\partial \rho}{\partial t} + \frac{\partial \rho\, u}{\partial x} + \frac{\partial \rho\, v}{\partial y} + \frac{\partial \rho\, w}{\partial z} = 0,$$

where ρ is the water volumic mass and (u, v, w) are the eastward, northward and upward components of the velocity, respectively. Without horizontal variations and considering an incompressible fluid, the previous equation reads:

$$\frac{\partial w}{\partial z} = 0 \tag{2.1}$$

This velocity is null at the bottom and hence null for any depth:

$$\boxed{w = 0.}$$

Momentum equations

An important consequence of the one-dimensional assumption is that the advective terms vanishes. This fact will have to be remembered when we will have to discuss the results. With all the hypothesis previously mentioned, the momentum equation is reduced to the balance between the following terms:

$$\boxed{\text{Temporal derivative} = \text{Coriolis force} + \text{diffusion},}$$

which in our case is expressed by

$$\frac{\partial u}{\partial t} = f v + \frac{\partial}{\partial z}\left(K_M \frac{\partial u}{\partial z}\right) \tag{2.2}$$

$$\frac{\partial v}{\partial t} = -f u + \frac{\partial}{\partial z}\left(K_M \frac{\partial v}{\partial z}\right) \tag{2.3}$$

$$\frac{\partial p}{\partial z} = -\rho\, g \tag{2.4}$$

where u and v are the horizontal components of the velocity, $f = 2\,\Omega \sin(latitude)$ is the Coriolis parameter, K_M is a vertical turbulent mixing coefficient, g is the gravity acceleration.

Equations for the tracers

The equations for the potential temperature of the ocean T and the salinity S are

$$\frac{\partial T}{\partial t} = w^* \frac{\partial T}{\partial z} + \frac{\partial}{\partial z}\left(K_T \frac{\partial T}{\partial z} - \gamma\right) + \frac{T_{ref} - T}{\tau} \tag{2.5}$$

$$\frac{\partial S}{\partial t} = w^* \frac{\partial S}{\partial z} + \frac{\partial}{\partial z}\left(K_S \frac{\partial S}{\partial z} - \gamma\right) + \frac{S_{ref} - S}{\tau} \tag{2.6}$$

where K_T and K_S are two other vertical turbulent mixing coefficients, defined by the *KPP vertical turbulent closure scheme* (see section 2.2); γ is a non-linear transport term in addition to the down-gradient component.

T_{ref} and S_{ref} are respectively the potential temperature and the salinity towards which the temperature and the salinity are relaxed, and τ is the nudging relaxation time towards data.

w^* is a vertical velocity to take into account the effects of a possible upwelling (see section 2.1.1). This velocity is obviously artificial, since the continuity equation told us that $w = 0$.

State equation

The density ρ is expressed as a function of P, T and S through the equation of state of sea water:

$$\rho = F(P, T, S) \tag{2.7}$$

The model allows us to choose between linear (2.8) or non-linear (2.9) formulations, the latter being taken from [Jackett and McDougall (1995)]:

$$\rho = \rho_0 \left[1 - \alpha(T - T_0) + \beta(S - S_0)\right] \tag{2.8}$$

$$\begin{aligned}
\rho &= 999.842594 + 6.793952\,10^{-2}T - 9.095290\,10^{-3}T^2 + 1.001685\,10^{-4}T^3 \\
&- 1.120083\,10^{-6}T^4 + 6.536332\,10^{-9}T^5 + S\left(0.824493 - 4.08990\,10^{-3}T\right. \\
&+ \left. 7.64380\,10^{-5}T^2 - 8.24670\,10^{-7}T^3 + 5.38750\,10^{-9}T^4\right) \\
&+ +\sqrt{S}\left(-5.72466\,10^{-3} + 1.02270\,10^{-4}T - 1.65460\,10^{-6}T^2\right. \\
&+ \left. 4.8314\,10^{-4}S\right)
\end{aligned} \tag{2.9}$$

2.1.1 Boundary conditions

Analytical formulation

The boundary conditions express the continuity of the fluxes (stress, heat and salinity) at the air-sea interface and at the bottom.

- At the top of the water column ($z = 0$), we have:

$$K_M \frac{\partial u}{\partial z} = \tau^x_{surf} \tag{2.10a}$$

$$K_M \frac{\partial v}{\partial z} = \tau^y_{surf} \tag{2.10b}$$

$$K_T \frac{\partial T}{\partial z} = \frac{Q_T}{\rho_0 C_p} \tag{2.10c}$$

$$K_S \frac{\partial S}{\partial z} = \frac{(E - P)S}{\rho_0} \tag{2.10d}$$

where $(E - P)$ is the evaporation minus the precipitation, τ^x_{surf} and τ^y_{surf} are the surface wind components, Q_T is the surface heat flux and C_p is the heat capacity at constant pressure.

- At the bottom ($z = -h$):

$$K_M \frac{\partial u}{\partial z} = \tau^y_{bot} = 0 \quad (2.11a)$$

$$K_M \frac{\partial v}{\partial z} = \tau^y_{bot} = 0 \quad (2.11b)$$

$$K_T \frac{\partial T}{\partial z} = 0 \quad (2.11c)$$

$$K_S \frac{\partial S}{\partial z} = 0 \quad (2.11d)$$

  with τ^x_{bot} and τ^y_{bot}, the bottom stress components, here set to zero.

Forcing of the model

As we have seen previously, boundary conditions are required to solve the model equations. They constitute the external forcing, performed via the following parameters:

- The surface momentum stress $[N/m^2]$: stress generated by the action of wind on the surface of the ocean, generally computed from the wind speed above the surface.
- The surface net heat flux $[W/m^2]$: total quantity of heat that gets to the air-sea interface, equal to the sum of four heat flux: latent, sensible, long wave and short wave.
- The surface freshwater flux $[cm/day]$: difference between evaporation and precipitation rates.
- the sea surface temperature [° C].
- the solar shortwave radiation $[W/m^2]$: solar incident radiation emitted in the visible and near-ultraviolet wavelengths.
- the surface net heat flux sensitivity to SST $[W/(m^2\,°C)]$: see section 3.3.6 page 43.
- the upwelling index $[m^3/s]$: index used to compute the vertical velocity w^* to take into account an upwelling effect that could bring tracers towards the surface. As we will not use this type of forcing, no further description will be made. Details can be found on the ROMS 1D model documentation [Penven].

The model runs with monthly data, which are interpolated linearly to get the forcing at each time step. The temporal mean of the heat and salinity fluxes are removed in order to obtain a yearly cyclic solution. A diurnal cycle is added to the solar short-wave radiation flux as a function of the latitude. These forcing parameters will be described in details in the chapter 3.

To illustrate how the forcing is performed concretely, we present here an example of a *forcing file* [2]: it is the kind of file through which the model forcing is achieved.

[2] This file is provided with the source code.

Forcing file 2.1 Data of a simulation in the Monterey Bay.

```
LONGITUDE= -122.2015   LATITUDE=   36.6835

SUSTR "surface u-momentum stress" "Newton meter-2"
    0.0130     0.0172     0.0307     0.0295     0.0349     0.0330
    0.0279     0.0249     0.0202     0.0151     0.0117     0.0085

SVSTR "surface v-momentum stress" "Newton meter-2"
   -0.0367    -0.0458    -0.0756    -0.0960    -0.1190    -0.1114
   -0.1024    -0.0851    -0.0719    -0.0632    -0.0459    -0.0361

SHFLUX "surface net heat flux" "Watts meter-2"
  -50.9245   -13.6624    27.0241    88.0957   137.0854   165.5644
  157.3836   124.3749    83.8437    24.9804   -28.1684   -59.4854

SWFLUX "surface freshwater flux (E-P)" "centimeter day-1"
   -0.0098    -0.0083     0.0340     0.0664     0.1059     0.0791
    0.0837     0.0847     0.0847     0.0803     0.0423     0.0060

SST "sea surface temperature" "Celsius"
   12.2561    12.1035    12.0097    11.8934    12.2891    13.1019
   13.8605    14.6821    15.2700    14.9239    14.0310    13.0777

DQSST "surface net heat flux sensitivity to SST" "Watts meter-2 Celsius-1"
  -34.5228   -34.2731   -36.8135   -35.1935   -35.7558   -35.1404
  -34.4302   -34.8325   -33.3956   -33.6455   -33.9390   -34.8636

SWRAD "solar shortwave radiation" "Watts meter-2"
   83.5423   116.0422   171.5213   227.1354   265.5645   281.2076
  262.2105   231.7137   198.0894   146.2076    99.2749    75.3418

UPWI "upwelling indice" "m3 s-1"
    3.63      22.41      70.80     142.00     214.74     244.06
  210.56     183.17     100.46      50.50      17.89       5.30
```

2.1.2 Initial conditions

Originally, the profiles of salinity and temperature are set analytically in the source code, with relations based on CalCOFI[3] mean profile. The conditions in the South Canaria area are totally different from the California area, so we have to work with typical data for the region of interest. That is what we will do in section 3.2.

Concerning the other variables, constants values are imposed over the water column:

- The initials velocities are set to zero.
- The initial value for the vertical mixing coefficient for momentum (K_M) is $0.01\,m^2/s$.
- The vertical mixing coefficients for salinity (K_S) and temperature (K_T) are taken equal to $0.001\,m^2/s$.

2.1.3 The vertical grid

The model use stretched vertical coordinate system to allow the increase of resolution near the surface boundary layer (fig. 2.1). The grid is *staggered*, *i.e.* the vertical velocity is defined at different localisations (z_w) than the tracers (z_ρ), according to

[3] California Cooperative Oceanic Fisheries Investigations

$$z_\rho(i) = -h\frac{\sinh\left(\theta_s\frac{N-i+0.5}{N}\right)}{\sinh(\theta_s)}, \qquad i=\{1,2,\ldots,N\}$$
$$z_w(i) = -h\frac{\sinh\left(\theta_s\frac{N-j}{N}\right)}{\sinh(\theta_s)}, \qquad i=\{0,1,\ldots,N\}$$

with

- N, the number of vertical layers,
- h, the total depth and
- θ_s, a parameter controlling the stretching of the grid: an increasing value of θ_s increases the resolution near the surface.

The height of the layer i is thus given by

$$H_z(i) = N\left(z_w(i) - z_w(i-1)\right), \qquad i=\{1,2,\ldots,N\}$$

The following figures show the position of the z_w points and of the z_ρ points and the influence of the parameter θ_s for a 100-meter depth domain with 10 vertical layers.

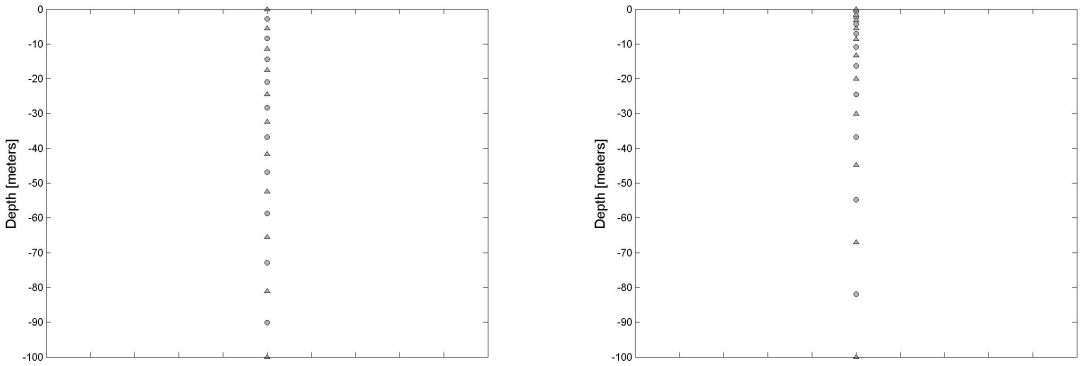

(a) $\theta_s = 2$ (b) $\theta_s = 4$

Figure 2.1: *The vertical stretched grid: triangle indicates positions of the w−points, circles indicate positions of the tracer-points.*

2.1.4 Nudging

This technique is commonly used to correct models trajectories by adding a term proportional to the difference between model results and observations.

In this model, temperature, salinity and nitrates are relaxed towards their initial values [see equations (2.5) and (2.6)] with a relaxation time given by $\tau = 2 + 23\,e^{\frac{z}{100}}$. The value of the time relaxation is 25 years at the surface and around 10 years at a depth of 100 meters (fig. 2.2).

Nudging may be used to account for processes which the one-dimension model is unable to deal with, *i.e.* horizontal advection in diffusion.

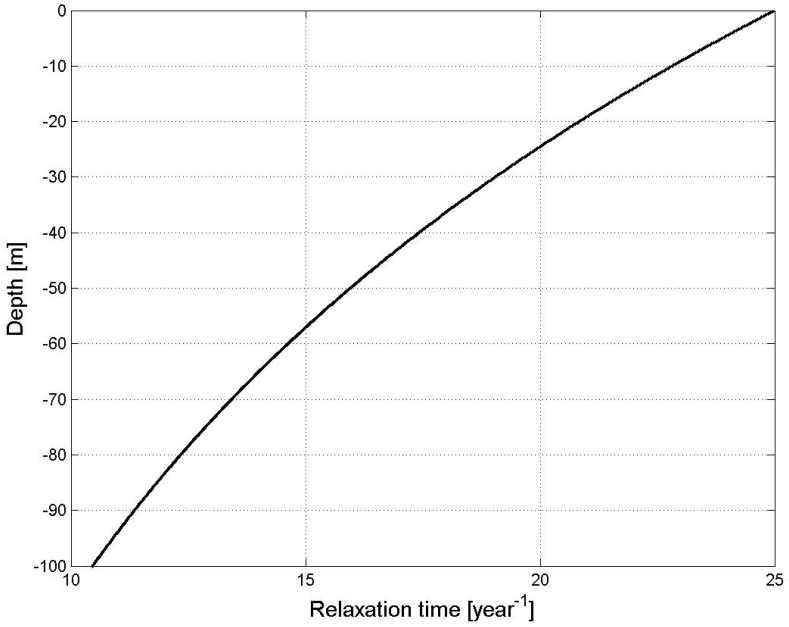

Figure 2.2: *Time relaxation in function of depth.*

2.2 The mixing closure sub-model

In this section we describe the *K profile parameterization* (KPP) boundary layer scheme [Large et al. (1994)], which is the mixing closure model used here to parameterize the small-scale processes. This scheme belongs to the diffusion models category (see section 1.4).

It was designed to be consistent with the similarity theory (section 2.2.1) and to represent the two different regimes we can distinguish in the ocean:

1. near the surface, under the surface forcing conditions;
2. the interior, where internal waves, shear instability and double diffusion occur;

This model is qualified as *nonlocal*, meaning that local fluxes not only depend on local properties and gradients, but also on boundary layer parameters, such as surface fluxes and boundary layer depth.

2.2.1 Monin-Obukhov similarity theory

The *Monin-Obukhov theory* is a relationship describing the vertical behaviour of non-dimensionalized mean flow and turbulence properties in the surface boundary layer as a function of key parameters.

This theory says that the only important turbulence parameters are d, the distance from the boundary, and $\overline{wx}_0$, the surface kinematic fluxes. With these parameters, the following fundamental turbulent parameters are constructed:

$$u^{*2} = (\overline{wu}_0^2 + \overline{wv}_0^2)^{1/2} = \frac{|\tau_0|}{\rho_0} \tag{2.12}$$

$$S^* = -\frac{\overline{ws}_0}{u^*} \tag{2.13}$$

$$L = \frac{u^{*3}}{\kappa B_f} \tag{2.14}$$

with $\boldsymbol{\tau}_0$ the surface wind stress vector, ρ_0 the surface density, κ the von Kármán constant and B_f is the *buoyancy flux*. u^* is called the *turbulent frictional velocity*, S^* the *turbulent flux scale* for the generalized scalar S (salinity, potential temperature, velocity components, ...) and L the *Monin-Obukhov length scale*.

The buoyancy flux may be considered as a number that summarizes the processes affecting the surface density and whose sign indicates if this surface density generates a stable or an unstable situation:

$$B_f = g\left[\alpha\, Q_{total} - \beta(E-P)S - \frac{\alpha\, I\, h}{\rho\, C_p}\right], \tag{2.15}$$

with
g, the gravitational acceleration,
Q_{total}, the total heat flux,
α, the thermal expansion coefficient,
β, the haline contraction coefficient
$(E-P)$, the freshwater flux (evaporation minus precipitation),
I, the net surface irradiance and
C_p the heat capacity at constant pressure.

With the use of these scales, all surface-layer flow properties can be expressed as dimensionless universal functions of stability parameter d/L, with $d < \varepsilon\, h$, the *surface layer depth*:

$$\phi_m = \frac{\kappa d}{u^*}\frac{\partial}{\partial z}\sqrt{U^2+V^2} \tag{2.16}$$

$$\phi_s = \frac{\kappa d}{S^*}\frac{\partial S}{\partial z} \tag{2.17}$$

$$\text{with} \quad S^* = \frac{-\overline{ws}_0}{u^*}$$

The forms of the universal functions are not given by the theory, but must be determined theoretically or empirically.

Note that from here and in the following of this section, the m subscripts will stand for momentum components, the s for scalar properties and x for any of them.

2.2.2 Mixing inside the boundary layer

To determine the vertical turbulent fluxes through the oceanic boundary layer, the following formulation is used:

$$\boxed{\overline{wx}(d) = -K_x \left(\frac{\partial X}{\partial z} - \gamma_x \right)} \tag{2.18}$$

where K_x is the diffusivity and γ_x is the *nonlocal transport*. Uppercase X represents mean quantities and lowercase x is the corresponding turbulent fluctuation. We will now see how K_x and γ_x are evaluated.

Diffusivity

The diffusivity (in m^2/s) profile in the boundary layer is expressed as a product of a length scale, a velocity scale and a shape function, in agreement with the dimensional analysis:

$$\boxed{K_x(\sigma) = h\, w_x(\sigma) G(\sigma)} \tag{2.19}$$

where h is the boundary layer height, w_x is a depth dependent turbulent velocity scale, $G(\sigma)$ is a cubic shape function and $\sigma = d/h$ is a dimensionless vertical coordinate. The proportionality to h expresses the fact that a deeper boundary layer can contain larger and more efficient turbulent eddies.

The cubic shape function G can be written as:

$$G(\sigma) = a_0 + a_1\sigma + a_2\sigma^2 + a_3\sigma^3$$

where the a_i are coefficients evaluated through physical arguments:

- turbulent eddies do not cross the surface, therefore no transport takes place across $d = 0$: $K_x(\sigma = 0) = 0$,
- in the surface layer, the similarity theory applies,
- w_x has to scale with $w^* = (-B_f h)^{1/3}$ in the convective limit,
- diffusivity and its gradient have to match with the interior values at the base of the surface layer.

After some calculations, we finally obtain:

$$G(0) = 0 \tag{2.20a}$$
$$\frac{\partial G(0)}{\partial \sigma} = 1 \tag{2.20b}$$
$$G_x(1) = \frac{K_x(h)}{h\, w_x(1)} \tag{2.20c}$$
$$\frac{\partial G_x(1)}{\partial \sigma} = -\frac{1}{w_x(1)} \frac{\partial K_x(h)}{\partial z} - \frac{K_x(h)}{h\, w_x^2(1)} \frac{\partial w_x(1)}{\partial \sigma} \tag{2.20d}$$

The physical meaning of this set of equations is that the oceanic boundary layer is influenced by the ocean interior through a dependence of the shape function $G(\sigma)$ and its derivative $\frac{\partial G}{\partial \sigma}$ at $\sigma = 1$ on the interior diffusivity and its vertical derivative at $d = h$. That is a reason why the scheme is said to be nonlocal.

Turbulent velocity scales

In the surface layer ($\sigma < \varepsilon = \mathcal{O}(0.10)$), the similarity theory applies. Eliminating $\frac{\partial X}{\partial z}$ from (2.17) and (2.18) (with $\gamma_x = 0$), using (2.19) and approximating the polynomial by $G(\sigma) \cong a_1 + a_2\sigma$, we find

$$w_x(\sigma)(a_1 + a_2\sigma) = \frac{\kappa u^*}{\phi_x} \frac{\overline{wx}(d)}{\overline{wx}_0}, \tag{2.21}$$

which can be satisfied by equalling the velocity scale with the first factor of the right member. In the stably forced boundary layer, this relation is assumed to be valid everywhere, while under unstable conditions, the turbulence velocity scales beyond the surface layer are constant and equals their $\sigma = \varepsilon$ values, *i.e.*

$$w_x(\sigma) = \begin{cases} \dfrac{\kappa u^*}{\phi_x(\varepsilon h/L)}, & \varepsilon < \sigma < 1,\ \zeta < 0 \text{ (instable condition)} \\ \dfrac{\kappa u^*}{\phi_x(\sigma h/L)} & \text{otherwise.} \end{cases} \tag{2.22}$$

Working with

$$\phi_x = (a_x - c_x\zeta)^{-1/3}$$

and using relations (2.13), (2.21) and (2.22), we eventually get to

$$\boxed{w_x(\sigma) = \begin{cases} \kappa \sqrt[3]{a_x\, u^{*3} + c_x\, \kappa\sigma w^{*3}}, & \sigma < \varepsilon, \\ \kappa \sqrt[3]{a_x\, u^{*3} + c_x\, \kappa\epsilon w^{*3}}, & \sigma \geq \varepsilon. \end{cases}} \tag{2.23}$$

Nonlocal transport

This term is nonzero only for scalars in unstable (convective) forcing conditions. The formulas used are

$$\gamma_x = 0 \qquad \zeta \geq 0, \tag{2.24a}$$
$$\gamma_m = 0, \tag{2.24b}$$
$$\gamma_s = C_s \frac{\overline{ws}_0}{w_s(\sigma)h} \tag{2.24c}$$
$$\gamma_\theta = C_s \frac{(\overline{w\theta}_0 + \overline{w\theta}_R)}{w_s(\sigma)h} \qquad \zeta < 0. \tag{2.24d}$$

with $C_s = C^*\kappa(c_s\kappa\varepsilon)^{1/3}$, $C^* = 10$, $\overline{w\theta}_R$ represents the amount of radiative heat absorbed in the boundary layer that effectively contributes to the nonlocal transport of heat.

Boundary layer depth

The depth of the oceanic boundary layer, h, is expected to depend on:

- the surface forcing (wind, freshwater flux, heat flux, ...),
- the buoyancy profile,

- the velocity profile.

The value of h is obtained as the smallest value of d that makes the *bulk Richardson number*

$$\boxed{\mathrm{Ri}_b(d) = \frac{[B_r - B(d)]d}{|\mathbf{V}_r - \mathbf{V}(d)|^2 + V_t^2(d)}} \tag{2.25}$$

equal to its critical value Ri_{cr}. In (2.25), B_r and $\mathbf{V}_r$ are estimates of the average buoyancy and velocity, respectively, and V_t/h is the *turbulent velocity shear*. The latter is parameterized by

$$V_t^2(h) = \frac{C_v\sqrt{-\beta_T}}{\mathrm{Ri}_c\kappa^2}\sqrt{C_s\varepsilon}h\,N\,w_s$$

with
C_v, the ratio of the interior Brunt-Väisälä frequency to the Brunt-Väisälä frequency at the entrainment depth,
β_T, the ratio of entrainment buoyancy flux to surface buoyancy flux,
κ, the von Kármán constant,
C_s, a constant that parameterizes the boundary local transport,
ε, the nondimensional extent of the surface layer.

When the buoyancy forcing is stable, *i.e.* when the forcing buoyancy B_f is positive, the boundary layer depth is taken as the minimum of

- the value computed according to (2.25),
- the Monin-Obukov length (2.14),
- the Ekman depth $h_E = 0.7\,u^*/f$.

2.2.3 Mixing below the boundary layer

In the ocean interior, mixing is performed via three physical processes: instability due to vertical shear, internal wave breaking and double diffusion. The internal diffusivity ν_x is the sum of these three contributions:

$$\boxed{\nu_x(d) = \nu_x^s(d) + \nu_x^w(d) + \nu_x^d(d).}$$

Once ν_x is known, the turbulent vertical fluxes of scalar and momentum below the boundary layer are calculated by

$$wx(d) = -\nu_x(d)\frac{\partial X}{\partial z}$$

Shear instability

The tendency for shear instability is characterized by the *gradient Richardson number*, which is a measure of the relative importance of the stratification stabilizing effects over the shearing destabilizing effects:

$$\boxed{\mathrm{Ri}_g = \frac{N^2}{M^2}}$$

where

$$\begin{aligned} N^2 &= \frac{\partial b}{\partial z} \quad \text{is the Brunt-Väisälä frequency, and} \\ M^2 &= \left(\frac{\partial u}{\partial z}\right)^2 + \left(\frac{\partial v}{\partial z}\right)^2 \quad \text{is the shearing frequency.} \end{aligned}$$

Turbulent mixing will occur when Ri_g is under a critical value, *i.e.* the shearing effect is overcoming the stratification stabilizing effect. The diffusivity is then parameterized as a function of Ri_g:

$$\frac{\nu_x^s}{\nu^0} = \begin{cases} 1, & \mathrm{Ri}_g < 0, \\ \left[1 - \left(\frac{\mathrm{Ri}_g}{\mathrm{Ri}_0}\right)^2\right]^{p_1}, & 0 < \mathrm{Ri}_g < \mathrm{Ri}_0, \\ 0, & \mathrm{Ri}_0 < \mathrm{Ri}_g. \end{cases}$$

with $\nu^0 = 50 \times 10^{-4}$, $\mathrm{Ri}_0 = 0.7$ and $p_1 = 3$.

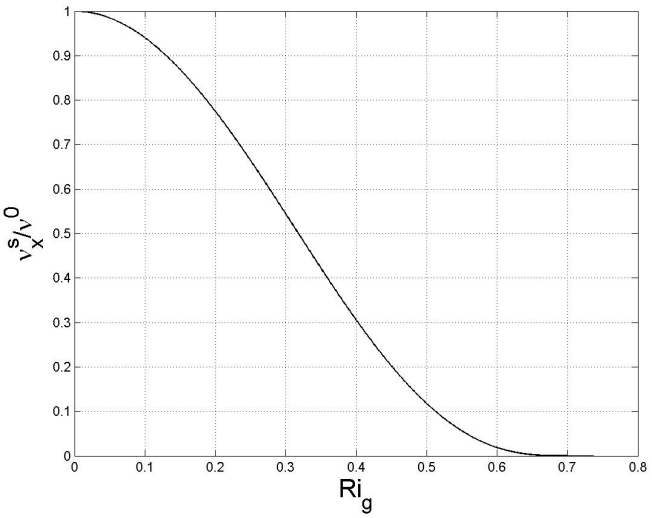

Figure 2.3: *Diffusivity parameterization for the shear instability.*

Double diffusion

The double diffusion is a phenomenon that occurs when the stratification is stable ($\frac{\partial \rho}{\partial z} < 0$) but either the temperature gradient or the salinity gradient is instable in its contribution to the density, *i.e.* $\frac{\partial T}{\partial z} < 0$ or $\frac{\partial S}{\partial z} >$, respectively. The first case is called *diffusive convection*,

the second *salt fingering*. To determinate where and when these phenomenons occur, the double-diffusion density ratio is defined:

$$\boxed{R_\rho = \frac{\alpha \frac{\partial T}{\partial z}}{\beta \frac{\partial S}{\partial z}},}$$

where α and β are the thermal expansion and the haline contraction coefficients, respectively.

- In the case of salt fingering, diffusivities are parameterized by

$$\frac{\nu_s^d(R_\rho)}{\nu_f} = \begin{cases} \left[1 - \left(\frac{R_\rho - 1}{R_\rho^0 - 1}\right)\right]^{p_2}, & 1.0 < R_\rho < R_\rho^0, \\ 0, & R_\rho \geq R_\rho^0. \end{cases}$$

$$\nu_\theta^d(R_\rho) = 0.7\,\nu_s^d,$$

with $\nu_f = 10^{-3}\,m^2 s^{-1}$, $R_\rho^0 = 1.9$ and $p_2 = 3$. The case where R_ρ is less or equal than 1 corresponds to a convective instability.

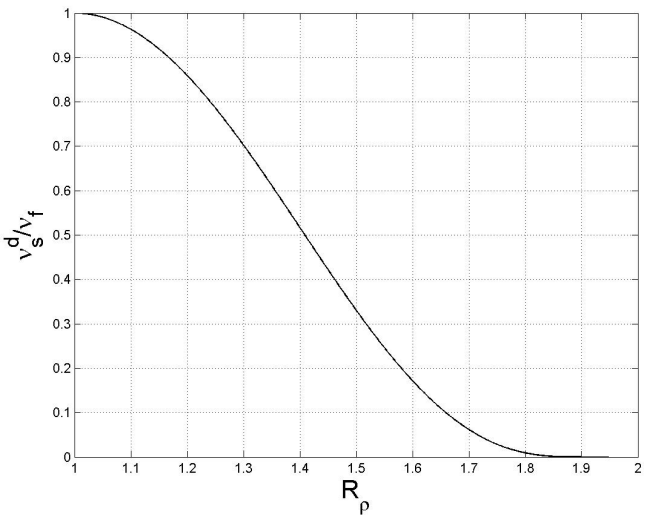

Figure 2.4: *Diffusivity parameterization for the salt fingering.*

- In the diffusive-convective case, the parameterization used is

$$\frac{\nu_\theta^d}{\nu} = 0.909 \exp\left(4.6 \exp\left[-0.54(R_\rho^{-1} - 1)\right]\right)$$

$$\nu_s^d = \begin{cases} \nu_\theta^d \left(1.85 - 0.85\,R_\rho^{-1}\right) R_\rho, & 0.5 \leq R_\rho < 1.0, \\ \nu_\theta\, 0.15\, R_\rho, & R_\rho < 0.5. \end{cases}$$

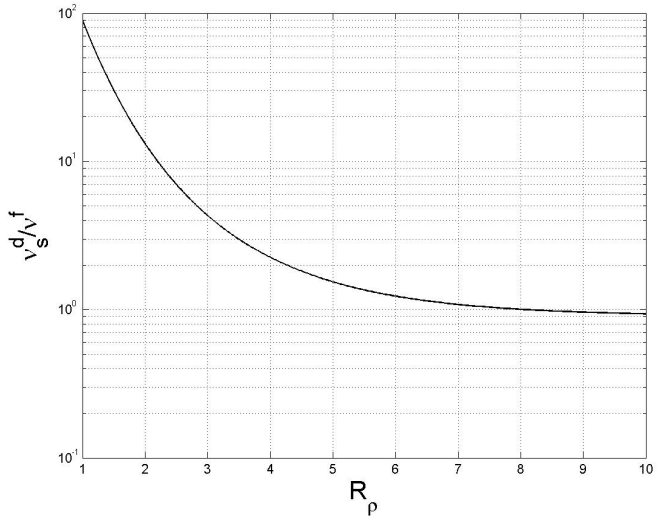

Figure 2.5: *Diffusivity parameterization for the diffusive convection.*

2.2.4 Summary

Here are the different steps of the mixing closure model, the formulas and the numerical values for the parameters implemented in the ROMS 1D code.

Procedure

1. Compute the bulk Richardson number at each point of the vertical grid (2.25).
2. Linearly interpolate to find the mixed layer depth, *i.e.* the value of the depth where Ri_b reaches its critical value.
3. Compute the buoyancy forcing (2.15); in the case of stable buoyancy forcing compare h with Ekman and Monin-Obukhov depths and restrict it if necessary .
4. Compute turbulent velocity scales w_m and w_s at $z = h$ ((2.23).
5. Compute coefficients for nondimensional shape functions $G_x(\sigma)$ in terms of interior diffusivities at $\sigma = 1$ and their vertical derivatives at $z = h$.
6. Set mixing coefficients within boundary layer:
   (a) Compute turbulent velocity scales, w_m and w_s at depths $z = z_w(k)$ (2.23),
   (b) Set the mixing coefficient profiles as products of these velocity scales and the nondimensional shape functions.
7. Compute the boundary layer nonlocal transport (2.24)

Formulas and parameters values

Bulk Richarson number:

$$\mathrm{Ri}_{bulk}(h_{bl}) = \frac{-g(\rho_{surf} - \rho(h_{bl}))h_{bl}}{\rho_0 \left[(u_{surf} - u(h_{bl}))^2 + (v_{surf} - v(h_{bl}))^2 + V_t^2(h_{bl})\right]}$$

Turbulent velocity scales:

Scalars:

$$w_s = \begin{cases} \kappa \sqrt[3]{-28.86\, u^{*3} + 98.86\, \kappa\sigma w^{*3}}, & \sigma < \epsilon, \\ \kappa \sqrt[3]{-28.86\, u^{*3} + 98.86\, \kappa\epsilon w^{*3}}, & \sigma \geq \epsilon. \end{cases}$$

Momentum:

$$w_m = \begin{cases} \kappa \sqrt[3]{1.86\, u^{*3} + 8.38\, \kappa\sigma w^{*3}}, & \sigma < \epsilon, \\ \kappa \sqrt[3]{1.26\, u^{*3} + 8.38\, \kappa\epsilon w^{*3}}, & \sigma \geq \epsilon. \end{cases}$$

Nonlocal transport

$$\gamma = 10\, \kappa \sqrt[3]{c_s \kappa \epsilon \frac{B_f}{h_{bl} w_s}}$$

Diffusivities:

$$K_M = 10^{-4} + 5 \times 10^{-3} \left[1 - \left(\frac{\mathrm{Ri}}{0.7}\right)^2\right]^3 + 0.1$$

$$K_T = 10^{-3} + 5 \times 10^{-3} \left[1 - \left(\frac{\mathrm{Ri}}{0.7}\right)^2\right]^3 + 0.1 + K_T^{dd}$$

$$K_S = 10^{-3} + 5 \times 10^{-3} \left[1 - \left(\frac{\mathrm{Ri}}{0.7}\right)^2\right]^3 + 0.1 + K_S^{dd}$$

Salt fingering case:

$$K_T^{dd} = 7 \times 10^{-4} \left[1 - \left(\frac{\min(R_\rho, 1.9) - 1}{0.9}\right)^2\right]^3$$

$$K_S^{dd} = 10^{-3} \left[1 - \left(\frac{\min(R_\rho, 1.9) - 1}{0.9}\right)^2\right]^3$$

Diffusive convection case:

$$K_T^{dd} = 1.3635 \times 10^{-6} \exp\left[4.6 \exp\left(-0.54(R_\rho^{-1} - 1)\right)\right]$$

$$K_S^{dd} = \begin{cases} 0.15\, K_T^{dd} R_\rho & , R_\rho < 0.5 \\ K_T^{dd}(1.85\, R_\rho - 0.85) & \text{otherwise.} \end{cases}$$

2.3 The biological model

In this section we describe the biological model which is coupled to the physical one. A complete understanding, description and explanation of this model could not be done in the present work, so we limit ourselves to outline the most important features of the model, which will allow us to interpret and discuss the numerical results.

Moreover, a biological model implies numerous parameters (see tab. A.1) for the different processes that occur between the biological species and for the interactions between the physical and the biological variables. These parameters have to take into account the specificities of the region of interest, therefore an important bibliographical study is required to find appropriate values. That is why we decide to work with the values provided in the original code, even if they are not perfectly representative on the biological conditions of the Canary Islands waters. Doing so, we hope to get a qualitative view of the evolution with time and depth of the biological variables.

2.3.1 Introduction

The biological model is based on [Fasham et al. (1990)]. Their model was designed to simulate annual cycles of plankton dynamics and nitrogen cycling in the ocean mixed layer. Nitrogen is generally considered as the limiting nutrient of primary production, hence its choice as central element of the biological model.

This model is compartmental: the ecosystem is divided into compartments, each compartment exchanging various fluxes (for example nitrogen, carbon, energy) with its neighbours. The task consists in modelling these flows, according to physical, biological and chemical processes that occur in the studied system. The fundamental assumption behind this kind of model is that the mixed layer can be considered biologically homogeneous. In other words, the physical mixing rate is fast compared to the growth rates of the organisms. This assumption is valid except for very deep mixed layer.

The choice of compartments and exchanges between them permits the distinction between *new* and *regenerated* productions: new production is the portion of total primary production that is driven by new nutrients (primarily nitrate) that originates from outside the euphotic zone. Regenerated production is defined as the part of primary production that is driven by nitrogen which is recycled within euphotic zone (mainly ammonium) [Dugdale and Goering (1967)].

2.3.2 Variables and exchange fluxes

This biological model deals with eight variables: nitrate (NO_3), ammonium (NH_4), phytoplankton ($Phyt$), zooplankton (Zoo), small detritus ($SDet$), large Detritus ($LDet$), chlorophyll a ($Chla$) and oxygen (Oxy). The different processes that lead to fluxes between the eight compartments are:

- the nitrate and ammonium *uptake* by phytoplankton;
- the *nitrification* of ammonium to nitrate;
- the phytoplankton *grazing* by zooplankton, giving zooplankton and detritus;

- the phytoplankton *mortality*, leading to small detritus;
- the zooplankton *excretion* of ammonium;
- the zooplankton *mortality*, yielding small detritus;
- the *coagulation* of phytoplankton with small detritus that provides large detritus;
- the small detritus *breakdown* to ammonium;
- the large detritus recycling to ammonium (*remineralization*).

The model also takes into account the vertical sinking, each biological variable being assigned with an adapted sinking velocity. It affects phytoplankton, small and large detritus. The effect of vertical sinking is calculated after the biogeochemical reactions. The algorithm for the vertical sinking is based on the piecewise parabolic method [Colella and Woodward (1984)].

2.3.3 Photosynthetically available radiation

Photosynthetically available radiation (PAR) indicates the total energy available to plants for photosynthesis and is thus a key parameter to study the ecosystem seasonality. In the model, the PAR is derived from the shortwave solar radiation according to the following steps:

1. A linearly interpolated value is calculated for each time step. This is necessary because the model works with a monthly forcing.
2. A diurnal cycle for the insulation is superimposed to the solar shortwave radiation.
3. If the calculated surface radiation is negative, zero is used instead.
4. Starting from the top, the PAR is calculated for each grid box according to

$$PAR_k = PAR_{k+1} \exp\left\{(-0.5\left(k_{water} + k_{Chla}[Chla]_k\right)\Delta z_k\right\}$$

with k_{water} and k_{Chla}, the attenuation coefficients for water and chlorophyll, $[Chla]$ the chlorophyll concentration and Δz, the height of the vertical grid layer. k is the cell index (from 1 at the bottom to N at the top).

As light abundance is an essential factor for primary production in pelagic systems, its evolution with respect with depth has to be parameterized suitably. Several PAR parameterizations are described in [Zielinski et al. (2002)], and their influences on the results of a coupled biological-physical model are compared.

They also show that the light model has significant effects on the simulated distribution of chlorophyll in space and time and recommend to use a model with an increased value of the attenuation coefficient near the surface, due to the absorption at larger wavelengths, and specific chlorophyll attenuation, as done in the present model.

2.3.4 Equations

We present here the equations of the biological model. Generally, the evolution of each variable (say B) is governed by an equation like:

$$\frac{\partial B}{\partial t} = \text{Source}_B - \text{Sink}_B.$$

For the sake of adding no unhelpful complexity, we will not write them in their mathematical form, but rather in terms of processes, as our purpose is simply to outline the relations between each variable. The equations resolved by the numerical model are formulated in appendix A.

Nitrate concentration

Nitrates are consumed by the phytoplankton and can be generated by the transformation of ammonium (nitrification). If Δ_t stands for "variation with respect to time", the evolution of the nitrate concentration may be written as:

$$\Delta_t(\text{nitrate}) = -\text{ phytoplankton uptake} + \text{nitrification}.$$

Ammonium concentration

The ammonium losses are induced either by the phytoplankton *uptake* or by the *nitrification*, while the concentration increase is due to *excretions* from zooplankton and detritus *remineralization*.

$$\begin{aligned}\Delta_t(\text{ammonium}) &= -\text{ phytoplankton uptake} - \text{nitrification} + \text{zooplankton excretion}\\ &- \text{small and large detritus remineralization}.\end{aligned}$$

Phytoplankton concentration

The phytoplankton concentration is increased by new and recycled production and decreased by *coagulation* with small detritus (giving large detritus) and zooplankton *grazing*. As said previously, phytoplankton, small and large detritus are each affected by vertical sinking.

$$\begin{aligned}\Delta_t(\text{phytoplankton}) &= \text{new production} + \text{recycled production} - \text{mortality}\\ &- \text{coagulation} - \text{grazing} + \text{vertical sinking}.\end{aligned}$$

Zooplankton concentration

The zooplankton increase is driven by phytoplankton consumption (*grazing*), then we can expect the zooplankton concentration to follow the phytoplankton concentration. Three mechanisms contribute to the zooplankton concentration decrease: its *metabolism*, which

creates ammonium, *mortality*, leading to small detritus, and *excretion*, which also provides ammonium. We can summary these processes by writing

$$\begin{aligned}\Delta_t(\text{Zooplankton}) &= \text{Grazing} - \text{zooplankton metabolism} - \text{zooplankton decease} \\ &- \text{excretion.}\end{aligned}$$

Small detritus concentration

The small detritus are created by residue of zooplankton grazing, as well as by phytoplankton and zooplankton deceases. The processes of *aggregation* (or coagulation) and *remineralization* induce a diminution of small detritus, leading to production of large detritus and ammonium, respectively. All in all, we may write

$$\begin{aligned}\Delta_t(\text{Small detritus}) &= \text{Zooplankton grazing residue} + \text{phytoplankton decease} \\ &+ \text{zooplankton decease} - \text{aggregation} - \text{remineralization} \\ &+ \text{vertical sinking.}\end{aligned}$$

Large detritus concentration

The processes responsible for large detritus generation were mentioned with the previous variable: these processes are *coagulation* of phytoplankton with small detritus and *remineralization*. Taking into account the vertical sinking, the temporal evolution of large detritus is given by

$$\Delta_t\,(\text{Large detritus}) = \text{aggregation} - \text{remineralization} + \text{vertical sinking.}$$

Chlorophyll concentration

The chlorophyll equation deals with θ, the cellular chlorophyll to carbon ratio. The important fact is that chlorophyll concentration is increased of new and regenerated productions and also affected by the vertical sinking.

Oxygen concentration

The oxygen evolution is driven by the new and regenerated production (increase), the nitrification (decrease), the metabolism and respiration of zooplankton and the remineralization of detritus into ammonium. The oxygen equation reads

$$\begin{aligned}\Delta_t(\text{oxygen}) &= \text{new production} + \text{recycled production} - \text{nitrification} \\ &+ \text{zooplankton excretion and respiration} - \text{detritus remineralization} \\ &+ \text{gas exchange.}\end{aligned}$$

2.3.5 Summary of the exchange processes

On fig. 2.6 is showed the nitrogen fluxes between each compartment, which permits to give rise to the coupling between each variable.

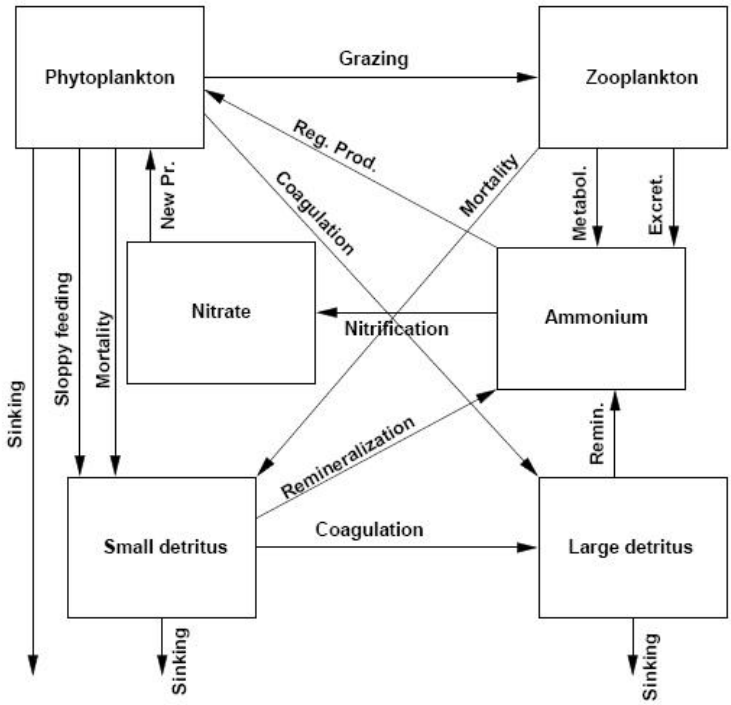

Figure 2.6: *Schematic representation of the fluxes of nitrogen in the model.*

2.3.6 Parameters value

The model allows us to choose between two sets of parameters value: one for the oceanic (oligotrophic [4] waters) and one for the coastal case (eutrophic [5] waters). As we have mentioned in the beginning of this section, the tuning of the biological parameters requires important bibliographical researches, and this could not be undertaken in the present work. Moreover, each biological model is different, thus the parameters used are also different.

For those reasons we decided to work with the values of the oceanic case displayed in tab. A.1.

2.4 Adjustable parameters

This section is dedicated to the description of the model parameters that can be changed and adapted to a specifical simulation.

2.4.1 Running parameters

- `time`: time of the year (in seconds) when the simulation starts. This time has to be adapted in agreement with the initial profiles chosen as initial conditions.
- `tdays`: time of the year (in days) when the simulation starts.

[4] Lacking in plant nutrients and having a large amount of dissolved oxygen throughout
[5] Rich in mineral and organic nutrients that promote a proliferation of plant life

- `dt`: time step in seconds.
- `ntimes` total number of time steps in current run, *i.e.* time of the numerical simulation.
- `noutput`: number of time steps between writing in output file .
- `twrite`: number of days before starting to write in output file.

2.4.2 Physical parameters

- `hmax`, the maximum depth in meters.
- `thetas`, the grid stretching parameter: increasing θ_s increases the vertical resolution near the surface (see section 2.1.3).
- `N`, number of vertical layers.
- `Jwtp`, the Jerlov water type ([Jerlov (1968)]), used to compute the fraction of solar shortwave flux penetrating the water at a specified depth.
- $\texttt{Ri}_{\texttt{cr}}$, the critical Richardson number.
- λ, the latitude and f, the Coriolis parameter.

2.4.3 Biological parameters

- the initial values of biological variables (NO_3, NH_4, O_2 etc).
- parameters from the biological model [Fasham et al. (1990)] (see tab. A.1).

Summary

The ROMS 1D model can be broken up into three components: physical, biological and mixing.

The physical model deals with the velocities (u, v), the temperature T and the salinity S. It is forced by the sea surface temperature, the surface net heat flux, the short wave solar radiation, the freshwater flux and the wind stress.

The biological model concentrates on the nitrogen cycle, with the following variables: nitrate NO_3, ammonium NH_4, phytoplankton, zooplankton, small and large detritus, chlorophyll a and oxygen.

The mixing closure scheme is the K-profile parameterization. Two regimes are distinguished: near the surface and the ocean interior, where vertical shear, internal wave breaking and double diffusion are the processes taken into account.

Chapter 3

Initialization and model forcing

3.1 Choice of the simulation parameters

The parameters we worked with were chosen according to our main purpose: the simulation of annual cycles of phytoplankton, zooplankton and nutrients. We also had to into account numerical constrains. Complete description of these parameters are found in section 2.4.

Numerous runs were made in order to assign suitable values to these parameters. We summarize here the conclusions of these preliminary tests.

`time = 235 days:` the initial conditions were taken between the 17th and 25th of August.

`dt = 60 seconds:` longer time steps caused numerical instability.

`ntimes = 6 years:` we simulate the phenomenon during six years, the time necessary to obtain a stabilisation of the differents variables, and keep only the last year values.

`noutput = 1 day` : since we are not interested in the diurnal cycle, the numerical results were kept only one time per day (or 24 time steps).

`latitude = 27.5° North, longitude = 15.5° West:` see fig. 3.1.

`hmax = 500 meters`

`thetas = 4:` this value yields a good refinement of the vertical grid near the air-sea interface.

`N = 40 layers:` compromise between precision and computation time. Larger number of layers were tried but did not yield significant differences in the results.

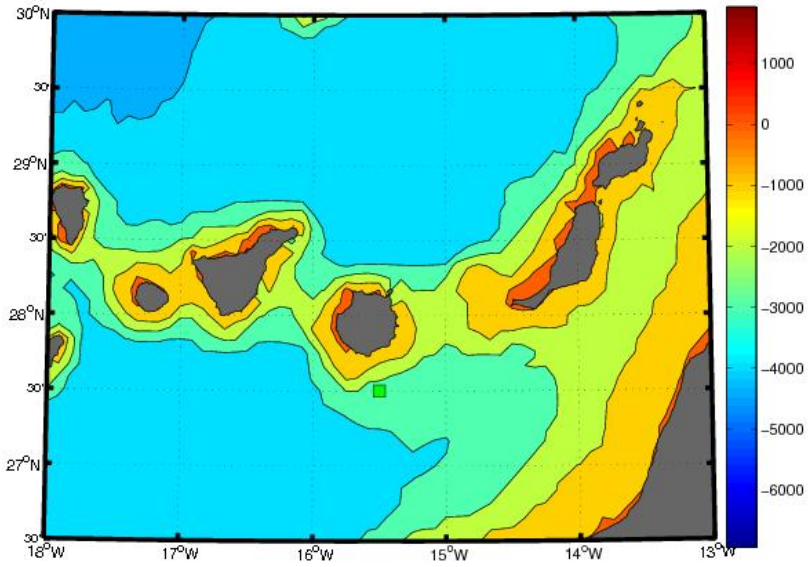

Figure 3.1: *Bathymetry of the region of interest for the simulations.*

The Jerlov water types

Jerlov (1951) classified oceanic water types according to their optical attenuation properties [Jerlov (1968)]. `Type I` waters were represented by extremely clear oceanic waters. Most clear coastal waters were classified as `Type II` because attenuation tends to be greater than that for oceanic waters of low productivity [1]

In the source code, the fraction of surface shortwave radiation forcing penetrating to a depth z is computed by

$$\texttt{swdk}(z) = r_1(i) \exp\left(\frac{z}{\mu_1(i)}\right) + [1 - r_1(i)] \exp\left(\frac{z}{\mu_2(i)}\right), \tag{3.1}$$

with the coefficients values given in tab. 3.1. Because we do not possess sufficient data to determinate which type of water we have, we work assuming water of `Type II`. Plots of light intensity with depth are shown on fig. 3.2 for the five Jerlov water types. Absorbtion is more efficient in the first meters with `Type I` water, but in the rest of the water column light penetrates deeper.

The choice of this parameter will only affect the qualitative aspect of the cycles we study in this work, as more or less light will reach a determined depth, according to the water type chosen. This will be illustrated on the fig. 5.6 (section 5.1.4), where the MLD is computed for the five values of type of water.

[1] Source: Unesco Environment and development in coastal regions and in small islands.

Jerlov water type	r_1	μ_1	μ_2
I	0.58	0.35	23
II	0.62	0.60	20
III	0.67	1.00	17
IV	0.77	1.50	14
V	0.78	1.40	7.9

Table 3.1: *Values of the parameters for the surface shortwave radiation attenuation in function of the Jerlov water type.*

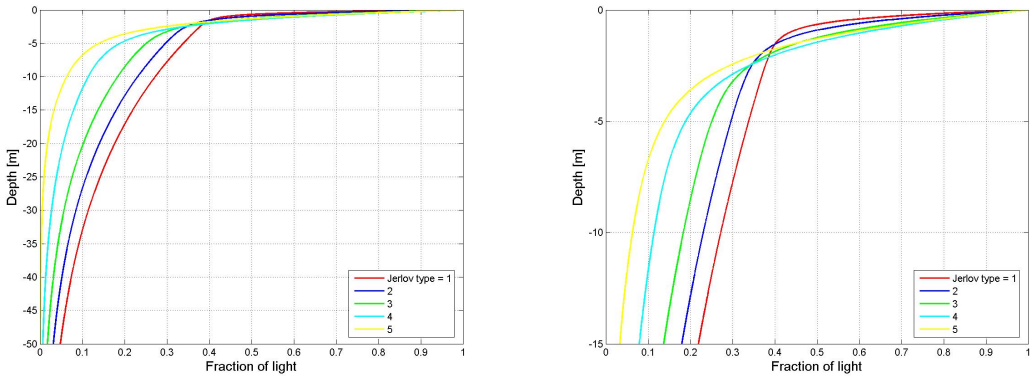

(a) 50 m (b) 15 m

Figure 3.2: *Fraction of surface light as a funcion of depth for the five Jerlov water types.*

3.2 Initialization

In order to get more realistic results, we have replaced the initial conditions from the original model (see section 2.1.2 page 13) by real data from cruises made in proximity of the point where our simulations are done. These data are taken from the FAX campaign [Barton et al. (2004)]. Moreover, preliminary tests realized on the model showed high sensibility to initial conditions, therefore it is essential to work with realistic initial data to get correct results.

As we do not have any profile at the exact location of the study, we worked with mean profiles, calculated from vertical profiles measured between the 17th and the 25th of August. A 4th-degree interpolation was performed to get a analytical relation between the depth and the other variables. This interpolation was chosen because it allowed to preserve the shape the profiles; higher degree interpolation were also tried but yield vertical fields with large oscillations, which do not correspond to the physical reality.

The figure 3.3 shows the positions of the points where the vertical profiles were taken and the point where simulations were carried out. When no vertical profile was available for a variable, we used a constant value over the water column (tab. 3.2).

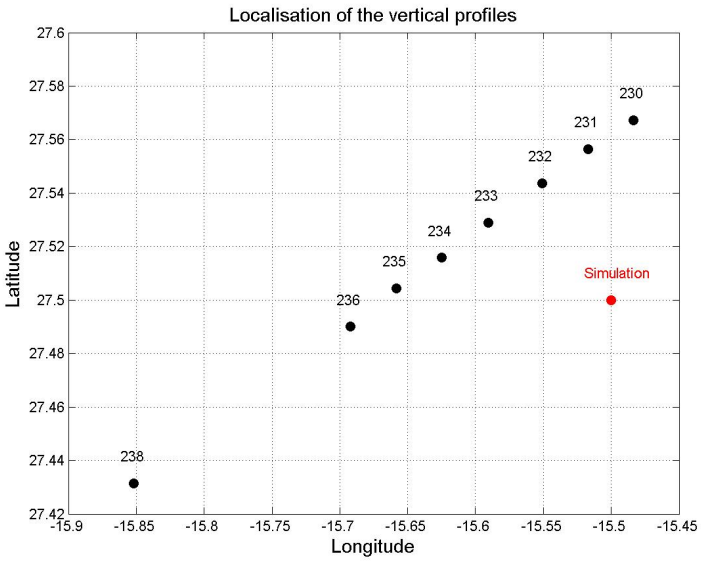

Figure 3.3: *Localisation of the vertical profiles used to compute the initial conditions. Numbers indicate days of the year. Data are from the FAX campaign.*

Temperature

The profile shows a very small mixed layer, with a temperature around $23\,°C$, and the seasonal thermocline, which becomes weaker at $150, m$, with a temperature below $12\,°C$ at the bottom.

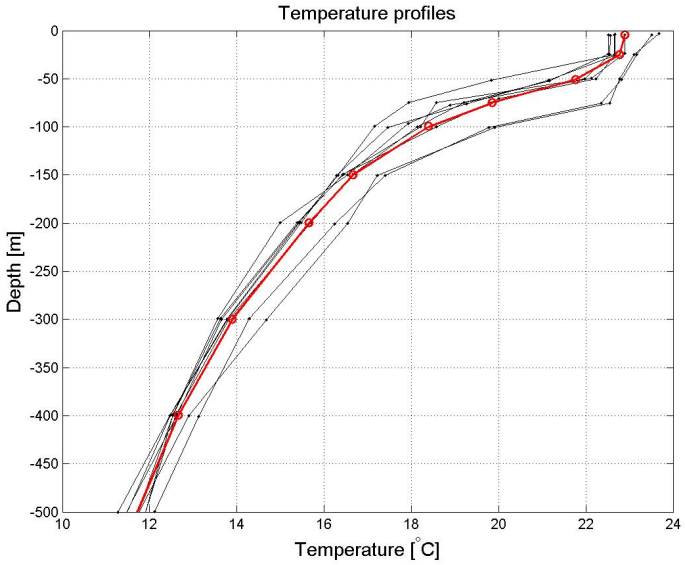

Figure 3.4: *Vertical profiles of temperature: in black are the profiles at the positions and times specified on the figure; in red is the mean profile.*

Salinity

We can see a constant value from 0 to $-50\,m$, a slight increase (around $0.1\,PSU$) from -50 to $-100\,m$, followed by a decrease of nearly $1\,PSU$ over the last $400\,m$.

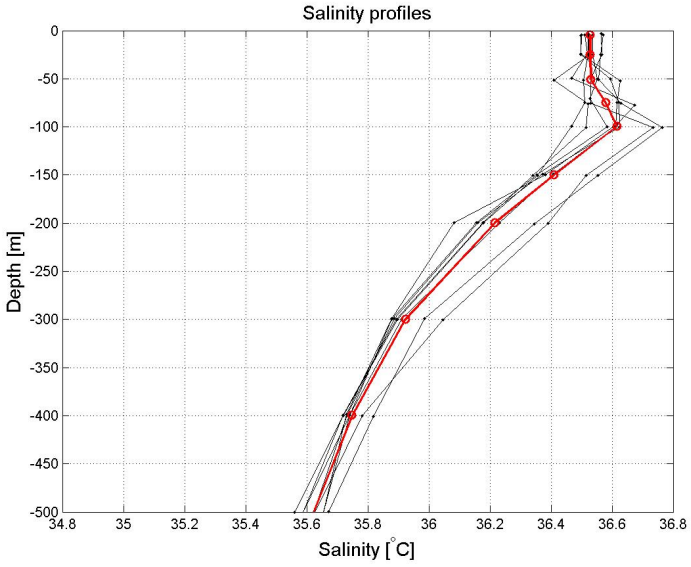

Figure 3.5: *Vertical profiles of salinity.*

Oxygen

The surface value is around $220\,m\,mol/m3$, then the concentration increases until a value of $220\,m\,mol/m3$ at $-75\,m$, to finally reach its lowest value at the bottom,

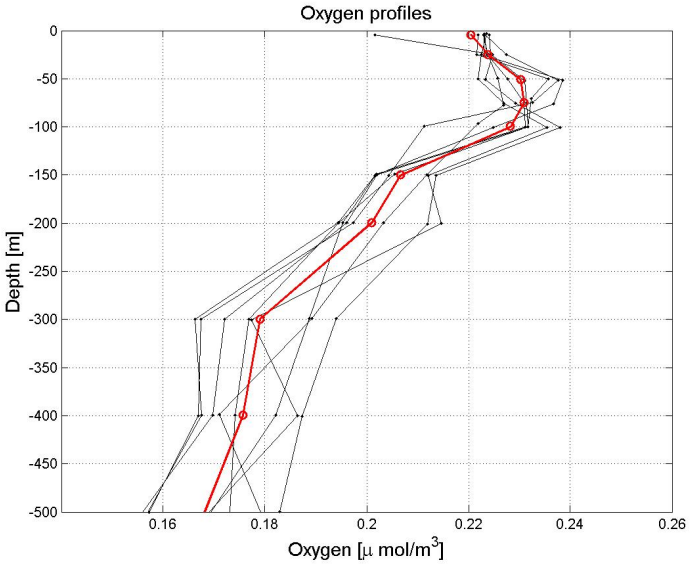

Figure 3.6: *Vertical profiles of oxygen concentration.*

Nitrate

The nitrate profile nearly null values from the surface to $-50\,m$. The the decrease is weak from $-50\,m$ to $-100\,m$ and then sharper to the bottom.

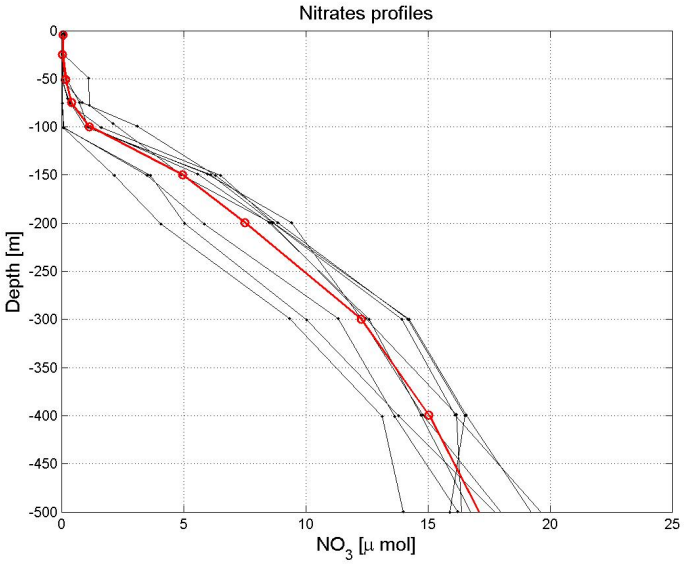

Figure 3.7: *Vertical profiles of nitrate.*

Other variables

For our simulations, we do not dispose of initial profiles for each variables, we attribute a constant value over the water column depth to the other variables. The difficulty is to choose these values according to the specificity of the studied region. We performed several runs to see the influence provoked by changes in these parameters. As the numerical runs are performed over 4-year period, we did not see significative change in the results. The values used are reported in the below table.

Variable	Units	Prescribed value
Ammonium	$mMol\,N_2m^{-3}$	0.1
Chlorophyll a	$mg\,Chl_a\,m^{-3}$	0.5
Phytoplankton	$mMol\,N_2m^{-3}$	$0.5/(6.625 * 12 * 0.053)$ $(\star)$
Zooplankton	$mMol\,N_2m^{-3}$	0.06
Small detritus	$mMol\,N_2m^{-3}$	0.04
Large detritus	$mMol\,N_2m^{-3}$	0.02

Table 3.2: *Initial values for the biological parameters. $(\star)$: using the maximal chlorophyll/phytoplankton ratio.*

3.3 Forcing

The forcing is an important step in the modelling process: it expresses the influence of the external world on the system, *i.e.* in our case, the effects of the atmosphere on the ocean. In other words, forcing quantifies how heat, fresh water and momentum are exchanged across the air-sea interface.

That is why an important part of this work was dedicated to the research and the processing of data. Moreover, a good description of this forcing will be useful when we will have to give an interpretation of the numerical results.

We worked with 10-year averaged data (from 1993 to 2002) to get a yearly mean annual cycle. The simulation are done in the south of Gran Canaria Island, at 27°30′ north and 15°30′ west (fig. 3.1). When necessary, the data are interpolated (inverse distance interpolation) to get the value at the same localisation. The table 3.3 summarises the nature of data and their sources.

There are often many sources for a determined type of data, so we need criterions for our choices: we try to work with dataset with the optimal spatial resolution and with reanalized datas. As an example, we compare the sea surface temperature from two different sources (fig. 3.15): the plots of individual years are different from one case to another, but the 10-year means are very close.

Data	source
Sea surface temperature	NOAA optimum interpolation SST V2
Solar short wave radiation	OAFlux
Surface freshwater flux	ECMWF
Surface momentum stress	CDC Derived NCEP Reanalysis Products Surface Flux
Surface net heat flux	OAFlux

Table 3.3: *Types of data and their sources*

3.3.1 Wind stress

Wind stress is defined as the drag force per unit area caused by wind shear [2]. It is computed with the help of the formula

$$\boldsymbol{\tau} = \rho_{air} C_D \left\| \mathbf{U_{10}} \right\| \mathbf{U_{10}} \tag{3.2}$$

where ρ_{air} is the air density, $\mathbf{U_{10}}$ is the wind speed at 10 meters, and C_D is the *drag coefficient*, which depends on the stability of the air column. In this work, we directly use the wind stresses computed and reanalysed in the CDC Derived NCEP Reanalysis Products Surface Flux data set.

An important feature of the wind stress is that the maximum wind intensity taking place in summer, leading to a situation with strong shearing. The fig. 3.9 also shows the high variability from one year to another.

The wind stress vectors are plotted on fig. 3.10 and point out the nearly constant direction through the year and the maximum intensity in July.

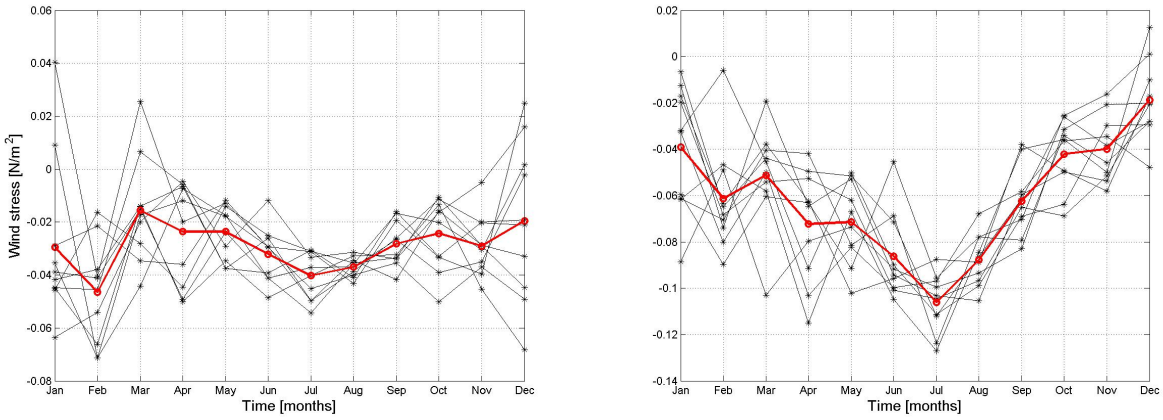

(a) Eastward

(b) Northward

Figure 3.8: *Wind stress Eastward and Northward components; the 10-year mean is plotted in red.*

[2]Source: AMS Glossary of Meteorology.

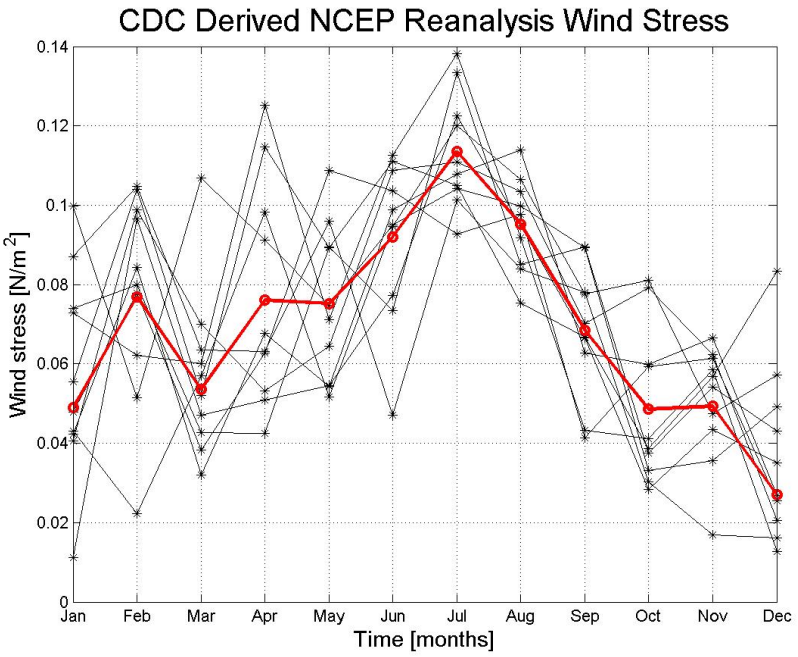

Figure 3.9: *Monthly wind stress.*

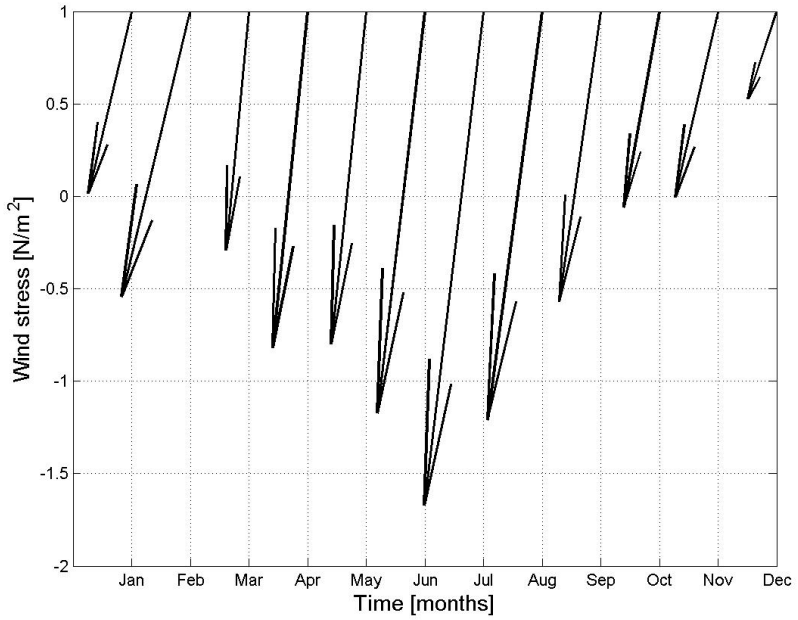

Figure 3.10: *Monthly-averaged wind stress vectors.*

3.3.2 Surface net heat flux

The surface net heat flux is the total amount of heat which is effectively transferred to the surface. It can be positive (the ocean acquire heat from the atmosphere) or negative (net heat loss) and has the dimension of a power per unit area of surface ($Watt/m^2$). It is the sum of four different fluxes:

The shortwave solar radiation: this radiation comes from the Sun and penetrates through space to the outer surface of Earth atmosphere. The energy received by a surface oriented perpendicular to an incoming beam of light has a value around $1377\,W/m^2$. When penetrating through the atmosphere, this radiation undergoes absorption and reflection, which decreases its intensity [3].

The shortwave radiation is positive all through the year, with maximum in May-June (fig.3.11(a)), period when the sun angle approaches its maximal value .

The longwave solar radiation: the energy absorbed at the surface is radiated by the Earth as *terrestrial longwave radiation* ($L\uparrow$) which is dependent on the temperature of the surface. This longwave radiation is partly absorbed by the gases of the atmosphere and then emitted downward as *longwave atmospheric counter-radiation* ($L\downarrow$). Its consequence is to keep the surface temperature warmer than in absence of the atmospheric gases. This is called the *greenhouse effect*.

The net longwave radiation is the difference between the downward and upward longwave radiations:

$$L^* = L\downarrow - L\uparrow .$$

The longwave radiation is always negative (heat loss for the ocean) and has a minimal intensity in summer (fig. 3.11(b)). This can be explained by the higher upward radiation generated by the summer temperatures.

The sensible heat flux: it is the heat energy transferred between the surface and air when there is a difference in temperature between them.

We observe a negative sensible heat flux during the year (fig. 3.11(c)), except in July and August, which means that the sea temperature is generally higher than the atmosphere temperature (downward temperature gradient).

An example of computation of this flux is found in [Haney (1971)]:

$$Q_H(T_S) = \rho_{air} C_D W\, C_p(T_S - T_A), \tag{3.3}$$

with C_D is the drag coefficient, W the wind speed , C_p the specific heat of air at constant pressure, T_S the temperature of ocean surface and T_A the temperature of air. The important features in equ. 3.3 are the proportionality of the flux to the temperature difference and to the wind speed.

The latent heat flux: it is the quantity of heat absorbed or released by a substance undergoing a change of state: evaporation, condensation, melting, freezing or sublimation. This heat flux is said to be latent because the during the transformation from a state to another, the temperature remains constant.

For example, the evaporation requires a heat supply to occur. That is why we feel cold when we go out of the seawater: the water takes some heat from our skin to change its state to vapour. Conversely, the water condensation is a transformation which gives

[3] Source: `http://www.uwsp.edu/geo/faculty/ritter/geog101/textbook/energy/energy_balance.html`.

energy to the external environment. This is what provides energy to tropical cyclones, which occur in warm and wet regions.

The formula given in [Haney (1971)] again show the influence of the wind speed on the flux:

$$Q_E(T_S) = \rho_{air} C_D W \, L(q_S\,[T_S) - q_A]\,, \tag{3.4}$$

where L is the latent heat of vaporization, $q_S(T_S)$ is the saturation specific humidity at the ocean temperature T_S and q_A is the specific humidity of air.

The fig. 3.11(d) shows a correlation between the wind stress and the latent heat flux: the evaporation rate is enhanced by the wind, therefore the latent flux is maximum in the period of intense winds.

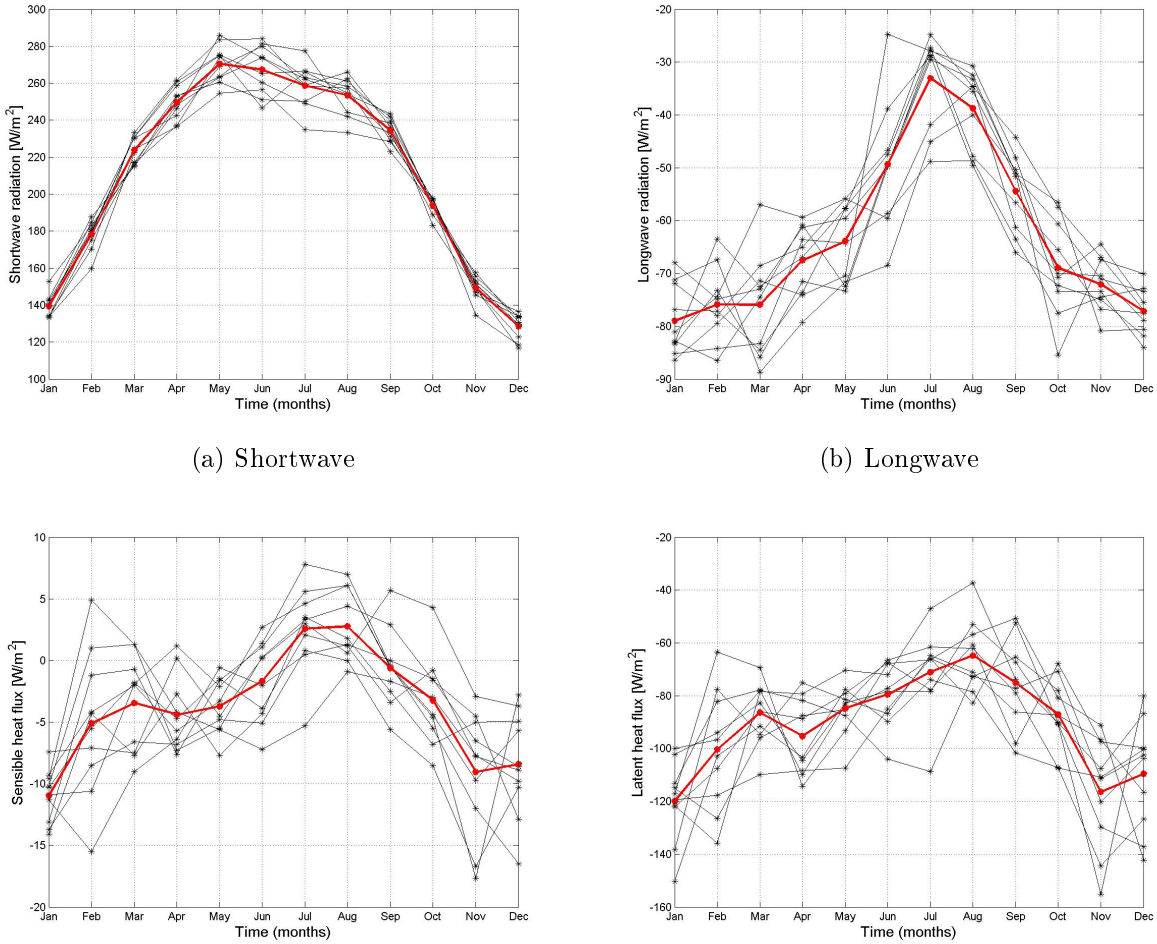

(a) Shortwave

(b) Longwave

(c) Sensible

(d) Latent

Figure 3.11: *The four terms of the surface net heat flux.*

Summing the four contributions, we finally get the monthly heat fluxes depicted on fig. 3.13. Here are the conclusions we can draw:

1. The latent, sensible and longwave fluxes constitute loss of heat for the ocean.

2. The total heat flux is negative from mid-October to February. Therefore this period will be favorable to convective mixing.

3. The maximum value ($\mathcal{O}(150\,W/m^2)$ on average) is reached in July-August, but can vary between 100 and $200\,W/m^2$ according to the atmospherical conditions.

We worked with Objectively Analysed Air-Sea Fluxes because this data set provides values coming from an weighted objective analysis of data from NCEP reanalysis and ECMWF operational analysis. They are the best estimates of heat fluxes.

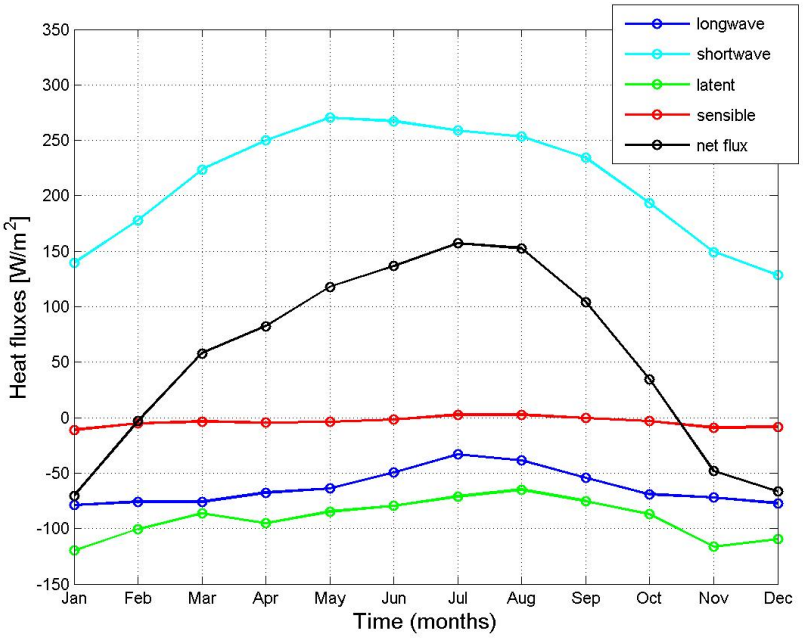

Figure 3.12: *Contributions to surface net heat flux.*

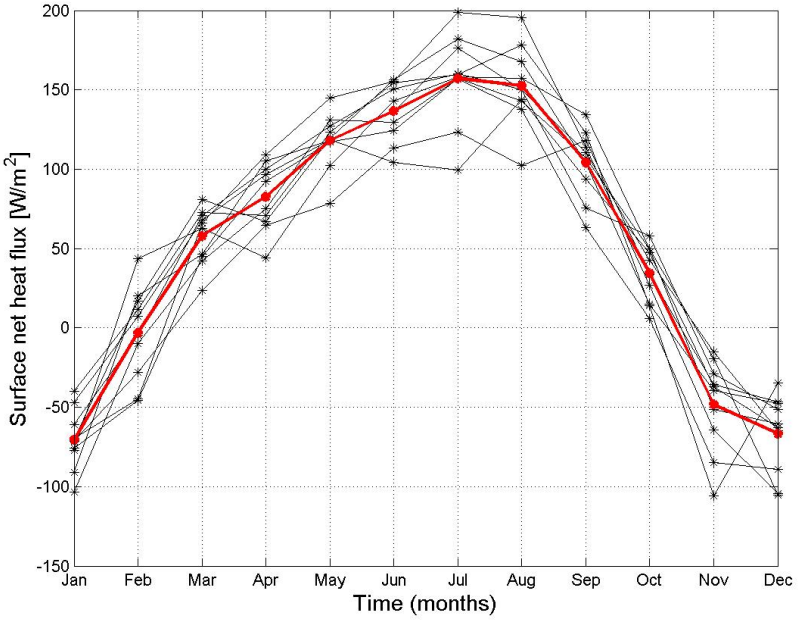

Figure 3.13: *Monthly surface net heat flux.*

3.3.3 Surface freshwater flux

The surface freshwater flux is defined as the difference between precipitation and evaporation. Its effect is to modify the surface density via the salinity: if evaporation is greater than precipitation (negative surface heat flux), the surface salinity will be increased.

As we see on the fig. 3.14, the freshwater flux is maximum from November to January (around $0.1\,cm/day$) and minimum in summer, where the evaporation rate is maximum. Globally, the observed values are weak and thus will not have a great influence on the salinity.

The source for these data is the ECMWF 40 Years Re-Analysis, because it is the only one which provides both reanalysed precipitation and evaporation values.

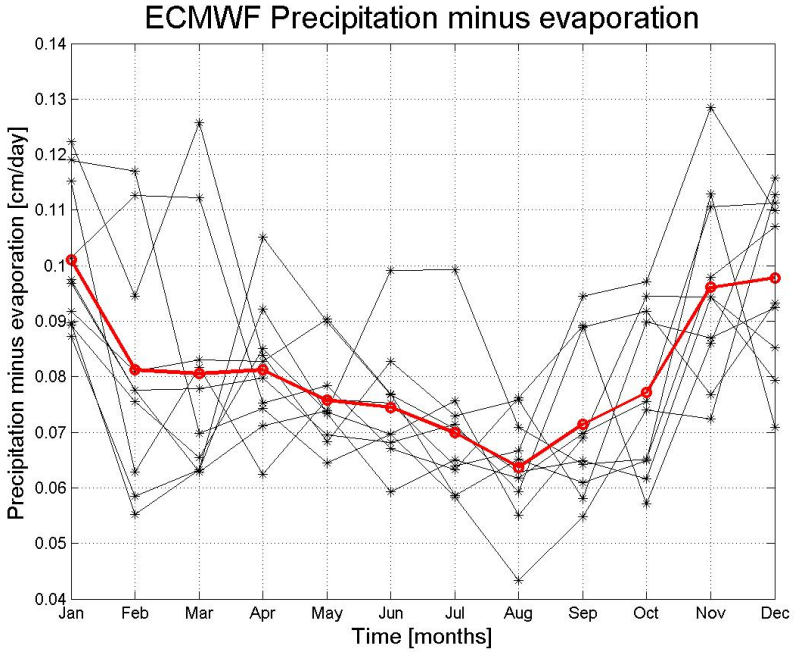

Figure 3.14: *Monthly surface freshwater flux.*

3.3.4 Sea surface temperature

The *sea surface temperature* (SST) is the temperature of the ocean surface. The term sea surface temperature is generally meant to be representative of the upper few meters of the ocean as opposed to the *skin temperature*, which is the temperature of the upper few centimeters.

It is important to point out that the SST is not used as a boundary condition for the temperature: the real boundary condition for T expresses the continuity of the heat flux across the air-sea interface [equ.(2.10)]. We will see in section 3.3.6 that SST is required to bring correction to the heat fluxes through the *surface net heat flux sensitivity to SST*.

The fig. 3.15 shows the seasonal variability of the SST, with values ranging from $19°C$ in February-March to 23° in September-October, *i.e.* about one or two months after the maximum net heat flux.

We worked with SST from NOAA Optimum Interpolation, but other databases can provide values close to these ones.

3.3.5 Solar shortwave radiation

The shortwave radiation was defined in section 3.3.2. The maximum occurs in May-June around $270\,W/m^2$ and stays at a value close to $260\,W/m^2$ until August.

3.3.6 Surface net heat flux sensitivity to SST

The surface net heat flux sensitivity to SST is used in the calculation of the *model* surface net heat flux, from the sea surface temperature and the *measured* surface net heat flux.

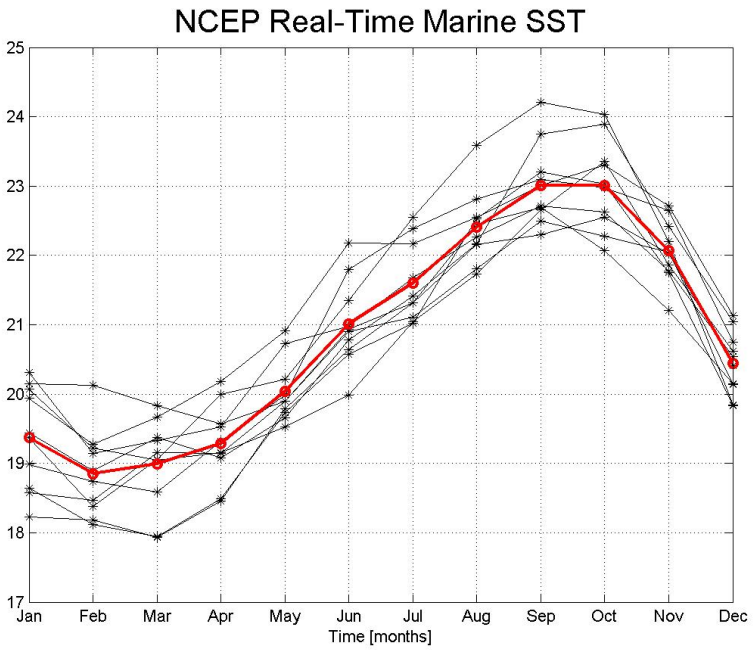

(a) NCEP

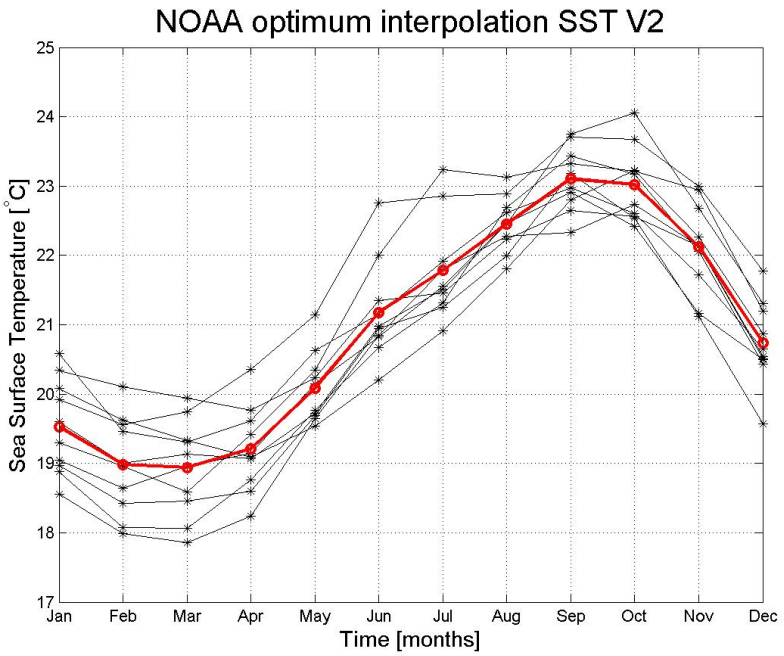

(b) NOAA

Figure 3.15: *Monthly sea surface temperature.*

This means that an approximate surface boundary condition is used, rather than a more physically realistic condition that involves (often inaccurate) surface fluxes.

Justifications of the physics behind the following formulas can be found in [Haney (1971)] and [Killworth et al. (2000)]. The aim of this section is to expose the main results and the data required to compute these forcing parameters.

Formulation

Let us call Q_{model}, the model sea surface net heat flux and Q, the sea surface net heat flux from the atmospheric data. Theses two fluxes are linked with the difference between the model temperature and the sea surface temperature, following the formula:

$$\begin{aligned} Q_{model} &= Q + \frac{d\,Q}{d\,SST}\,(T_{model} - SST)\,, \quad \text{with} \\ \frac{d\,Q}{d\,SST} &= q_1 + q_2 + q_3, \end{aligned} \tag{3.5}$$

q_1, q_2 and q_3 representing the three different contributions to $\frac{d\,Q}{d\,SST}$:

- q_1, the infrared contribution:

  $$q_1 = -4\,\varepsilon\,\sigma\,(SST^3),$$

  where SST is the sea surface temperature, ε is the emissivity coefficient and σ is the Stefan-Boltzmann constant.

- q_2, the sensible heat contribution:

  $$q_2 = -\rho_{atm}\,C_p\,C_h\,U,$$

  where ρ_{atm} is the atmosphere volumic mass, C_p is the specific heat of atmosphere, C_h is the sensible heat transfer coefficient (stable condition) and U the wind speed.

- q_3, the latent heat contribution:

  $$q_3 = -\rho_{atm}\,C_e\,L\,U\,\frac{d\,q_{sea}}{d\,T},$$

  where C_e is the latent heat transfer coefficient (stable condition), L is the latent heat of vaporisation , q_{sea} is sea level specific humidity. L and $\frac{d\,q_{sea}}{d\,T}$ are calculated according to

  $$\begin{aligned} L &= 2.5008\,10^6 - 2.3\,10^3\,sat \\ \frac{d\,q_{sea}}{d\,T} &= 2353\,\ln(10)\,\frac{q_{sea}}{SST^2} \end{aligned}$$

  with sat, the sea surface atmospheric temperature.

The value of the parameters is given in the table 3.4 and the necessary atmospheric data are summarized in the table 3.5.

Putting it altogether, we finally obtain

$$\begin{aligned} \frac{d\,Q}{d\,SST} &= q_1 + q_2 + q_3 \\ &= -4\varepsilon\,\sigma\,T^3 - \rho_{atm} C_p\,C_h\,U - \rho_{atm} * C_e\,L\,U\,2353\,\ln\left(10\,\frac{q_s}{T^2}\right) \end{aligned} \tag{3.6}$$

Parameter	Value	Unit
specific heat of atmosphere	1004.8	$J\,kg^{-1}\,K^{-1}$
sensible heat transfer coefficient	$0.66\,10^{-3}$	–
latent heat transfer coefficient	$1.15\,10^{-3}$	–
emissivity coefficient	0.98	–
Stefan-Boltzmann constant	$5.6697\,10^{-8}$	$Wm^{-2}K^{-4}$

Table 3.4: *Values of the parameters for the calculation of $dQ/dSST$.*

Symbol	Variable	Unit
SST	sea surface temperature	K
sat	sea surface atmospheric temperature	$°C$
ρ_{atm}	atmospheric density	kg/m^3
U	wind speed	m/s
q_{sea}	sea level specific humidity	$(kg\,water/kg\,air)$

Table 3.5: *Data used for the $dQ/dSST$ computation.*

Data used

We use the same approach as in the previous section and work with 10-year averaged data. All the variable except the air density, are taken from the NCEP database.

Specific humidity: it is a measure of the quantity of water contained in a given volume of air. Its value depends on the atmospherical conditions: the higher is the temperature, the more water can be contained in the air volume.

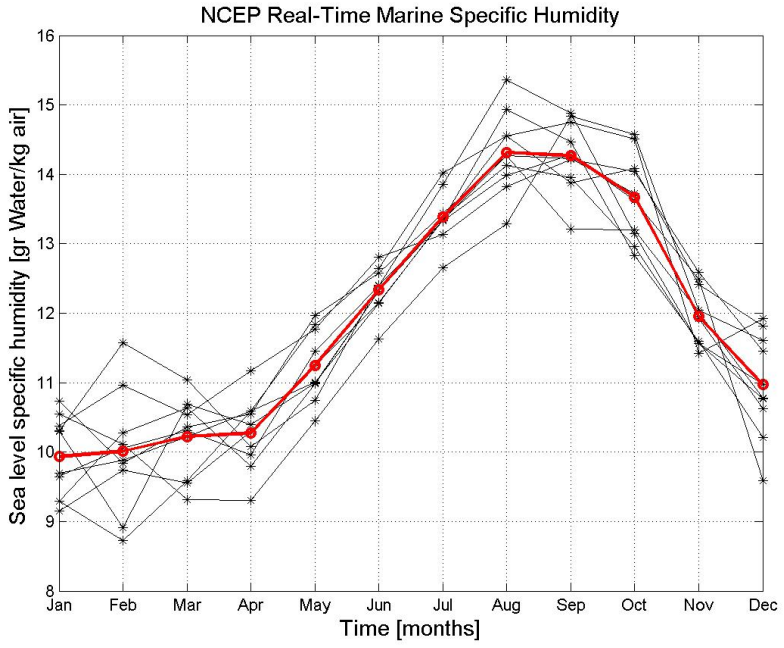

Figure 3.16: *NCEP specific humidity.*

Wind speed: as expected, the 10-meter wind speed has the same characteristics than the wind stress: maximal intensity from June to August, minimal values in winter.

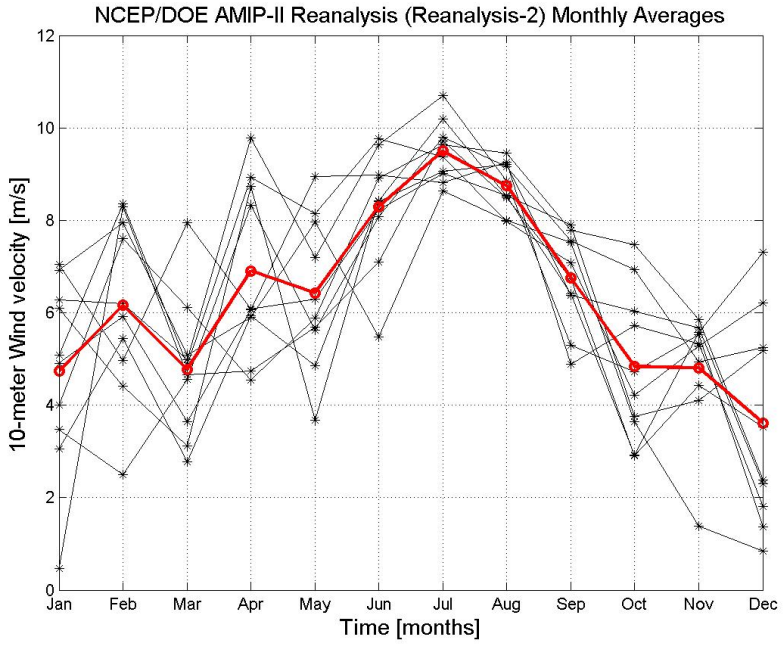

Figure 3.17: *NCEP 10-meter wind speed.*

Sea atmospheric temperature: same seasonal evolution than the SST, but the amplitude of variations are smaller: between $18°C$, from January to April, and $22°C$ in October.

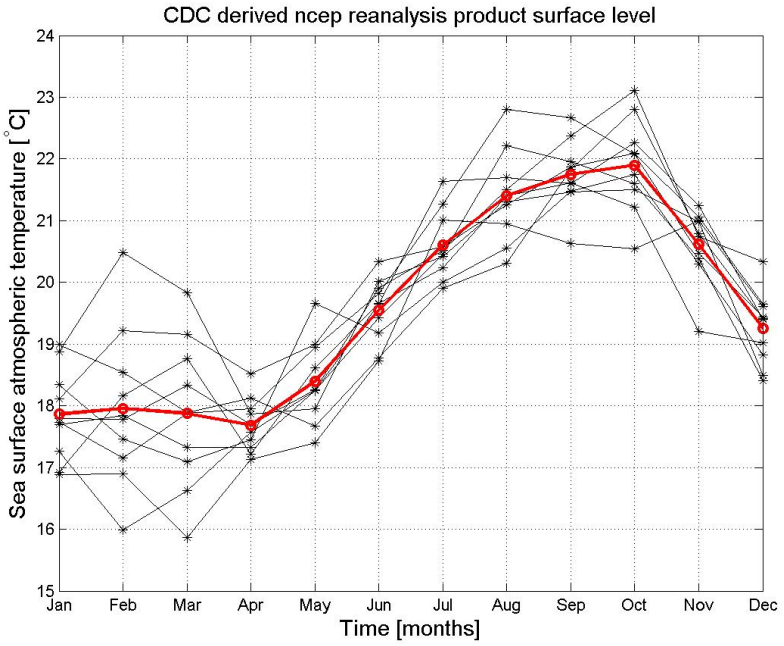

Figure 3.18: *NCEP sea atmospheric temperature.*

Computation

The computation of the surface net heat flux sensitivity to SST is based on the code written by Pierrick Penven (2002)[4] The three contributions to $dQ/dSST$ are on fig.3.19: the infrared contribution is nearly constant around $-6\,W\,m^{-2}\,°C^{-1}$; the sensible heat contribution varies slightly more, with highest values from June to August; the latent heat contribution is clearly the dominant term.

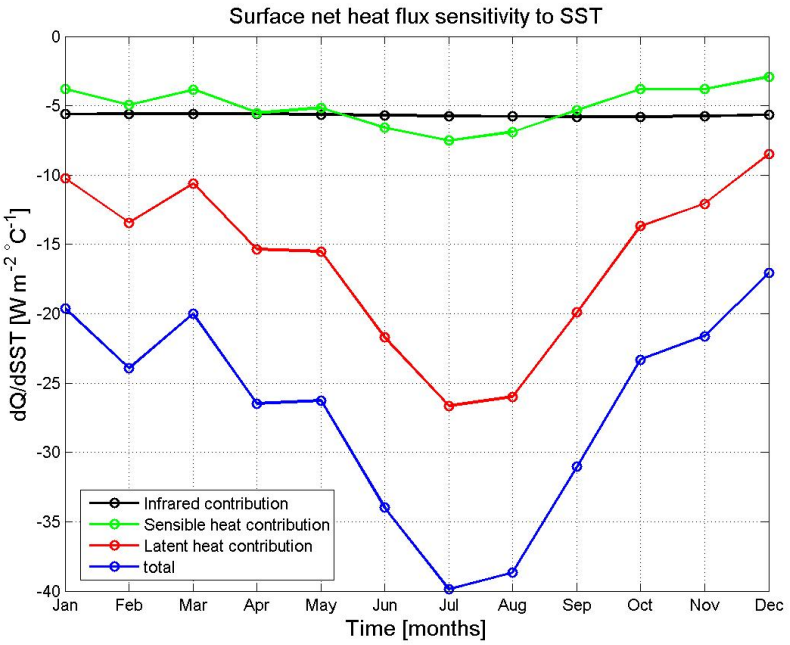

Figure 3.19: *Surface net heat flux sensitivity to SST.*

3.3.7 Summary

The resulting forcing file used in the following of this work is displayed here:

[4]ROMS-3D preprocessing tools.

Forcing file 3.1 Data for the simulation in the south of Gran Canaria.

```
LONGITUDE=  -15.500000   LATITUDE=    27.500000

SUSTR "surface u-momentum stress" "Newton meter-2"
    0.0295     0.0466     0.0155     0.0236     0.0236     0.0321
    0.0402     0.0370     0.0282     0.0243     0.0290     0.0195

SVSTR "surface v-momentum stress" "Newton meter-2"
    0.0391     0.0612     0.0512     0.0723     0.0714     0.0863
    0.1061     0.0877     0.0623     0.0421     0.0399     0.0187

SHFLUX "surface net heat flux" "Watts meter-2"
  -70.6000    -3.2900    57.8500    82.5500   118.0500   136.7200
  157.1700   152.5800   104.3200    34.3500   -48.2400   -66.6800

SWFLUX "surface freshwater flux (E-P)" "centimeter day-1"
    0.1010     0.0812     0.0805     0.0812     0.0758     0.0745
    0.0699     0.0637     0.0714     0.0772     0.0961     0.0978

SST "sea surface temperature" "Celsius"
   19.5280    18.9840    18.9380    19.2060    20.0870    21.1730
   21.7820    22.4550    23.1060    23.0210    22.1210    20.7360

DQSST "surface net heat flux sensitivity to SST" "Watts meter-2 Celsius-1"
  -19.6172   -23.9558   -20.0083   -26.4715   -26.2730   -33.9950
  -39.8760   -38.6577   -31.0458   -23.3095   -21.6306   -17.0639

SWRAD "solar shortwave radiation" "Watts meter-2"
  139.3200   178.0600   223.6300   249.7900   270.4800   267.2900
  258.6900   253.3500   234.4600   193.5900   149.3300   128.4700

UPWI "upwelling indice" "m3 s-1"
    0.00       0.00       0.00       0.00       0.00       0.00
    0.00       0.00       0.00       0.00       0.00       0.00
```

Summary

The numerous model parameters (physical, biological and running) are chosen according to the purpose of our simulations and to premilinary tests.

Initialization uses averaged vertical profiles from a cruise in the South of Gran Canaria, for temperature, salinity, nitrate and oxygen; constant values are assigned to the other variables.

Forcing is performed with 10-year averaged monthly data; when necessary, these data are spatially interpolated to provide values at the point of interest. Both wind stress and surface net heat flux reach their respective maximal value in July; the sea surface temperature varies from $18°C$ in February-March to $23°C$ in September-October.

Chapter 4

Model analysis and testing

4.1 Experiments with idealized forcing

The aim of this subsection is to compare the results yielded by the K profile parameterization (KPP) boundary layer model with other mixed-layer models, in cases of idealized forcing. These experiments will allow us to see if the model reacts well given these physical situations.

The models we want to make the comparison with are: the Mellor-Yamada level 2 (MYL 2) and level 2.5 (MYL 2.5) closures [Mellor and Yamada (1974)], the Niiler [Niiler (1977)], Garwood [Garwood (1977)] and Price (PWP) [Price et al. (1986)] models.

The first two belong to the category of differential models (see 1.4.3), i.e. they use the governing equation in their primitive form. The three other are based on integrated form of the equations; the mixed layer is defined as a region of uniform salinity and temperature.

4.1.1 Wind deepening experiment

In this case, mixing is done by the action of the wind on the surface by generation of turbulence.

Conditions of the experiment

The initial conditions are taken as follow: SST $= 24\,°C$, thermal stratification of $0.05\,°C/m$ and $u = v = 0$. The latitude is taken at $29.91°\,N$, which leads to a inertial period of 24 hours. The wind stress has a constant value $\tau = 0.4\,N/m^2$, the surface net heat flux are set to zero and the vertical resolution $\Delta z = 2\,m$.

For these tests, we have taken the following values for the parameters:

```
time=1.
tdays=0.
dt=60.
ntstart=1
ntimes=int((5.*86400.+0.001)/dt)
hmax=400.
theta_s=0.01
```

The weak value of θ_s is chosen to have a regularly spaced vertical grid. The forcing file we used for this experiment is reproduced bellow.

Forcing file 4.1 Wind deepening.

```
LONGITUDE=  -15.500000   LATITUDE=    29.910000

SUSTR "surface u-momentum stress" "Newton meter-2"
    0.4000     0.4000     0.4000     0.4000     0.4000     0.4000
    0.4000     0.4000     0.4000     0.4000     0.4000     0.4000

SVSTR "surface v-momentum stress" "Newton meter-2"
    0.0000     0.0000     0.0000     0.0000     0.0000     0.0000
    0.0000     0.0000     0.0000     0.0000     0.0000     0.0000

SHFLUX "surface net heat flux" "Watts meter-2"
    0.0000     0.0000     0.0000     0.0000     0.0000     0.0000
    0.0000     0.0000     0.0000     0.0000     0.0000     0.0000

SWFLUX "surface freshwater flux (E-P)" "centimeter day-1"
    0.0000     0.0000     0.0000     0.0000     0.0000     0.0000
    0.0000     0.0000     0.0000     0.0000     0.0000     0.0000

SST "sea surface temperature" "Celsius"
   24.0000    24.0000    24.0000    24.0000    24.0000    24.0000
   24.0000    24.0000    24.0000    24.0000    24.0000    24.0000

DQSST "surface net heat flux sensitivity to SST" "Watts meter-2 Celsius-1"
    0.0000     0.0000     0.0000     0.0000     0.0000     0.0000
    0.0000     0.0000     0.0000     0.0000     0.0000     0.0000

SWRAD "solar shortwave radiation" "Watts meter-2"
    0.0000     0.0000     0.0000     0.0000     0.0000     0.0000
    0.0000     0.0000     0.0000     0.0000     0.0000     0.0000

UPWI "upwelling indice" "m3 s-1"
    0.00       0.00       0.00       0.00       0.00       0.00
    0.00       0.00       0.00       0.00       0.00       0.00
```

Results

The table 4.1 shows the values of the MLD with different models. The KPP model yields results in agreement with the others models. In the figure 4.1 the comparison of the MLD in the wind deepeninig experiment with two different values of the critical Richardson number Ri_{cr}.

The diminution of Ri_{cr} makes the mixed layer less deep.

Model	MYL 2	MYL 2.5	Niiler	Garwood	PWP	**KPP**
MLD $[m]$	39	39	54	51	54	**42**

Table 4.1: *Mixed Layer Depth obtained with different models in the wind-deepening experiment.*

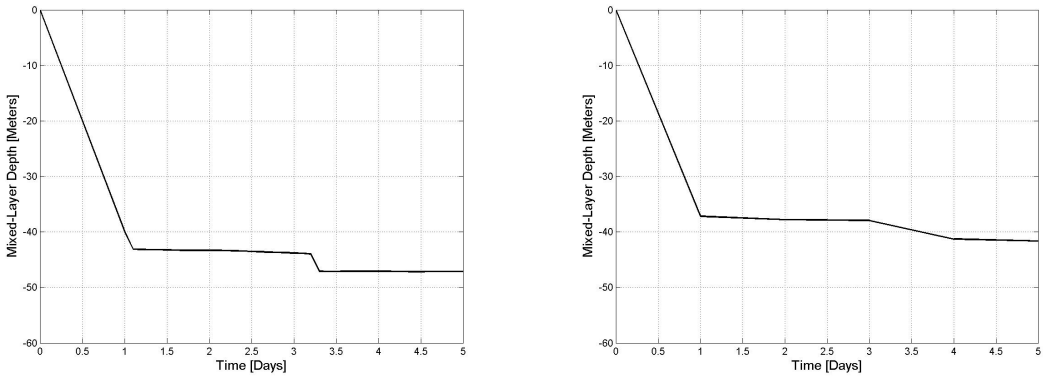

(a) $Ri_{cr} = 0.65$ (b) $Ri_{cr} = 0.25$

Figure 4.1: *Wind-deepening experiment.*

4.1.2 Cooling experiment

Here the mixing occurs because of convection: the water near the surface is cooled and tends to sink.

Conditions of the experiment

The initial conditions are the same as the previous experiment. For the forcing, we have: constant value $\tau = 0.1\, N/m^2$ for the wind stress and surface net heat flux of $-96.8\, W/m^2$. This experiment is run 120 days.

Results

Model	MYL2	MYL 2.5	Niiler	Garwood	PWP	**KPP**
MLD $[m]$	101	103	127	117	101	**110**

Table 4.2: *MLD obtained with different models in the cooling experiment.*

Forcing file 4.2 Cooling experiment.

```
LONGITUDE=  -15.500000   LATITUDE=    29.910000

SUSTR "surface u-momentum stress" "Newton meter-2"
    0.1000     0.1000     0.1000     0.1000     0.1000     0.1000
    0.1000     0.1000     0.1000     0.1000     0.1000     0.1000

SVSTR "surface v-momentum stress" "Newton meter-2"
    0.0000     0.0000     0.0000     0.0000     0.0000     0.0000
    0.0000     0.0000     0.0000     0.0000     0.0000     0.0000

SHFLUX "surface net heat flux" "Watts meter-2"
  -96.8000   -96.8000   -96.8000   -96.8000   -96.8000   -96.8000
  -96.8000   -96.8000   -96.8000   -96.8000   -96.8000   -96.8000

SWFLUX "surface freshwater flux (E-P)" "centimeter day-1"
    0.0000     0.0000     0.0000     0.0000     0.0000     0.0000
    0.0000     0.0000     0.0000     0.0000     0.0000     0.0000

SST "sea surface temperature" "Celsius"
   24.0000    24.0000    24.0000    24.0000    24.0000    24.0000
   24.0000    24.0000    24.0000    24.0000    24.0000    24.0000

DQSST "surface net heat flux sensitivity to SST" "Watts meter-2 Celsius-1"
    0.0000     0.0000     0.0000     0.0000     0.0000     0.0000
    0.0000     0.0000     0.0000     0.0000     0.0000     0.0000

SWRAD "solar shortwave radiation" "Watts meter-2"
  -96.8000   -96.8000   -96.8000   -96.8000   -96.8000   -96.8000
  -96.8000   -96.8000   -96.8000   -96.8000   -96.8000   -96.8000

UPWI "upwelling indice" "m3 s-1"
    0.00       0.00       0.00       0.00       0.00       0.00
    0.00       0.00       0.00       0.00       0.00       0.00
```

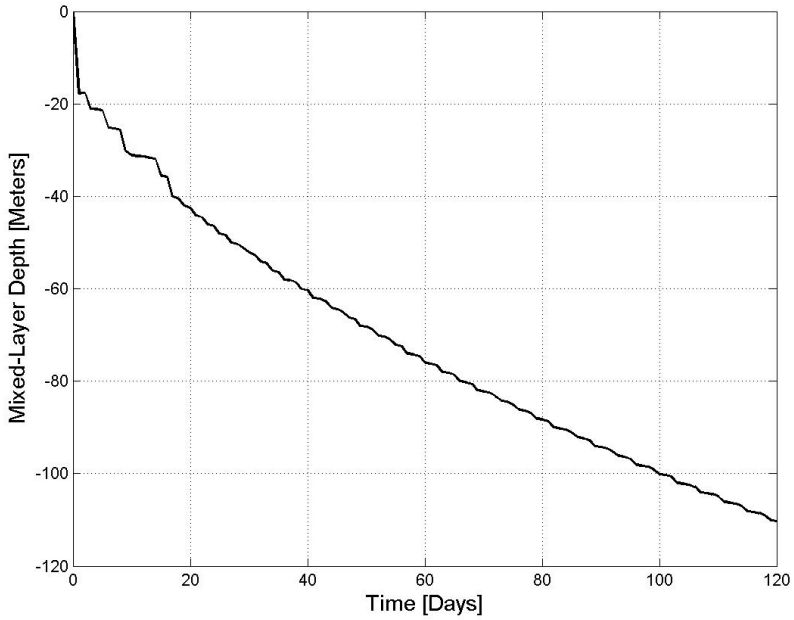

Figure 4.2: *Cooling experiment.*

4.1.3 Heating experiment

This experiment is done to show the stabilizing effect of heating.

Conditions of the experiment

The initial conditions are the same as the two previous cases, except that we do not take a thermal stratification: the initial temperature profile is constant at $19\,°C$. The wind stress has a value of $\tau = 0.1\,N/m^2$ and the net heat flux $290.4\,W/m^2$.

Forcing file 4.3 Heating experiment.

```
LONGITUDE=  -15.500000   LATITUDE=    29.910000

SUSTR "surface u-momentum stress" "Newton meter-2"
    0.1000     0.1000     0.1000     0.1000     0.1000     0.1000
    0.1000     0.1000     0.1000     0.1000     0.1000     0.1000

SVSTR "surface v-momentum stress" "Newton meter-2"
    0.0000     0.0000     0.0000     0.0000     0.0000     0.0000
    0.0000     0.0000     0.0000     0.0000     0.0000     0.0000

SHFLUX "surface net heat flux" "Watts meter-2"
  290.4000   290.4000   290.4000   290.4000   290.4000   290.4000
  290.4000   290.4000   290.4000   290.4000   290.4000   290.4000

SWFLUX "surface freshwater flux (E-P)" "centimeter day-1"
    0.0000     0.0000     0.0000     0.0000     0.0000     0.0000
    0.0000     0.0000     0.0000     0.0000     0.0000     0.0000

SST "sea surface temperature" "Celsius"
   19.0000    19.0000    19.0000    19.0000    19.0000    19.0000
   19.0000    19.0000    19.0000    19.0000    19.0000    19.0000

DQSST "surface net heat flux sensitivity to SST" "Watts meter-2 Celsius-1"
    0.0000     0.0000     0.0000     0.0000     0.0000     0.0000
    0.0000     0.0000     0.0000     0.0000     0.0000     0.0000

SWRAD "solar shortwave radiation" "Watts meter-2"
  290.4000   290.4000   290.4000   290.4000   290.4000   290.4000
  290.4000   290.4000   290.4000   290.4000   290.4000   290.4000

UPWI "upwelling indice" "m3 s-1"
    0.00       0.00       0.00       0.00       0.00       0.00
    0.00       0.00       0.00       0.00       0.00       0.00
```

Results

Model	MYL2	MYL 2.5	Niiler	Garwood	PWP	**KPP**
MLD $[m]$	14	14	4	14	8	**7**

Table 4.3: *MLD obtained with different models in the heating experiment.*

4.2 Sensitivity analysis

Our purpose in this section is to study the MLD behaviour when the forcing is modified. This is useful for several reasons:

1. to identify the parameters which influence the most the MLD;
2. to evaluate the impact of changes in the mean meteorological conditions: wind increase, temperature decrease etc ;

3. to examine if the model works well, according to what physics predict

We calculated the maximum, minimum and mean values of the MLD after perturbing the boundary conditions singly. The base file was the forcing file 3.1. The perturbations consisted in adding or subtracting 10 % at every monthly value of the tested forcing parameter. The numerical and graphical results are given in tab. 4.4 and fig. 4.3.

Here are the conclusions we can draw:

- An increase (decrease) in wind stress leads to a deepening (shallowing) of the mixed layer depth, as expected in theory and in agreement with the idealized experiments (section 4.1 page 50). These variations are weaker from October to February and the MLD maximum is nearly not affected.

- Increasing the surface net heat flux induced a general shallowing of the MLD, but the effets of variation of this parameter are noticeably weaker than those of the wind stress.

- The impact of freshwater flux variation are negligible, the mean relative variation being on the order of 0.05 %. Precipitations (evaporation) bring(s) less (more) salty waters at the surface; in a region with weak precipitation, the modification of the freshwater flux has little impact.

- Sea surface temperature perturbations provoke strong changes in the MLD, mostly in winter, where the MLD maximum undergoes variation between -14 (SST increase) and $+26$ percent (SST decrease). To explain these significant modifications, we have to keep in mind the role of the SST: it is used to modify the surface net heat flux so that the resulting surface temperature is equal to the SST.

  Combined with the mean value of surface net heat flux sensitivity to SST around $27\,W/m^2\,°C$, the $\pm 10\%$ perturbation of the SST ($\approx \pm 2°C$) causes a significant change of the surface net heat flux which is effectively applied in the numerical model (around $\pm 60\,W/m^2$).

- Modifying the surface net heat flux sensitivity to SST ($dQ/dSST$) do not have impact on the MLD. To understand this statement, we have to go back on the definition of this forcing parameter (see equ. (3.5) page 45): $dQ/dSST$ causes the model heat flux to differ from the heat flux from the data, the difference between the two flux being proportional to the difference between the computed temperature and the sea surface temperature.

  This difference has maximal value $\approx 0.6°C$, but the mean value is close to $0.2°C$. Combined with a $dQ/dSST$ mean value of around $27\,W/m^2\,°C$, the corresponding variation in the model heat flux less than to $6\,W$, a value insufficient to induce significant variations of the MLD.

- The rise of the solar shortwave radiation caused a deepening of the MLD, mostly in the period from June to October. This result is the opposite from what we had with the surface net heat flux. We expect to have a shallower MLD if the shortwave radiation is increased. To explain our observation, we first need to underline that this situation does not correspond to a physical reality: in this sensitivity analysis, we vary the forcing parameters one after each other, separately. Normally, by definition,

an increase of the solar shortwave radiation (`srflx`) requires an increase of the solar net heat flux.

Having a closer look into the code, we see that the MLD computation requires the knowledge of the buoyancy forcing `Bfsfc` as a function of depth. This buoyancy forcing is separated into two components: a surface buoyancy forcing `Bo` (without solar radiation) and a fraction `swdk` of surface shortwave radiation forcing `Bosol` penetrating to that depth. At a determined depth, the increase of `srflx` has the effect of diminishing the buoyancy forcing `Bfsfc`.

Further examination of the MLD computation shows that the `Bfsfc` decrease causes an increase of w_s, the turbulent velocity scale, which plays a role in the bulk Richardson number Ri_b (see eq. 2.25), by increasing its denominator. It is not straightforward to show that the diminution of `Bfsfc` results in a deepening of the mixed layer, as the bulk Richardson number depends on the MLD in a complicated way.

We performed additional runs to make sure that we get the same effects when the shortwave radiation is increased. To conclude, we can say that justifications are more numerical than physical.

Perturbated parameter		Mixed layer depth [m]					
		Minimum		Mean		Maximum	
		Value	Δ %	Value	Δ%	Value	Δ%
surface momentum stress	+10 %	25.57	10.29	56.83	2.53	108.02	-0.32
	-10 %	22.47	-0.66	54.08	-2.44	108.38	0.02
surface net heat flux	+10 %	22.65	-2.33	54.56	-1.57	108.18	-0.17
	-10 %	24.28	1.01	56.10	1.21	107.41	-0.88
surface freshwater flux	+10 %	23.18	-0.04	55.41	-0.05	108.37	0.01
	-10 %	23.20	0.01	55.45	0.03	108.36	-0.01
sea surface temperature	+10 %	20.88	-9.95	49.60	-10.51	93.17	-14.02
	-10 %	28.43	4.83	63.12	13.86	136.78	26.22
surface net heat flux sensitivity to SST	+10 %	23.38	0.82	55.38	-0.09	108.31	-0.05
	-10 %	23.03	-0.15	55.51	0.14	108.43	0.06
solar shortwave radiation	+10 %	28.40	22.48	57.71	4.11	108.89	0.49
	-10 %	21.24	-1.80	53.75	-3.04	107.51	-0.79
reference		**23.19**	0.00	**55.43**	0.00	**108.36**	0.00

Table 4.4: *Sensitivity analysis: minimal, maximal and mean values of MLD for perturbed boundary conditions. Δ stands for the relative variation with respect to the reference results (last line).*

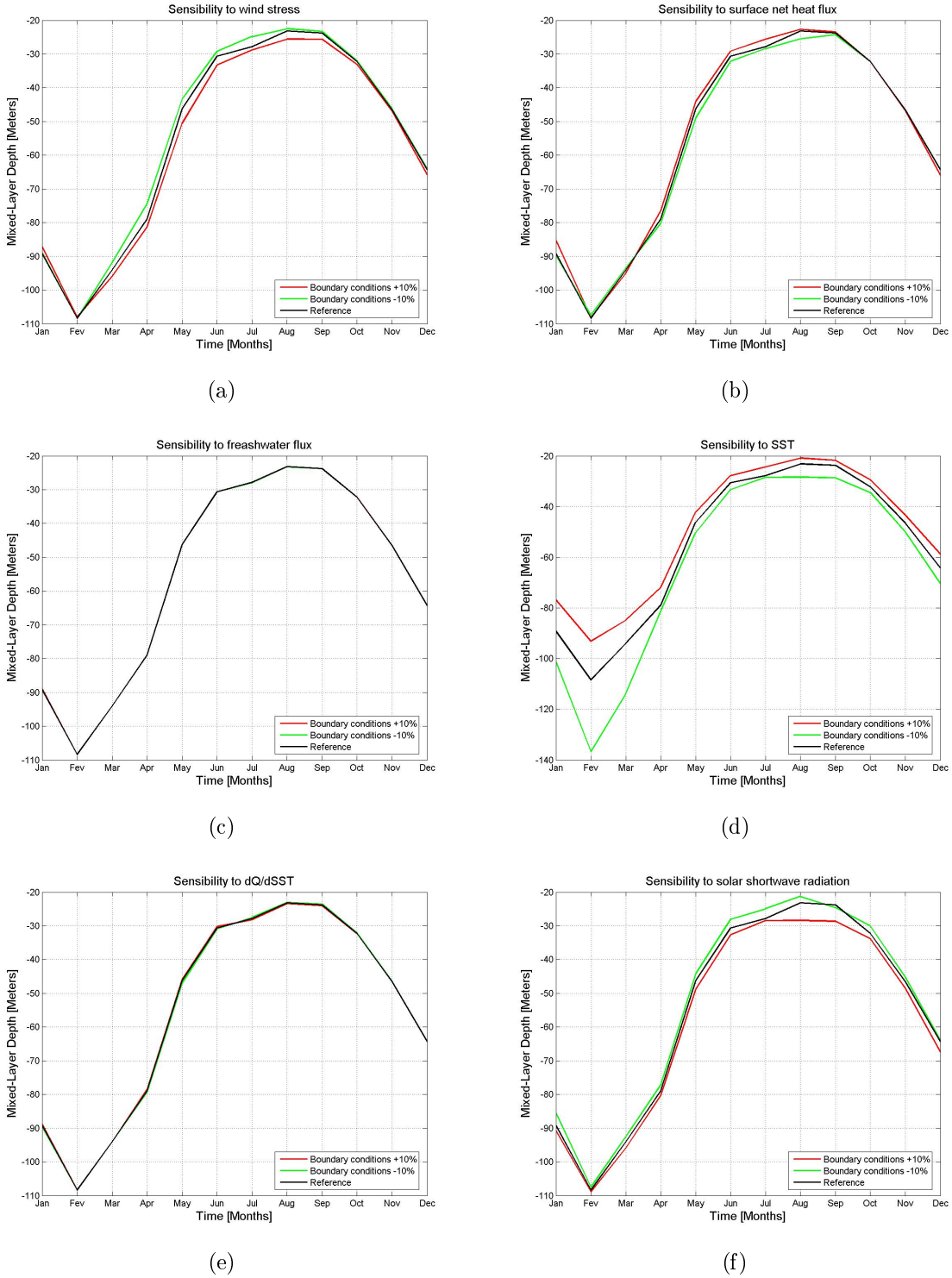

Figure 4.3: *Sensitivity to the forcing parameters: (a) wind stress, (b) surface net heat flux, (c) surface freshwater flux, (d) sea surface temperature, (e) surface net heat flux sensitivity to SST, (f) solar shortwave radiation. In black are the MLD's computed with the reference boundary conditions; in red and green are MLD's with boundary conditions increased and decreased of 10 percent, respectively.*

Summary

The model behaviour is tested with two ways: idealized experiments and sensitivity analysis. Results are compared with other mixed layer models.

In the first case, the experiments consists of simulating the mixed layer with idealized forcing, that is to say with conditions with which we can guess the results by basic reasoning: (a) constant wind stress acting on the water column, (b) cooling and (c) heating. The KPP scheme generates results in agreement with the other ones in each case.

The sensitivity analysis is then performed by perturbing the boundary conditions by adding or subtracting 10% to of a reference value, considering the forcing parameter one after each other. That analysis shows that the depth of the mixed layer is mostly sensible to the sea surface temperature (MLD mean value varying from $\pm 10\%$), the solar shortwave radiation (from $+4$ to -3%) and the wind stress ($\pm 2.5\%$).

Chapter 5

Numerical simulations

After describing the external forcing and the initial conditions needed by the model, we present and discuss the numerical experiments. Their results will then be compared with climatic and *in situ* data for their validation (chapter 6).

There are many ways to display the results given by the model, each of them having its own strong and weak points:

1. `contour plots`: they give a global representation of the variable evolution with respect to time and depth. Stratified and mixed zones are clearly detectable with the iso- lines (isotherm, isohaline, isopycnal, ... lines).

2. `depth profiles`: they provide an instantaneous view of the variable variation with depth and easily allow comparison with *in situ* data, as annual data are rarely available at the same location and at all depth, so contour plots are not always useful.

3. `depth-integrated plots`: they consist in computing the total amount of a given variable contained in the water column. As each variable is known at determined depths, the integrated value is computed by linearly interpolating between two consecutive values (*trapezoidal rule*). This kind of plots is used for the biological variables and permits to quickly locate the bloom.

5.1 Physical variables

Physical variables directly provided by the model are: velocity components, temperature, salinity, and mixed layer depth. From them, we can deduce the density through the equation of state (2.9). We are particularly interested by the temperature and the mixed layer depth for their impacts on the biological dynamics.

5.1.1 Temperature

The significant features of the temperature field (fig.5.1) are:

- the maximum surface temperature around $23°C$, occurring from late August to mid-October, that is to say 2-3 months after the maximal value of the net heat flux;
- a deeper mixed layer from February to May due to strong convective mixing ;
- the surface minimum temperature around $18°C$ from February to May, resulting from the loss of energy by the ocean (negative net heat flux);
- the strong stratification in late summer, under the influence of the strong solar heating, which has a stabilizing effect on the water column (increase of the temperature near the surface, provoking a decrease of the density).

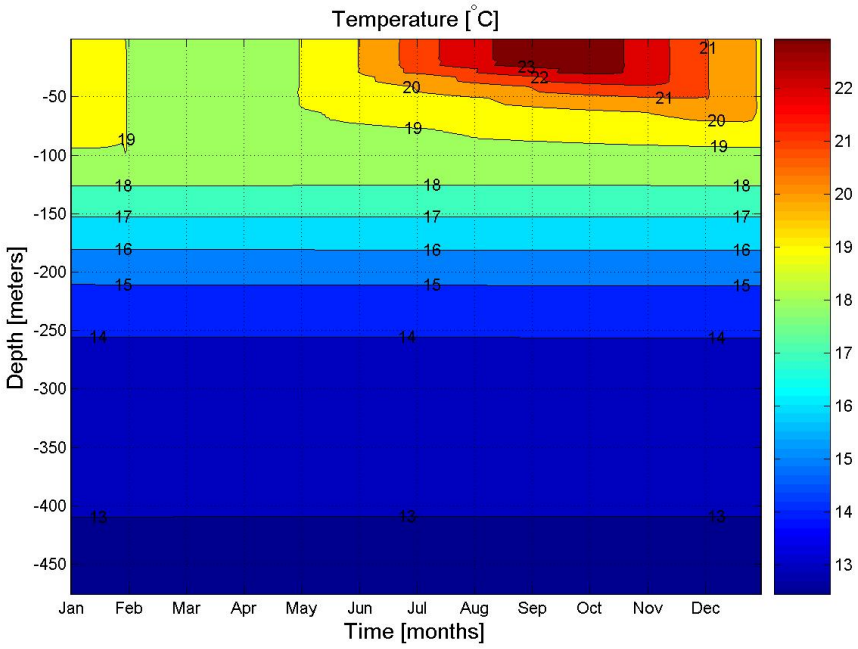

Figure 5.1: *Annual temperature field.*

We also computed the monthly-averaged profiles (fig. 5.2) to illustrate the evolution of the temperature field: from April-May we observe the formation of a seasonal thermocline, due to the effects of the important solar heating. The deepening begins in October-November, when the surface net heat flux becomes negative. The mixed layer depth undergoes overall variations from $100 - 110$ to $20 - 30$ meters.

Also note that the changes with respect to time are concentred in the layer between the surface and $-125\,m$, that is to say where the exchange with the atmosphere take place, a value slightly lower than the depth of $-200\,m$ given by [Pelegrí et al. (2005a)].

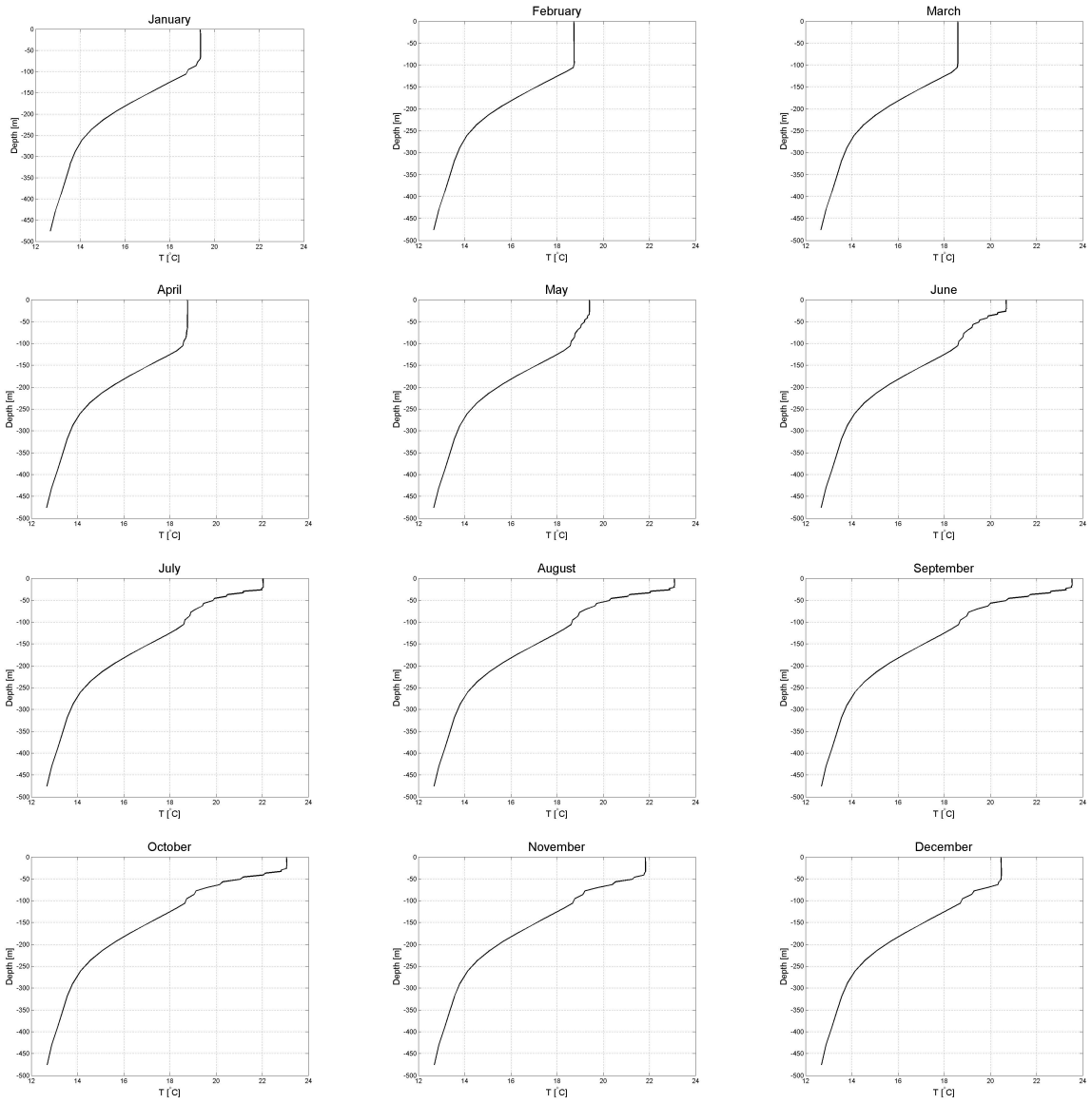

Figure 5.2: *Monthly-averaged profiles of temperature.*

5.1.2 Salinity

The salinity field (fig. 5.3) undergoes only weak variations throughout the year, because of the weak freshwater flux during the whole year. A stronger vertical gradient appears between 110 and 250 meters.

We also note the fact that higher salinity are found near the surface and lower near the bottom ($\frac{\partial S}{\partial z} > 0$), a situation favorable to salt-fingering and which may enhance the mixing process [Pérez et al. (2001)]. This salinity distribution is typical from subtropical regions, where the evaporation is enhanced by strong heating and wind in summer and the precipitations are weak through the year.

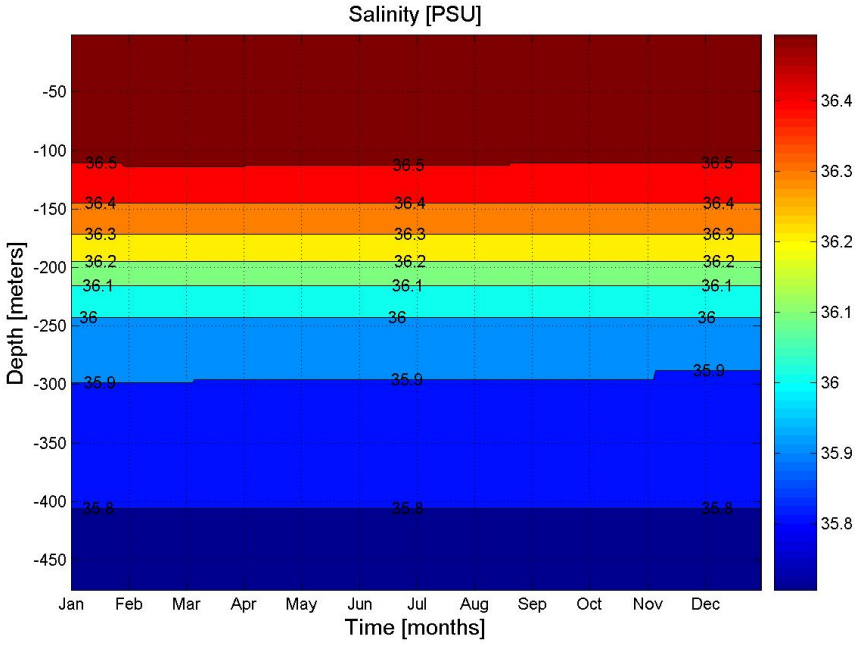

Figure 5.3: *Annual salinity field.*

5.1.3 Density

Once we know the temperature and the salinity, the water density (ρ) is easily computed by means of the state equation (2.9). We can consider the information brought by the density is redundant, but this variable is the one which is dynamically important. It also plays a role in the water column stability: the stratification is said to be stable when $\frac{\partial \rho}{\partial z} < 0$. Looking back to the turbulence closure scheme, we also see that ρ plays a role in the shearing instability, via the gradient Richardson number.

That is for these reasons that examine its variations (fig.5.4). The structure is very similar to the temperature: strong mixing around March, strong stratification in late summer, with a minimal value of density. This similarity is due to the fact that the salinity does not undergo important change with respect to time (fig.5.3), then density evolution is mainly driven by the temperature structure.

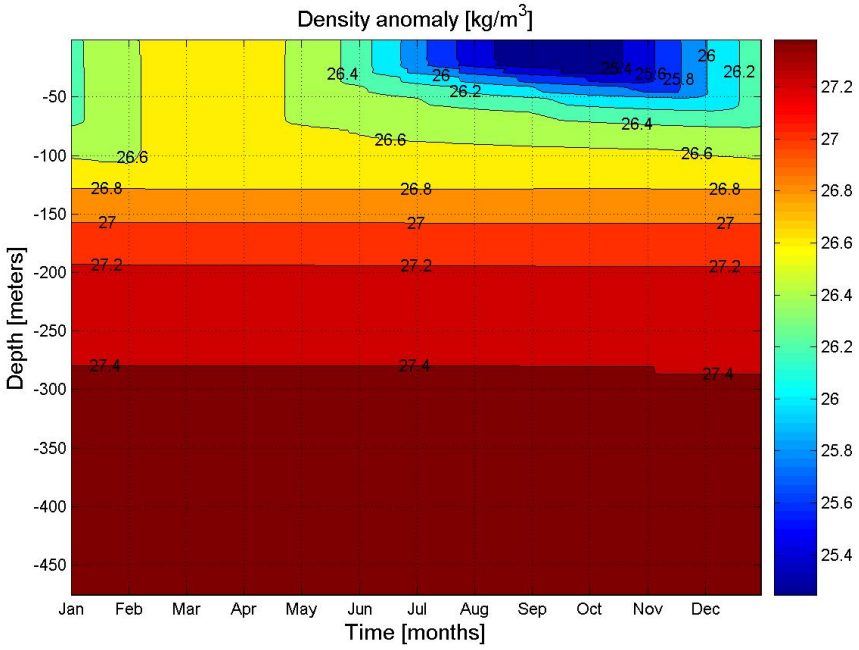

Figure 5.4: *Density anomaly field.*

5.1.4 Mixed layer depth

The mixed layer depth is a physical variable that has the asset of taking into account all the forcing parameters (wind, surface temperature, precipitation, heat fluxes) and allowing predictions over the behaviour of the biological variables. For these reasons, it can be considered as the key-parameter in this chapter.

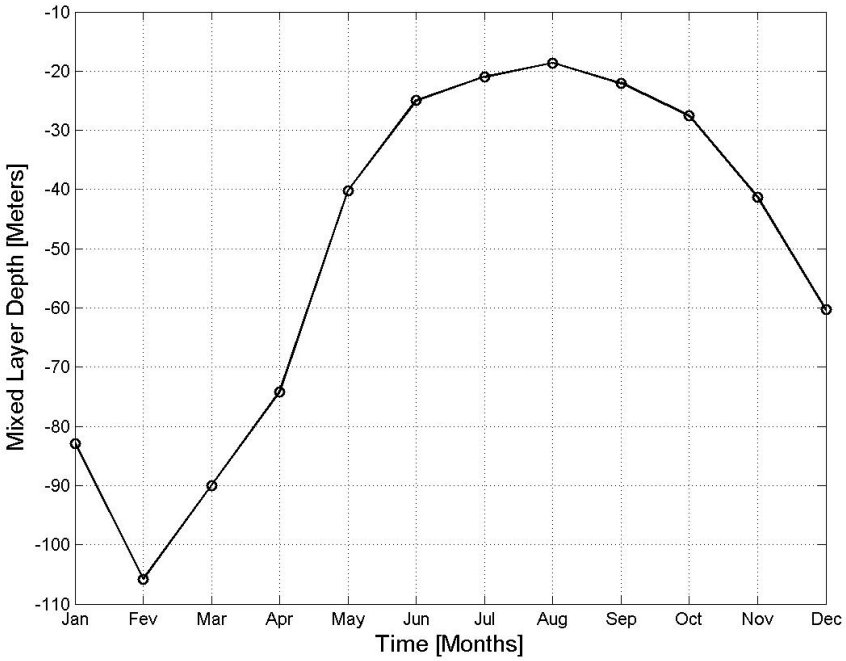

Figure 5.5: *Monthly-averaged MLD.*

The yearly cycle can be summarized in this way:

- in winter, when the surface net heat flux is negative, *i.e.* when the ocean loses heat, the MLD undergoes a deepening due to convection. The maximal depth is reached in February, at approximately 110 meters.
- from late winter to early summer, the MLD becomes shallower under the effect of the positive net heat flux. This period is also characterized by moderate trade winds.
- in summer, we have a competition between two antagonist processes: deepening due to the strong tradewinds and shallowing induced by the solar heating. Note that wind stress and net heat flux reache both their maximal value in July. During this period, the MLD conserves a value between 20 and 30 meters.
- between September and October, the deepening of the mixed layer starts because of the convective mixing. The mixing is more and more intense as the solar heat flux becomes more negative.

The situation described above shows an interesting difference with temperate regions, where winter cooling coincides with strong winds. The conjunction of a negative heat flux with strong winds can sometimes lead to situation where the water column is completely mixed.

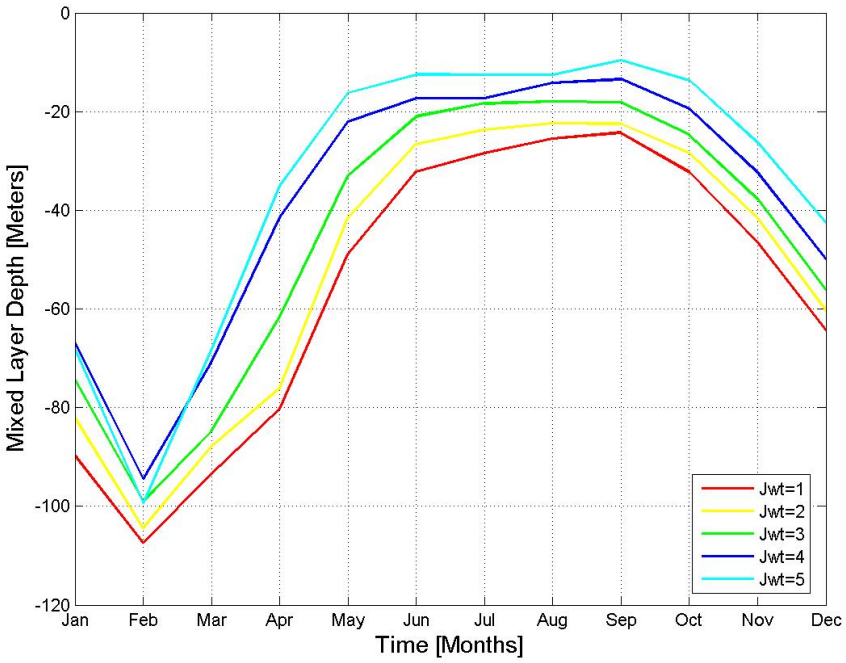

Figure 5.6: *Mixed depth layer for different Jerlov water type.*

5.1.5 Velocity

As we have seen in section 2.1, the velocity components are modified by the Coriolis force, the horizontal diffusion and the surface wind stress. If $\mathbf{u_h}$ stands for the horizontal velocity vector, we have

$$\frac{\partial \mathbf{u_h}}{\partial t} = f\,\mathbf{e_z} \times \mathbf{u_h} + \frac{\partial}{\partial z}\left(K_M \frac{\partial \mathbf{u_h}}{\partial z}\right),$$

with the boundary condition

$$K_M \frac{\partial \mathbf{u_h}}{\partial z} = \boldsymbol{\tau}_{surf}.$$

As the model is one-dimensional, there is no advection, so we may expect velocities different from measured values. However, the order of magnitude of surface velocity is around $0.05\,m/s$, in agreement with values of reported geostrophic speeds in the region (section 1.2). We obviously find the greatest velocity in summer, when the wind stress is the most intense.

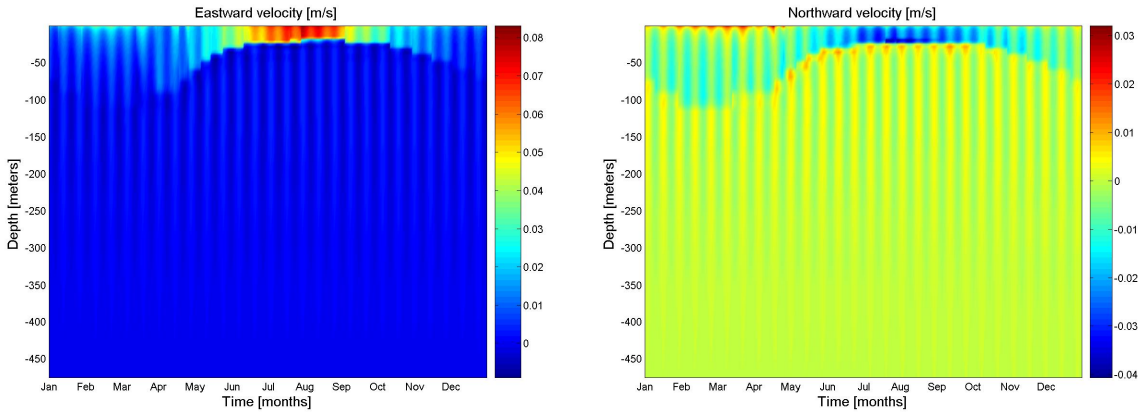

(a) Eastward component

(b) Northward component

Figure 5.7: *Velocity components.*

5.2 Biological variables

5.2.1 Nitrate

Nitrate is an important biological variable, as it is the nutrient that drives the new production. It is essential to accurately model the nitrate cycle as it will drive the other variable evolution.

As with the salinity, nitrate does not show significant variation with respect to time. What appears more clearly on the monthly averaged profiles (fig. 5.9) are the variations of the nitrocline depth, similar to those of the thermocline. We can observe that between January and February, a deepening of the nitrate mixed layer take place, the latter varying from -75 to -100 meters.

Another way of giving rise study the variations of a biological variable consists in integrating the variable over the water column depth, *i.e.* computing the total quantity of the considered variable contained in the water column (fig.5.10). A diminution of the nitrate quantity starts in February and ends in late March, meaning that during this period, the nutrient NO_3 is consumed by phytoplankton.

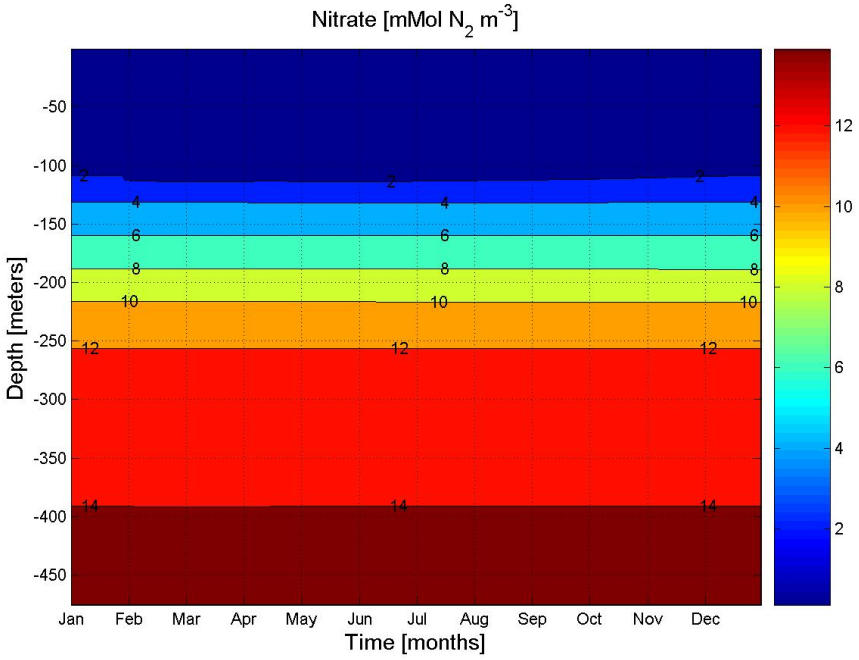

Figure 5.8: *Annual nitrate field.*

5.2.2 Phytoplankton

The variations of phytoplankton concentrations occur in the upper 150 meters of the layer, so we decide to concentrate only on this zone. At depths under 150 meters, the concentrations are quasi null. This can be explained by the fact that organisms like phytoplankton need light to grow, and light quickly decrease with depth.

Fig. 5.11 shows the strongest concentrations of phytoplankton occurring in February. As we have seen in the biological model, the phytoplankton growth is mainly driven by new and regenerated productions, or in other words, by nitrate and ammonium. This suggests that in February, when the phytoplankton concentration is maximal, a supply of nutrients is done in the upper layer of the ocean. That is what we will try to show in the following.

We can draw the same conclusions with fig. 5.12, where the concentrations were integrated over the whole water column ($500\,m$). Note that integrating over the 150 upper meters would have given the same results, as phytoplankton is quasi inexistent bellow that depth.

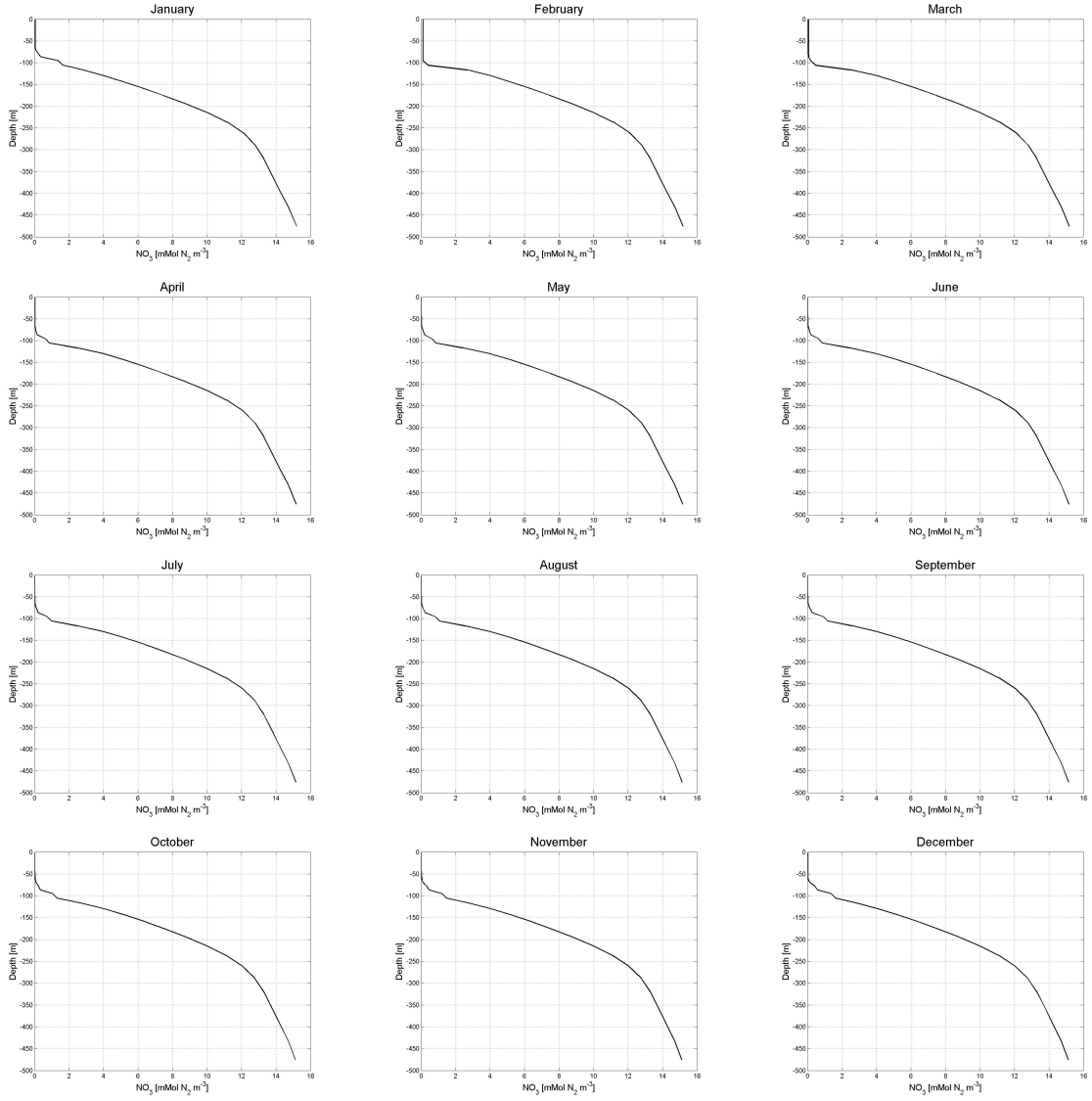

Figure 5.9: *Monthly-averaged profiles of nitrate.*

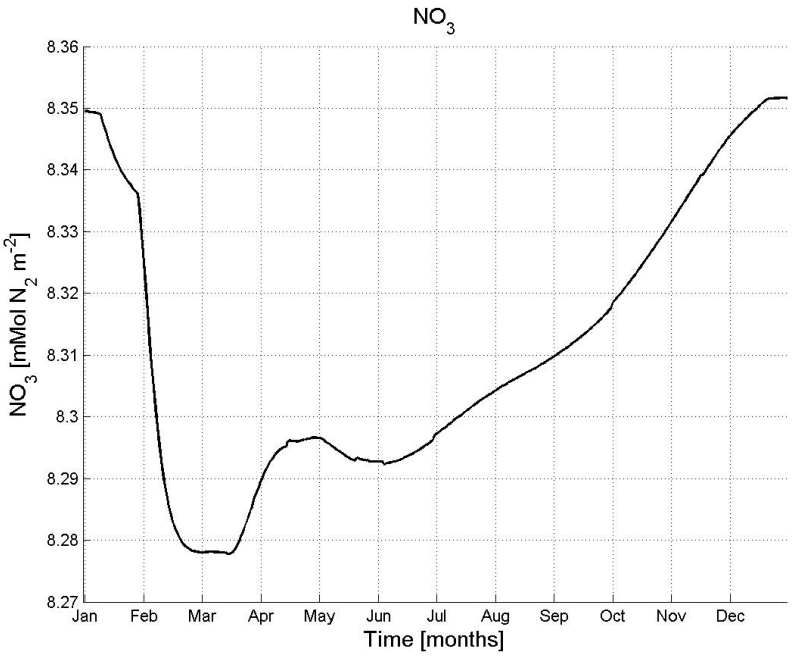

Figure 5.10: *Depth-integrated NO_3 concentration.*

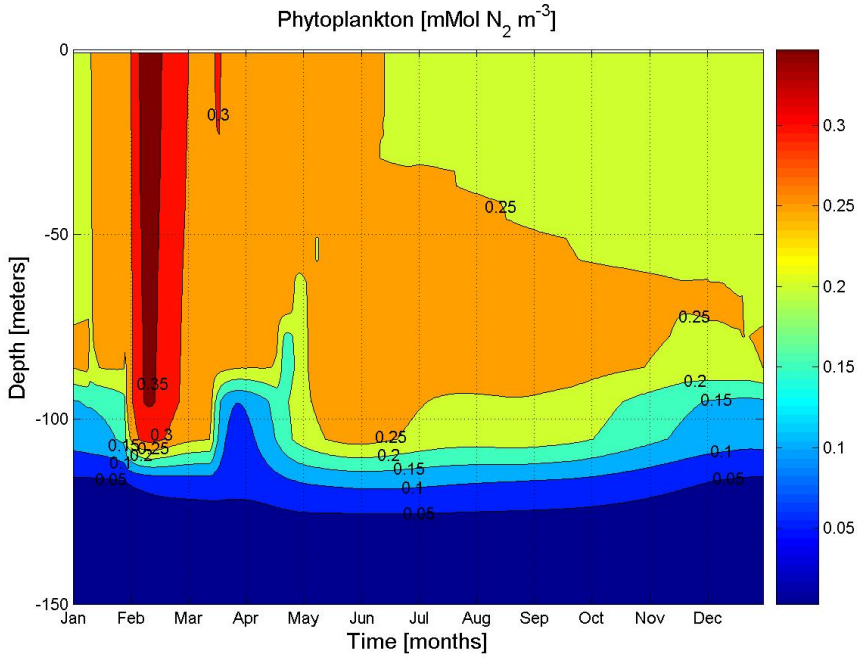

Figure 5.11: *Phytoplankton annual field.*

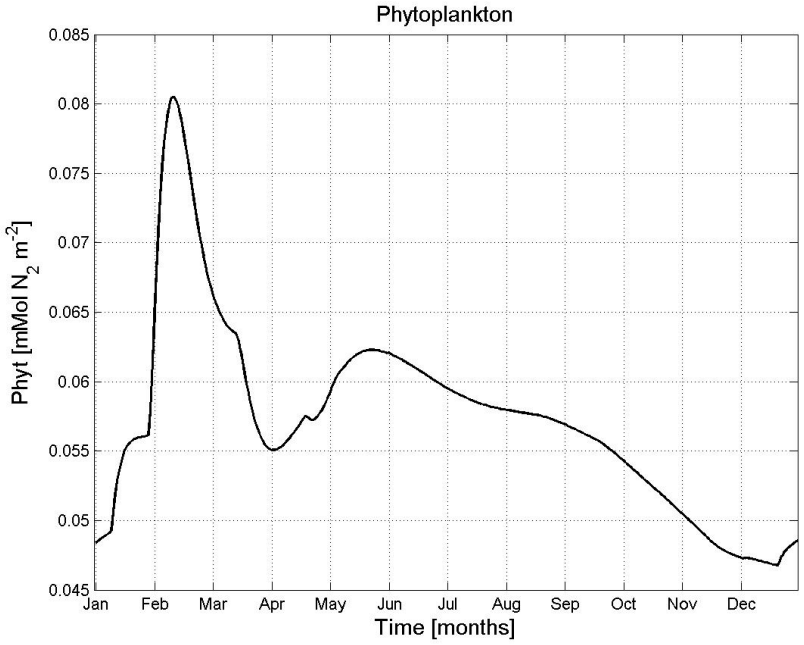

Figure 5.12: *Depth-integrated phytoplankton concentration.*

5.2.3 Zooplankton

The biological model indicates that the zooplankton grows with the grazing of phytoplankton but that its concentration may be reduced by its metabolism, decease or excretion. Therefore, we can expect it to be strongly dependent on the phytoplankton abundance.

On fig. 5.13, we see that the concentration starts to increase in February and reaches its maximum from mid March to late May. The major difference with the phytoplankton field is that the zooplankton bloom last during a longer period than the phytoplankton bloom. We assume that this is due to the fact that the phytoplankton bloom produced a sufficient quantity to feed the zooplankton for that period.

The integrated concentrations underline the strong increase from early February to mid March. After that period, the zooplankton production due to grazing weakens and its concentration starts to decrease under the effect of metabolism, decease and excretion.

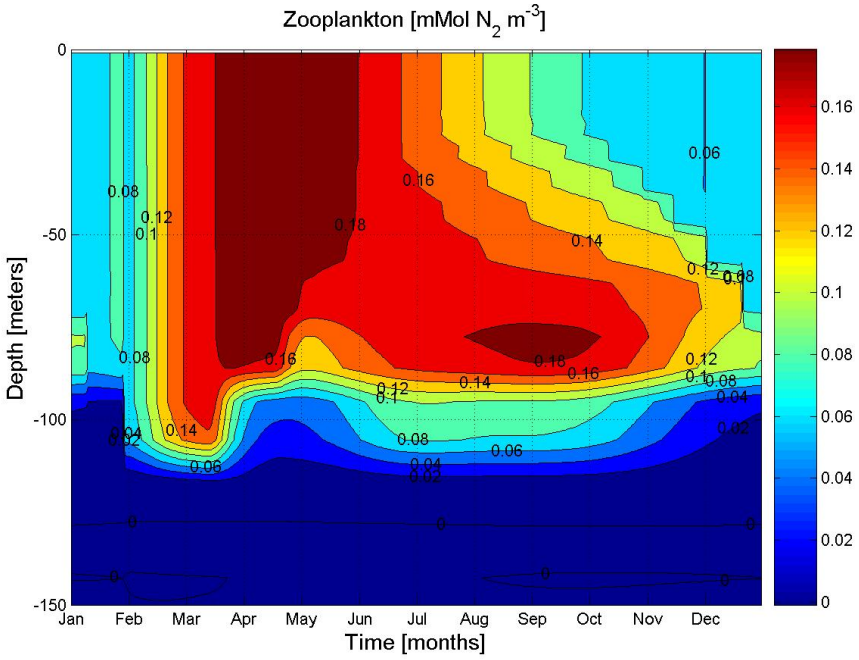

Figure 5.13: *Zooplankton annual field.*

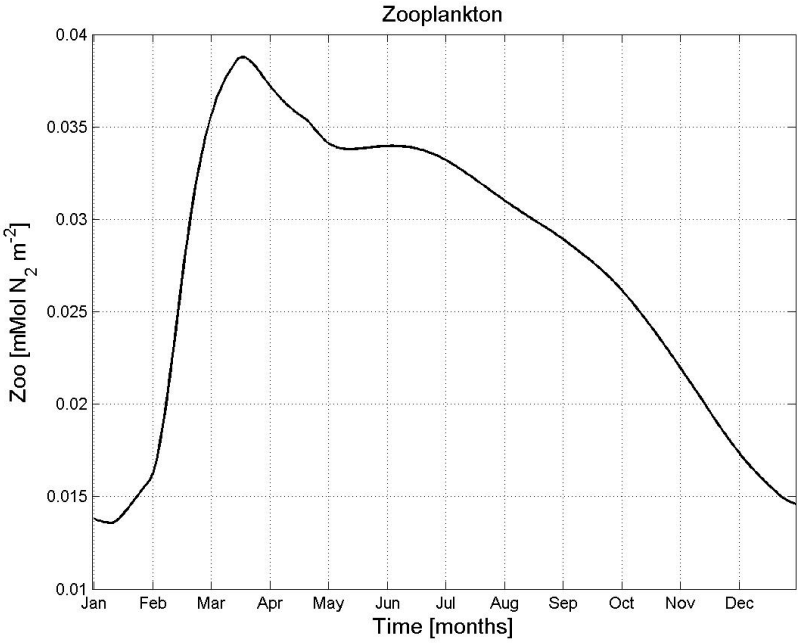

Figure 5.14: *Depth-integrated zooplankton concentration.*

5.2.4 Small detritus

The small detritus concentration (fig. 5.15) displays a maximum from February to November; until mid June, the layer of maximum concentration goes from 0 to - 100 meters, then the layer becomes thinner then which we can attribute to the vertical sinking.

Its variations are induced by the zooplankton grazing, and decease of phytoplankton and zooplankton, this is why it remains at its maximal value for a so long time.

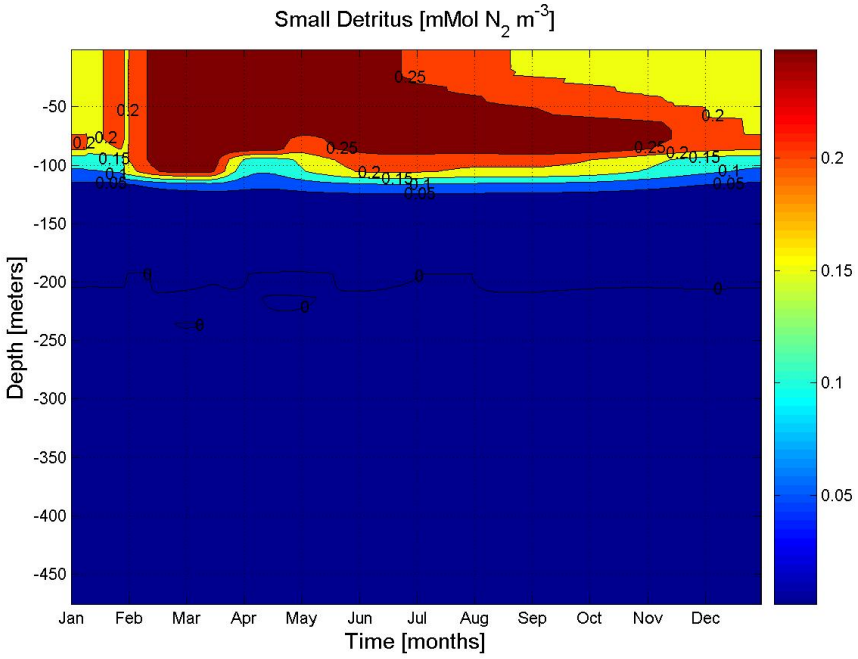

Figure 5.15: *Small detritus annual field.*

Large detritus

The only source of large detritus is the aggregation of small detritus with phytoplankton; the losses result of remineralization. The large detritus field (fig. 5.16) is similar to the one of the small detritus, except that its concentration is non zero at deeper levels (around $-300\,m$), certainly because of the vertical sinking, and that the region of maximum concentration is less extended: one possible explanation is that the aggregation requires both phytoplankton and small detritus to take place, and the phytoplankton concentration is maximal only during a short period.

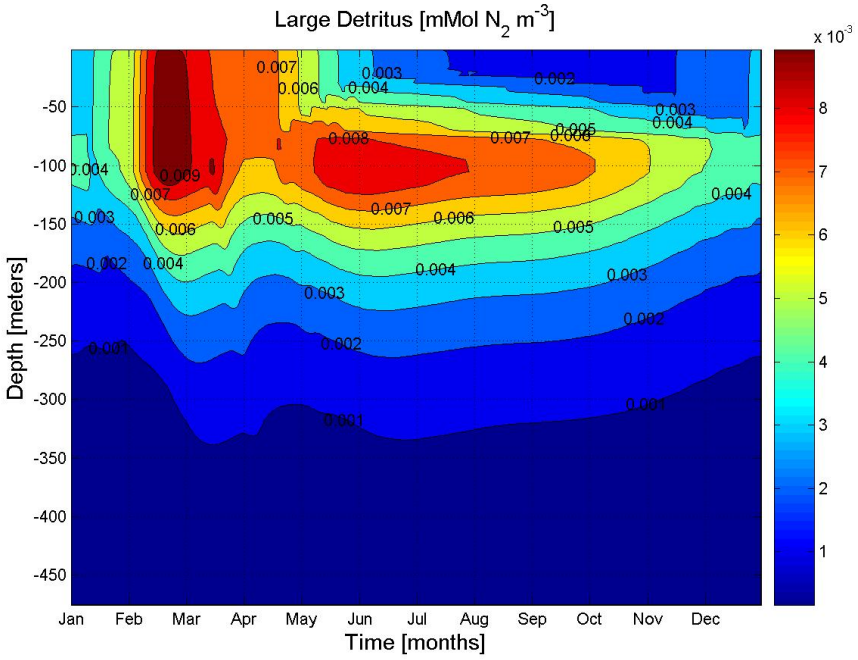

Figure 5.16: *Large detritus annual field.*

5.2.5 Ammonium

As we said in section 2.3.1, NH_4 is the nutrient that drives the regenerated production. Here are the observations we can make from fig. 5.17:

- a mixing (due to convection) from early February to late April, bringing NH_4 to surface,
- a maximal value around 100 meters almost all the year,
- strongest concentrations occurring in late March at 100 meters.

Referring to the biological model, we know that ammonium is generated only by excretion from zooplankton and is consumed by phytoplankton uptake, nitrification and remineralization. Comparing figs. 5.14 and 5.18, we note that the maximal integrated values occur nearly at the same time for the zooplankton and the ammonium.

The integrated concentration (fig. 5.18) indicates a minimum value in February, meaning that the quantity of nitrogen which is recycled at that period is very weak. We saw with the nitrate field that the new production is dominant in February.

5.2.6 Chlorophyll a

The chlorophyll structure (fig. 5.19) shows a homogeneous mixed layer of low chlorophyll above a deep chlorophyll maximum (DCM) fluctuating around $100\,m$ depth. According to [Basterretxea et al. (2002)], this unperturbed DCM can be understood in terms of steady-state balance between:

1. limitation of the phytoplankton production due to the light,

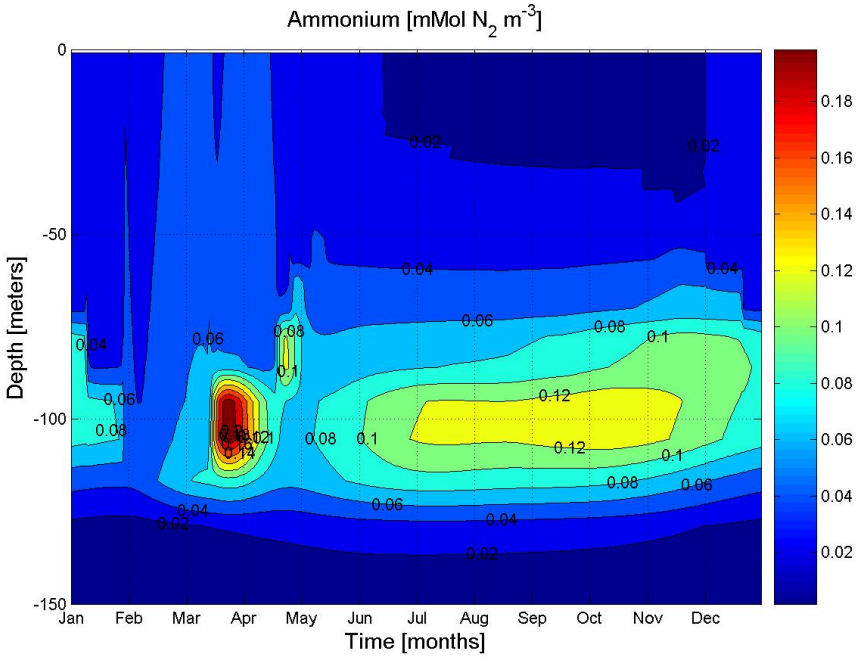

Figure 5.17: *Annual ammonium field.*

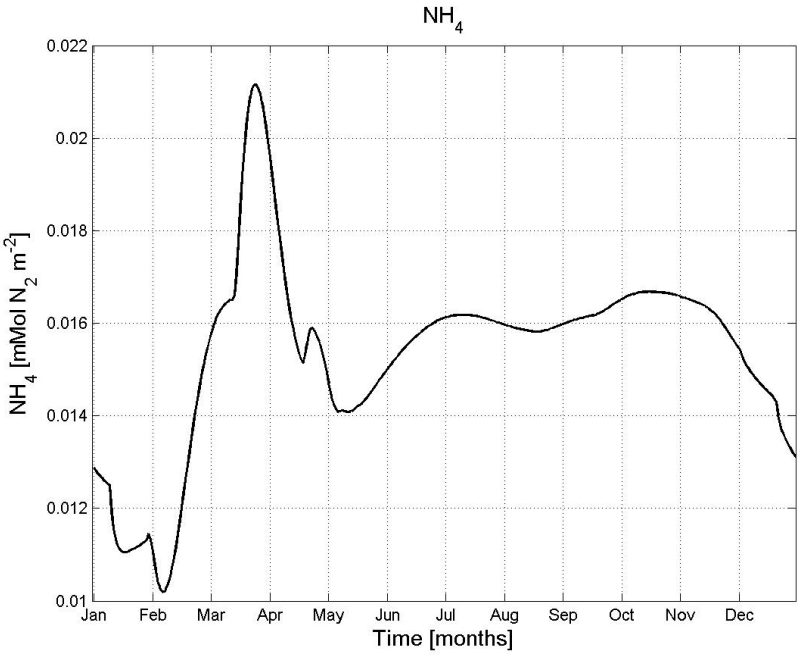

Figure 5.18: *Depth-integrated concentration of ammonium.*

2. losses due to exported production and the local metabolism of microplankton.

It is also interesting to compare figs. 5.18 and 5.20 which seems to show an evolution for the chlorophyll opposite to the one of ammonium: when one of these variables increases (decreases), the other decreases (increases). To understand this, we have to examine the biological model again: the expressions of new (eq. A.7) and regenerated (eq. A.8) productions show that a decrease of NH_4 will increase the new production (Q_{NP}) and increase the regenerated production (Q_{RP}). However, the variations of NO_3 have only influence on the new production, not on the regenerated one.

When $[NH_4]$ becomes high (mid March), Q_{NP} tends to zero and Q_{RP} tends to the unity, and we have a weak chlorophyll concentration. Inversely, when NH_4 has low concentrations (early February), Q_{NP}, proportional to $\frac{1}{[NH_4]}$, becomes significant, whereas Q_{RP} tends towards zero. Putting all together, we can say that the diminution of ammonium create a situation favorable to a strong chlorophyll concentration.

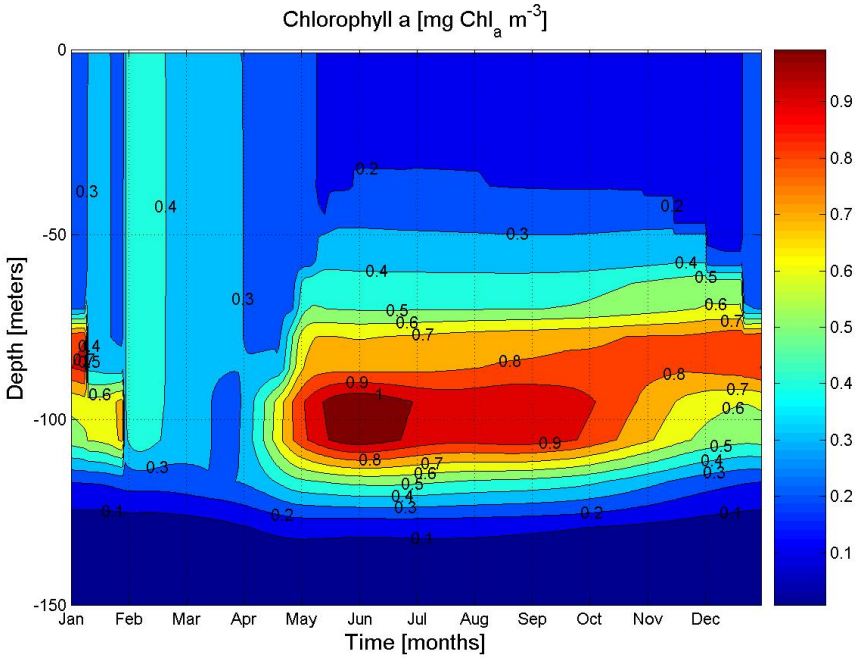

Figure 5.19: *Chlorophyll annual field.*

5.2.7 Oxygen

The oxygen is a variable that translates the global biological activity. It increases with phytoplankton, nitrate and ammonium concentrations. Fig. 5.21 shows that the horizontal variations are very weak bellow 150 meters. In the upper layer, we have strong concentrations from February to May near the surface, and from May to September, the region of maximal concentration is comprised between -50 and -100 meters, certainly because of the high zooplankton concentrations at those depths during that period (see fig. 5.13).

Fig. 5.22 shows a seasonal variation of the integrated oxygen concentration, with maximum in late winter, when the phyto- and zooplankton growth is important, and minimum in between October and December.

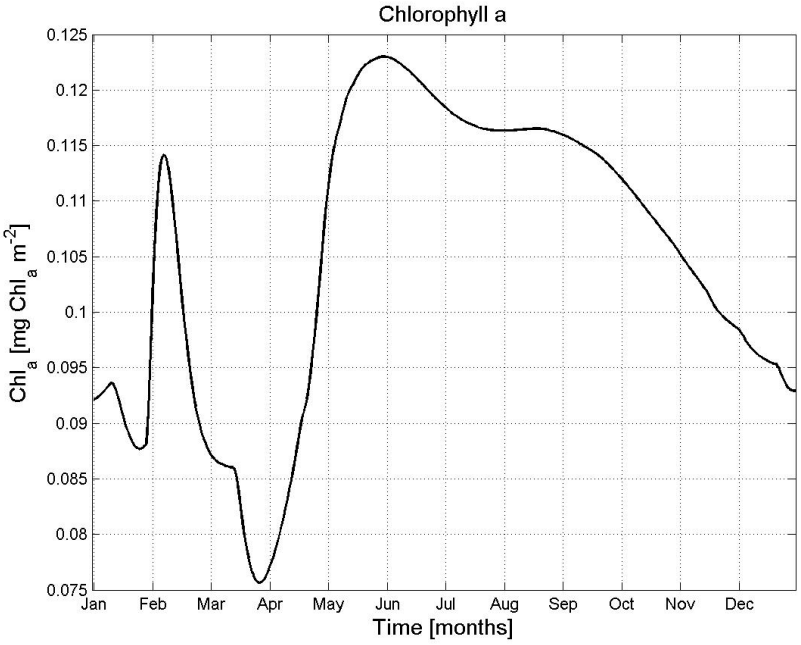

Figure 5.20: *Depth-integrated concentration of chlorophyll.*

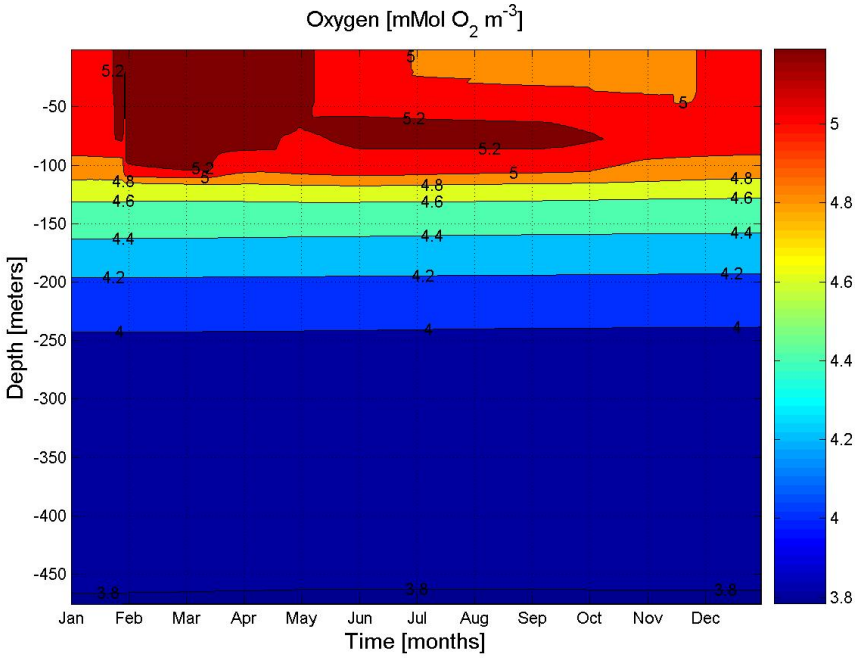

Figure 5.21: *Oxygen concentration annual field.*

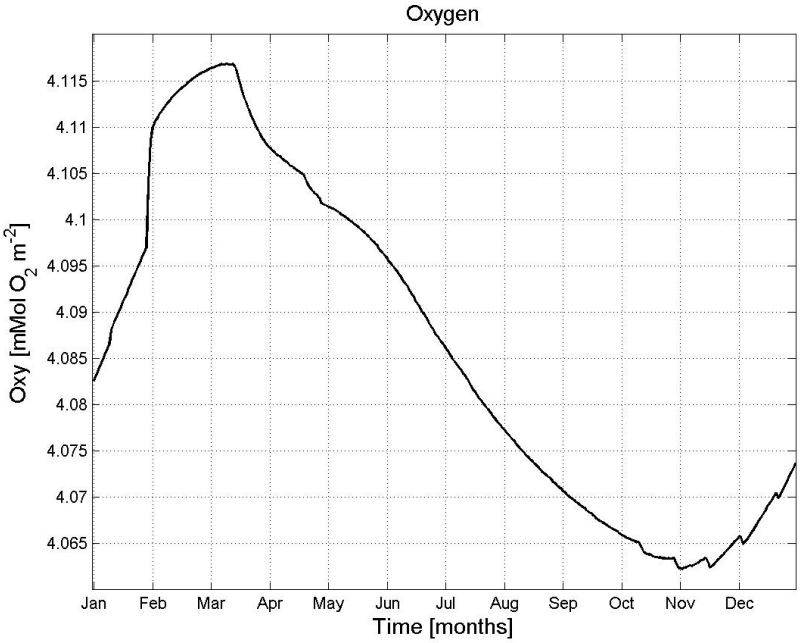

Figure 5.22: *Depth-integrated concentration of oxygen.*

5.3 Interpretation

Fig. 5.23 illustrates the dynamic of the biological variables: we integrated them over the euphotic depth (see section 5.3.2 for more details). We can see the succession of events: after the nutrients ejection (end of January) due to the mixed layer deepening, a phytoplankton bloom takes place (early February), followed by a zooplankton bloom (end of March).

Fig. 5.11 shows a phytoplankton bloom in February, when the mixed layer is deepest, but we also observe on fig. 5.23 that the phytoplankton maximum take places with a time delay ($\approx$ 10 days) with respect to the nutrients (nitrates) maximum. To interprete this time delay, we will appeal to Sverdrup's theory [Sverdrup (1953)]. Before that, we need to introduce some basic concepts of biological oceanography.

5.3.1 Radiation in the sea

When light passes through water, it undergoes absorbtion and scattering, resulting in an exponential decrease of the light intensity with depth. Different wavelengths penetrates to different depths: red light (around $650\,nm$) is quickly absorbed, with only about 1 % still remaining at 10 meters in very clear seawater; blue light (around $450\,nm$) penetrates deepest, with about 1 % remaining at 150 meters in clear water [Cognetti (2001)]. This light attenuation can be formulated as

$$\boxed{I_\lambda(z) = I_{\lambda,0} \exp(-k_\lambda z),} \tag{5.1}$$

$I_{\lambda,0}$ being the surface light intensity and k_λ the extinction coefficient, which depends on the wavelength of the light. Generally, eq. 5.1 is written without the λ subscripts,

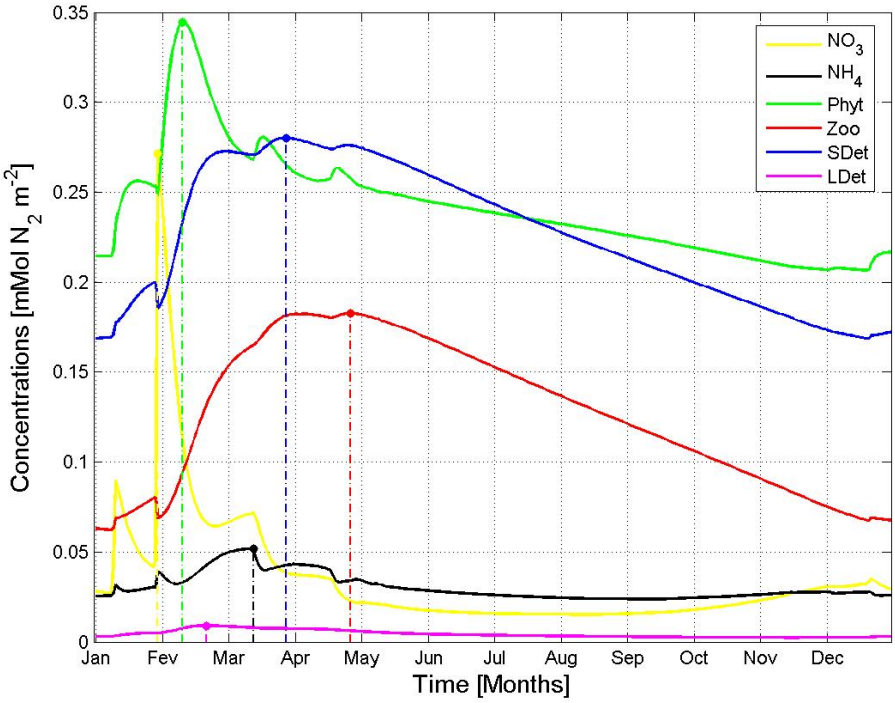

Figure 5.23: *Biological variables integrated over the euphotic depth.*

meaning that we work with mean light and mean extinction coefficient in the visible light the interval $[370, 720\,nm]$. The extinction coefficient can be calculated by measuring the radiation at a depth D and inverting the previous equation:

$$k = \frac{\ln[I_0] - \ln[I(D)]}{D}. \tag{5.2}$$

In our model, the light intensity variation with depth is given by the sum of two decreasing exponentials ([Paulson and Simpson (1977)] two wavelength bands solar absorption model):

$$I(z) = I_0 \left[r_1 \exp\left(\frac{z}{\mu_1}\right) + (1 - r_1) \exp\left(\frac{z}{\mu_2}\right) \right] \tag{5.3}$$

with the coefficients r_1, μ_1 and μ_2 dependent on the Jerlov water type (see table 3.1 and fig. 3.2).

5.3.2 The water column structure

Three zones can be defined according to the relative quantity of light that penetrates into the sea [Lalli (1993), Falkowski (1992)]:

the euphotic zone: it is the region where light is sufficient to support growth and reproduction of plants. In this zone, there is enough light for plant production by photosynthesis to exceed the loss of material that takes place through plant respiration.

the disphotic zone: in this zone, fish and some invertebrates can see but the light is too low for positive net photosynthesis (i.e. loss through respiration exceeds production by photosynthesis over 24 hours), but the presence of phytoplankton is still possible.

the aphotic zone: this region extends to the seafloor, and is characterized by the fact that the light intensity is too low to be detected by any biological system. This vast region does not support plant life, and is spatially removed from the initial link in the marine food chain.

Euphotic depth

The *euphotic depth* is defined as the depth where light intensity falls to 1 % its surface value, so it depends on the light attenuation in the water column. Typical euphotic depths vary from only several metres in turbid estuaries to around 200 metres in the open ocean.

5.3.3 Compensation depth

Let us concentrate our attention on the euphotic zone: here, the light is sufficient for production due to photosynthesis to exceed loss through respiration. The *compensation light intensity* is defined as the amount of light that makes production and loss equal; the *compensation depth* is the depth at which that equality is satisfied.

Using the previous definition and the formula (5.2), the compensation depth is calculated by

$$D_c = \frac{\ln(I_0) - \ln(I_C)}{k}, \tag{5.4}$$

where k is calculated from (5.2) assuming a wavelength of $550\,nm$. If $z < D_c$, photosynthesis still occurs, but in that case the net production is negative, that is to say respiration overcomes production.

5.3.4 Relation between irradiance and production

The relation between I, the light intensity and P, the production, also called the *P-I curve*, exhibits the following characteristics:

- when I is weak, there is a linear relation between them;
- when I is increased, P does the same, but more and more slowly;
- at a value I_{max}, called *saturation intensity*, P reaches its maximal value P_{max}, *i.e.* the maximal production;
- for $I > I_{max}$, P remains constant.

5.3.5 Sverdrup theory

More than 50 years ago, Sverdrup developed a model to explain the spring bloom of phytoplankton and the necessary conditions. His theory says that phytoplankton growth season starts in early spring when the mixed layer depth becomes shallower than the

critical depth. Critical depth or Sverdrup's critical depth is defined as the depth above which the depth-integrated daily gross primary production equals respiration, *i.e.* the depth above which integrated net daily primary production equals zero [Nybakken (2001)].

We have to keep in mind the hypothesis under this theory:

1. phytoplankton cells are uniformly distributed in the mixed layer,
2. photosynthesis is assumed to decrease exponentially with depth, as the light does,
3. respiration is considered to be constant over the mixed layer.

Figure 5.24 summaries the different depth we defined in this section.

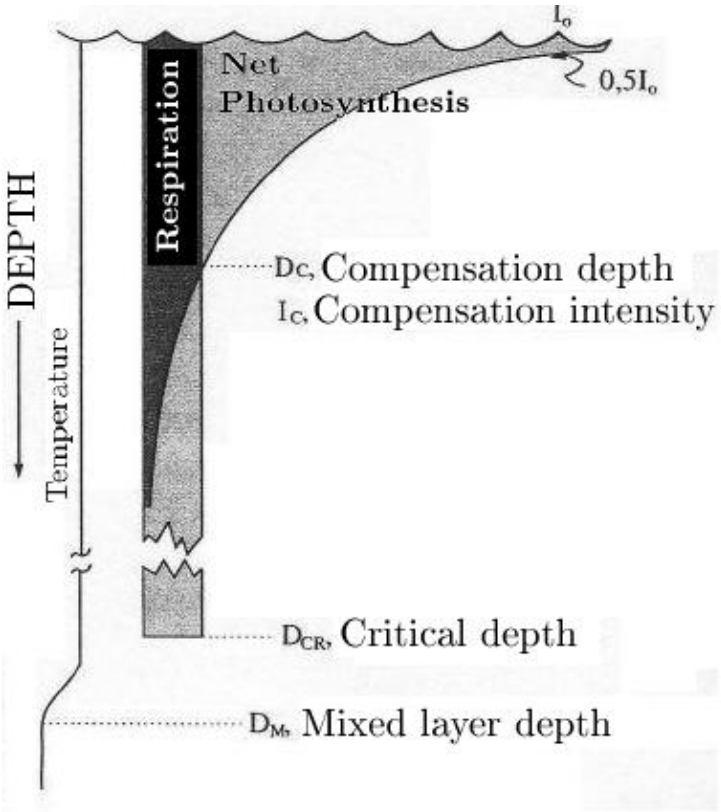

Figure 5.24: *Critical depth, compensation depth and mixed layer depth.*

Critical depth computation

In order to test the Sverdrup theory, we need a way to calculate the critical depth. In the surface layers of the sea, where mixing takes place, it is useful to work with an average value of light $\bar{I}_D$ penetrating into the euphotic zone. This average amount of light is obtained by integrating eq. 5.1 from the surface ($z = 0$) to the depth D, which leads to

$$\bar{I}_D = \frac{\bar{I}_0}{kD}(1 - e^{-kD})$$

The previous expression can be exploited to get an expression for the critical depth D_{cr}: phytoplankton cells move up and down in the mixed layer and get a mean light intensity $\bar{I}_D$. The depth at which $\bar{I}_D$ equals I_C is the critical depth.

Substituting $\bar{I}_D$ by the compensation light intensity I_C, we find

$$\boxed{D_{cr.} = \frac{\bar{I}_0}{k\, I_C}\left[1 - \exp(-k\, D_{cr.})\right]} \tag{5.5}$$

Assuming that $k\, D_{cr} \gg 0$, (5.5) can be simplified to

$$D_{cr.} = \frac{\bar{I}_0}{k\, I_C}. \tag{5.6}$$

Compensation depth computation

The compensation depth depends on the clarity of water and thus varies over the world's oceans: the clearer the water, the greater the light penetrationand the deeper the compensation depth [Nybakken (2001)]. It can be deduced from (5.4) if the compensation intensity is known.

According to [Nybakken (2001)], the compensation depth is approximatively equal to the depth at which the intensity has been reduced to 1 % of the surface light intensity, *i.e.* the euphotic depth. Using eq. (5.3), the euphotic depth $D_{euph.}$ satisfies the relation

$$\left[r_1 \exp\left(\frac{z}{\mu_1}\right) + (1 - r_1)\exp\left(\frac{z}{\mu_2}\right)\right] = \frac{I(D_{euph.})}{I_0} = 0.01.$$

The computed values varies between 24.5 and $86\,m$ according to the Jerlov water type (tab. 5.1). As seen in section 3.1, we choose the Jerlov indice equal to 2, leading to an euphotic depth of $72.8\,m$.

Jerlov indice	Compensation depth (meters)
1	86.0000
2	**72.8000**
3	59.5000
4	43.9000
5	24.5000

Table 5.1: *Compensation depth for different Jerlov water types.*

Results

Using the approximation $D_C \approx D_{euph}$ and extinction coefficients k between to 0.025 and $0.040\,m^{-1}$, the critical depth is computed according to (5.6). Figure 5.25 shows plots of critical and mixed layer depth. According to the value of k, the two depths are equal at different time of year: increasing the value of k makes the intersection of the two curves occur later. This is easy to understand if we recall the eq. 5.6: the critical depth is proportional to k^{-1}.

Comparing figures 5.23 and 5.25, we observe a good agreement with the Sverdrup's theory for a value of k between 0.025 and 0.030: the phytoplankton bloom starts when mixed layer is shallower than critical depth. We worked with different values of k because we do not know its value with precision. Furthermore, k is not constant through the year,

as it depends on the presence of suspended particles in the water and on the chlorophyll concentration.

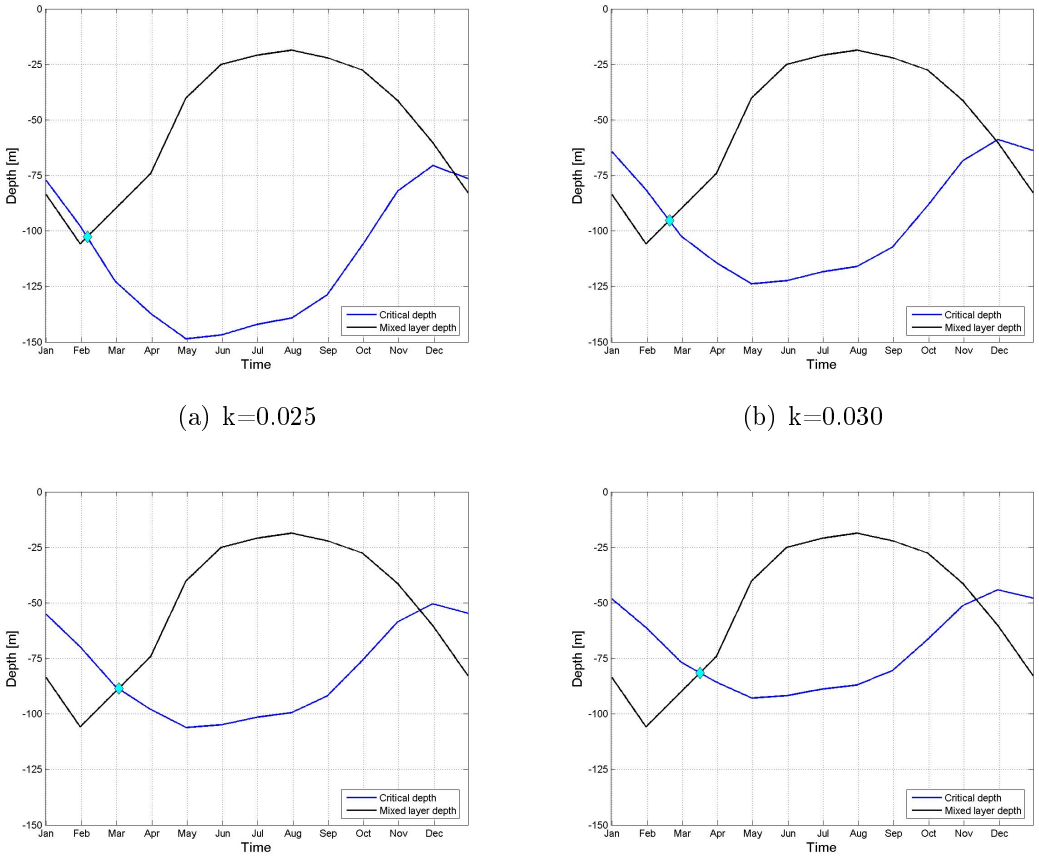

(a) k=0.025 (b) k=0.030

(c) k=0.035 (d) k=0.040

Figure 5.25: *Annual evolution of critical and mixed layer depths for different values of the extinction coefficient.*

To conclude this interpretation, we have to underline the limitations of our critical depth model:

- The substitution of the compensation depth by the euphotic depth: compensation light intensity from which compensation depth is normally deduced is somewhat different for different plankton species. Therefore a more elaborated model should be applied. A discussion about Sverdrup's Critical Depth Hypothesis and compensation depth computation can be found in [Siegel et al (2001)].
- The choice of a constant absorbtion coefficient: this coefficient is supposed to take into accound the effects (reflection, scattering) of the matter present in the water column, hence should depend on the chlorophyll concentration for instance.
- Light intensity as well as mixed layer depth used in the computation are monthly-mean values, then we cannot expect sharply exact results.

Despite all these limitations, Sverdrup's theory appears satisfying, as it provides a physical explanation to the numerical results.

Summary

The simulation results are analysed and discussed using the following representations: (a) time-depth contours, (b) depth-integrated variations and (c) monthly-averaged profiles.

The interesting features reproduced by the model are:

- for the physical variables: maximal temperature ($23°C$) from August to October, coinciding with the strongest stratification; minimal temperature ($18°C$) and maximal mixed layer depth in winter, under the effect of mixing by convection; increasing of salinity with depth (*salt fingering*); mixed layer depth varying from around $22\,m$ in summer, when both the wind and the solar heating are maximal, to $105\,m$ in February.

- for the biological variables: phytoplankton bloom in February, induced by the mixed layer deepening and the upward ejection of nutrients; deep chlorophyle maximum around a $100\,m$ depth during almost all the year.

The origin of the bloom is examinated in details, invoking the *Sverdrup critical depth*.

Chapter 6

Model validation

After the chapter dedicated to numerical results, we need to validate them to check if the model is able to reproduce real measured values. For the validation, we work with three kinds of data:

1. fields obtained from oceanic database, mainly from the NODC (Levitus) World Ocean Atlas (WOA) [1],
2. *in situ* data, originated from cruises to the south of Gran Canaria (FAX campaign in the present case [Barton et al. (2004)]),
3. data reproduced from publications.

6.1 Physical variables

6.1.1 Temperature

Our simulations [fig.6.1(a)] are well reproducing the maximal temperature around $22°C$ in the end of summer and the minimum surface temperature around $18°C$ in winter. The model also reproduces correctly the strong stratification and the development of the seasonal thermocline in summer and the winter convective mixing.

We observe difference in the value of the maximal temperature ($23°C$ in simulations against $22°C$ in the NODC data [fig.6.1(a)].

To understand the difference between our results and the data, we have to keep in mind the following facts :

1. We worked with a one-dimension model: there is no vertical velocity that could explain the deformation of the isotherms at higher depths.
2. Our simulations are performed with 10-years averaged data.
3. The point of simulations (27.5° North, 15.5° West) is slightly different from the location of the data.

[1] National Oceanographic Data Center
`http://www.nodc.noaa.gov/General/getdata.html`

4. Advection is not taken into account in the model, thus the influence of the Canary Current, which brings colder water from the north, cannot be modelled.

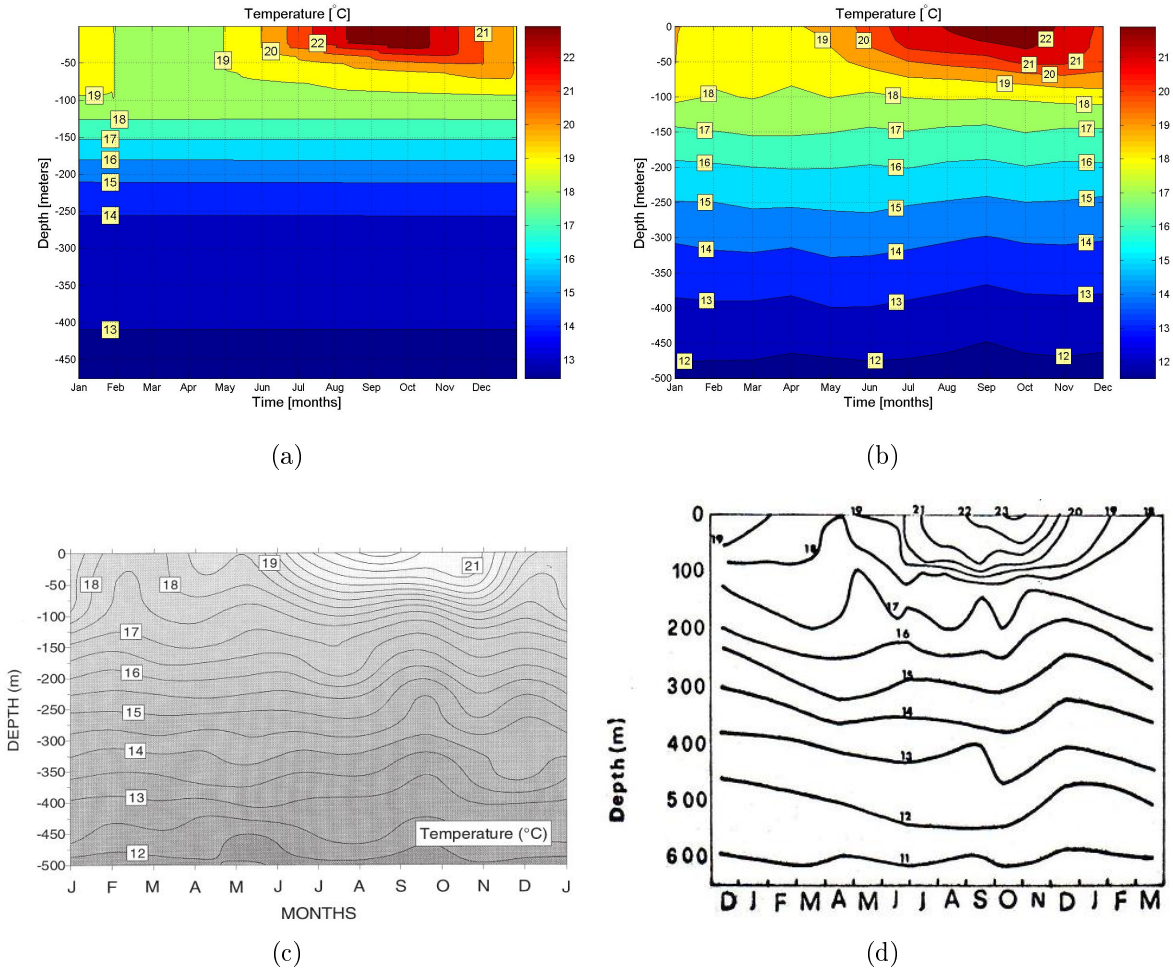

Figure 6.1: *Temperature contours: (a) Model results, (b) NODC (Levitus) WOA Monthly Long Term Mean temperature, (c) NODC archive for the area* $(29 - 31°N,\ 17 - 19°W)$ *(reproduced from [Barton et al. (1998)]), (d) measurements 5 miles East off Tenerife (reproduced from [Braun (1976)]).*

Temperature profiles

By observing the measured profiles (black lines), we can distinct three levels: the mixed layer $(0 - 25\,m)$, a region with a strong temperature gradient $(25 - 50\,m)$, and a domain with a weaker gradient $(50 - 500\,m)$.

Globally, the simulated profiles are close to the measured ones, except from the 29 of July, the 5 and the 11 of August. As these data come from cruises, the profiles are measured at different locations, therefore other meso-scale processes may have to be taken into account.

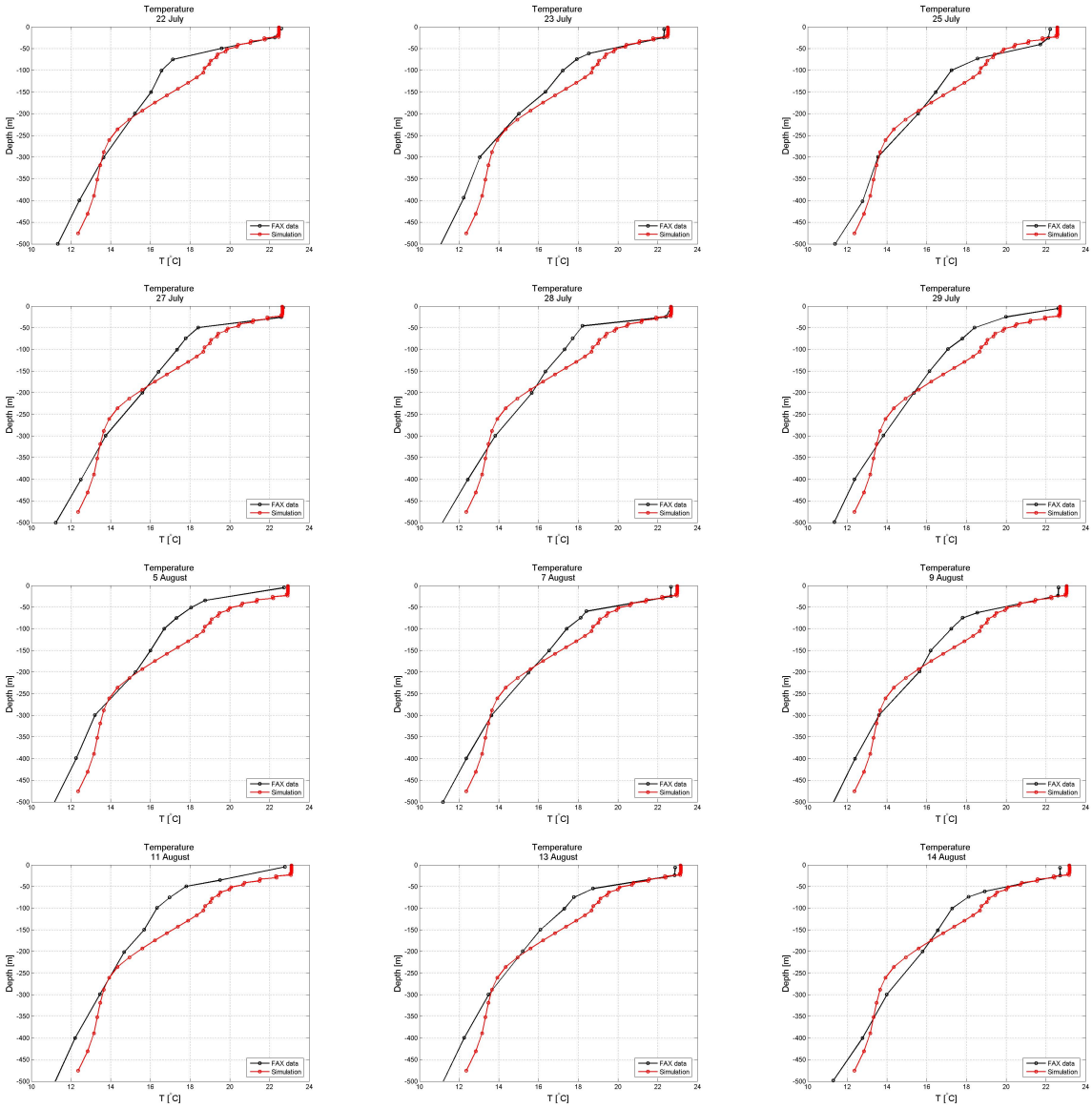

Figure 6.2: *Temperature profiles: in situ data (black line) and simulations results (red line).*

6.1.2 Salinity

We compare three salinity fields on fig. 6.3: model results (a), climatological data (b) and *in situ* measured values (c). Here are the observations we can make:

- an overall good agreement between the model results and the climatological data: the values of salinity are really close in these two case: around 36.4 PSU at -150 meters, 36.2 PSU at -200 meters, etc.
- a weaker (vertical) gradient near the bottom in the simulations case, as shown by the distance between two consecutive isohalines.
- a maximal salinity (36.7 PSU) greater in the case (b) than in the case (a). Once again, we can imagine that this saltier water comes from processes which are not taken into account by the one-dimensional model, *i.e.* the advection.

The most significant difference between the model results and the other figures is the nearly horizontal isohalines. As mentioned previously, no vertical velocity exists, by virtue of the continuity equation and the bottom boundary condition for the velocity. We may think that the implementation of an artificial vertical velocity [2] in the model could yield more realistic results.

The positive vertical gradient of salinity mentioned in section 5.1.2 is confirmed by the climatological and *in situ* data.

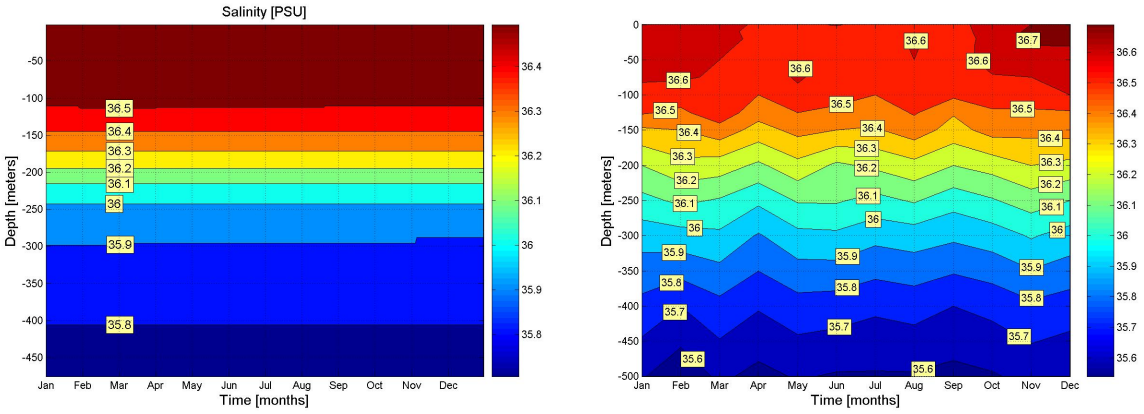

(a) (b)

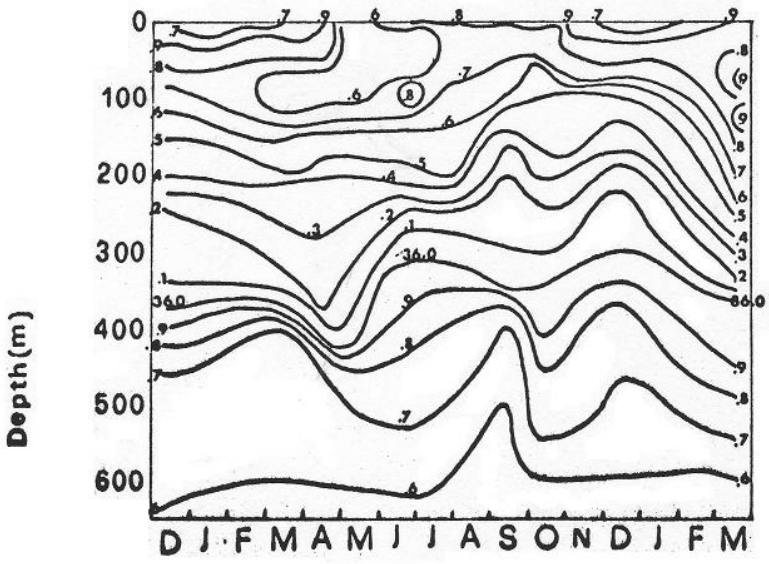

(c)

Figure 6.3: *Salinity field: (a) Model results, (b) NODC (Levitus) WOA Monthly Long Term Mean salinity, (c) measurements (reproduced from [Braun (1976)]).*

Salinity profiles

Measured and computed profiles have the same shape, except from the "peak" structure appearing near 50 meters, which can be attributed to small-scale processes not resolved

[2] In practice this can be done by turning on the UPWELLING cpp key in the source code. Please consult [Penven] for more details.

by the model.

The salinity appears constant in the first 100 meters of the layer, then it decrease from 36.5 to 35.9 PSU at -250 meters. Below 250 meters, the gradient becomes less steep as the salinity decreases of 0.2 PSU over the last 250 meters.

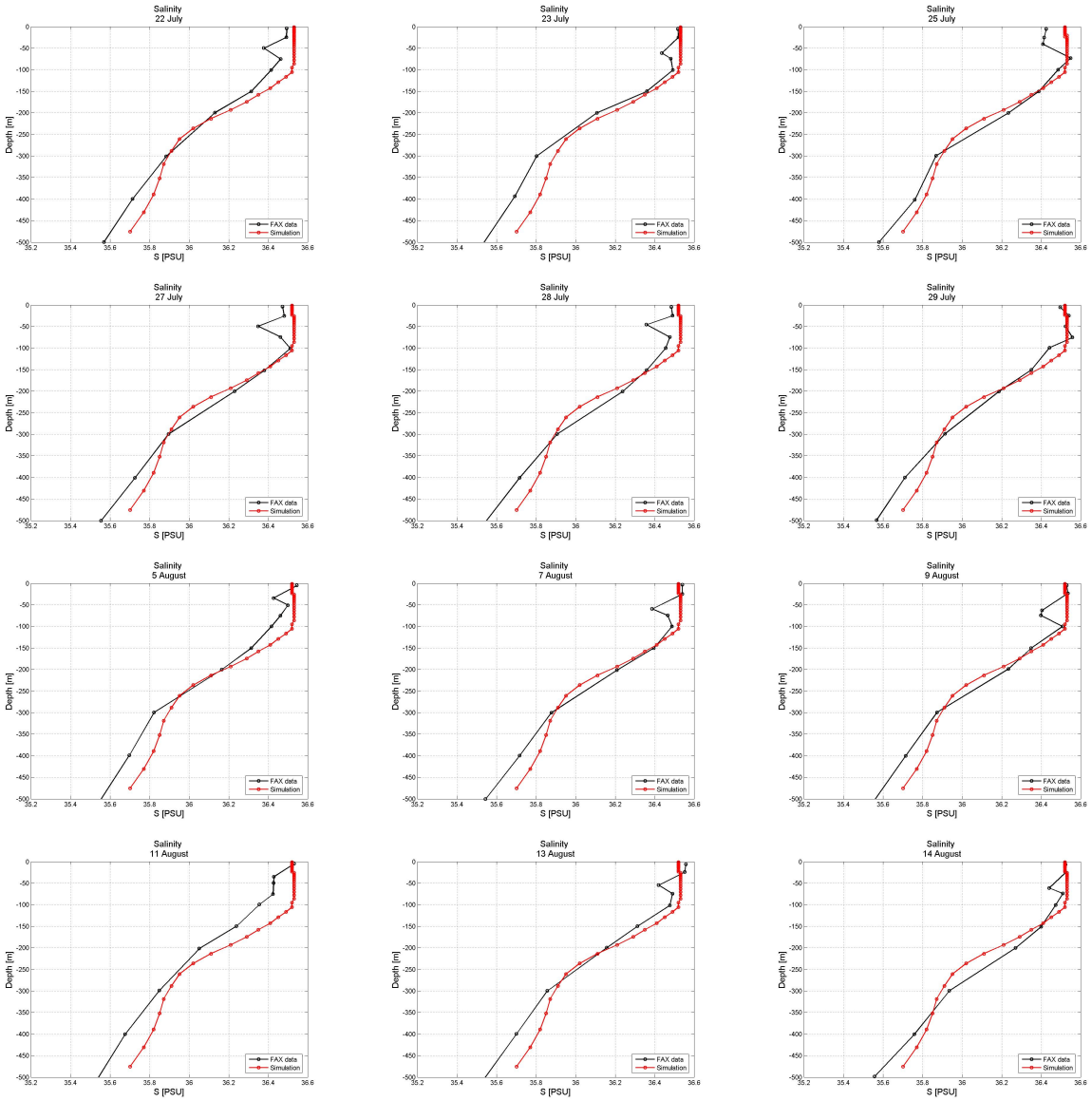

Figure 6.4: *Salinity profiles: in situ data (black line) and simulations results (red line).*

6.1.3 Mixed layer depth

We compared the MLD computed by the model with data from the NODC (Levitus) WOA 1994. In the WOA, the mixed layer depth is computed in two ways: using potential temperature or potential density criterions: as the mixed layer is assumed to have uniform temperature (density) over its thickness, the MLD is defined as the depth where the temperature (density) has a given difference ΔT ($\Delta\rho$) with the surface temperature (density). For example, the depth of the mixed layer can be defined as the depth where the temperature is $0.2°C$ below the surface temperature.

Our MLD is close to the others, especially during the months from May to December.

The largest differences occur from February to April, and can be explained by the fact that our results are averaged from 1993 and 2002, and the WOA mixed layer depth is a long term mean between 1899 and 1992. Furthermore, the ways the MLD is computed are not the same, thus their values will not necessary be the same.

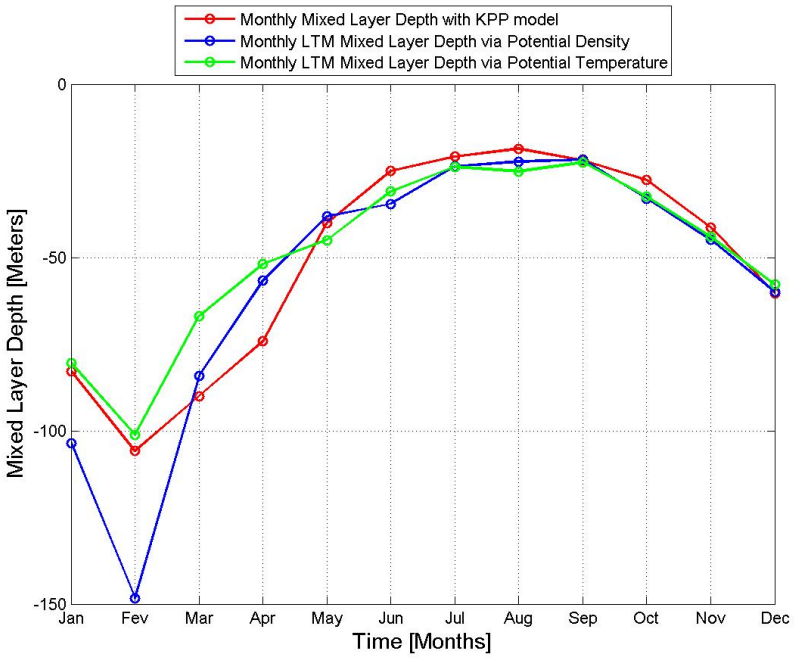

Figure 6.5: *Monthly-averaged MLD: KPP model (red); Levitus 1994 long term mean MLD via potential temperature (green) and via potential density (blue).*

Figs. 6.6 and 6.7 confirm the values obtained for the MLD with measured temperature profiles through the year: around $100\,m$ in winter, $50\,m$ in spring and $25-30\,m$ by the end of September.

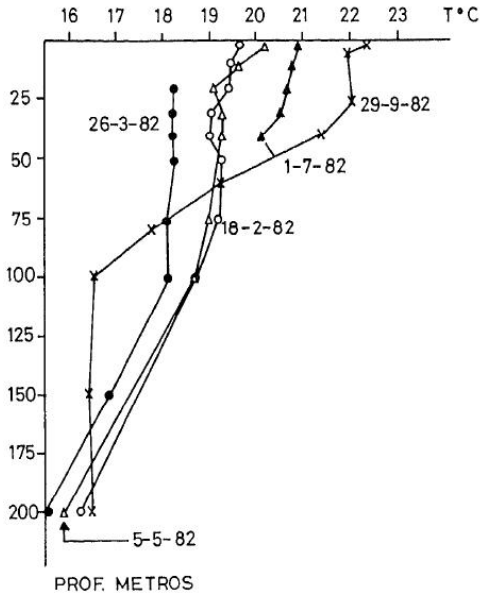

Figure 6.6: *Measured temperature profiles to the south of Gran Canaria (27°42′ north, 15°48′ west) between September 1981 and November 1982 (reproduced from [Hernández-León et al. (1984)]).*

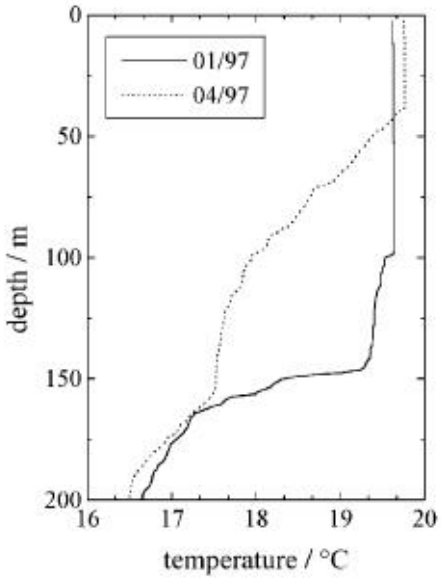

Figure 6.7: *Measured temperature profiles at station ESTOC, north of the Canary Islands (reproduced from [Zielinski et al. (2002)]).*

6.2 Biological variables

6.2.1 Nitrate

As mentioned in the case of salinity, the lines of equal NO_3 are nearly horizontal in our results [fig.6.8(a)], while measurements (fig.6.8(b)) displays marked deformations of these lines. Concerning the quantitative agreement between the two figures, we observe variation between 2 and 14 $mMol\,N_2/m^3$ in the case (a) and between 1 and 15 $mMol\,N_2/m^3$ in the case (b).

Besides the difference in the shape of the lines of equal NO_3, a stronger gradient appears clearly in the measured values, where the nitrate concentration varies from 10 $mMol\,N_2/m^3$ around -450 m to 15 $mMol\,N_2/m^3$ near the bottom. This may comes from a greater sinking velocity in the case (b), bringing more nutrients towards the bottom.

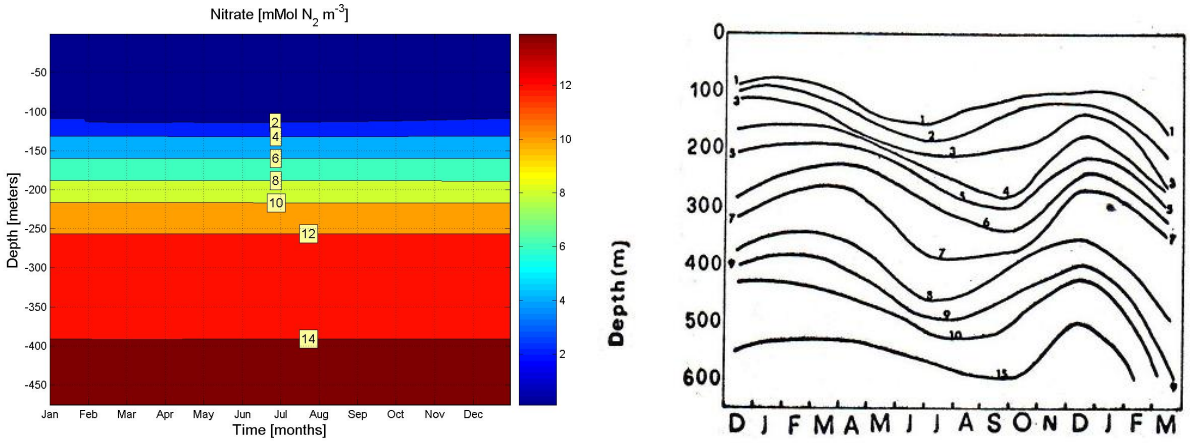

(a) (b)

Figure 6.8: *Nitrate: (a) Model results, (b) measurements (reproduced from [Braun (1976)]).*

Nitrate profile

From fig. 6.9, we can say the curves have the same qualitative aspect: a layer of nearly constant concentration, followed by a nitrocline, which can be broken up into two parts: a strong one ($100 - 300\,m$) and a weaker one ($300\,m$−bottom). The model systematically yields a deeper layer of uniform nitrate concentration than what the measured profiles show.

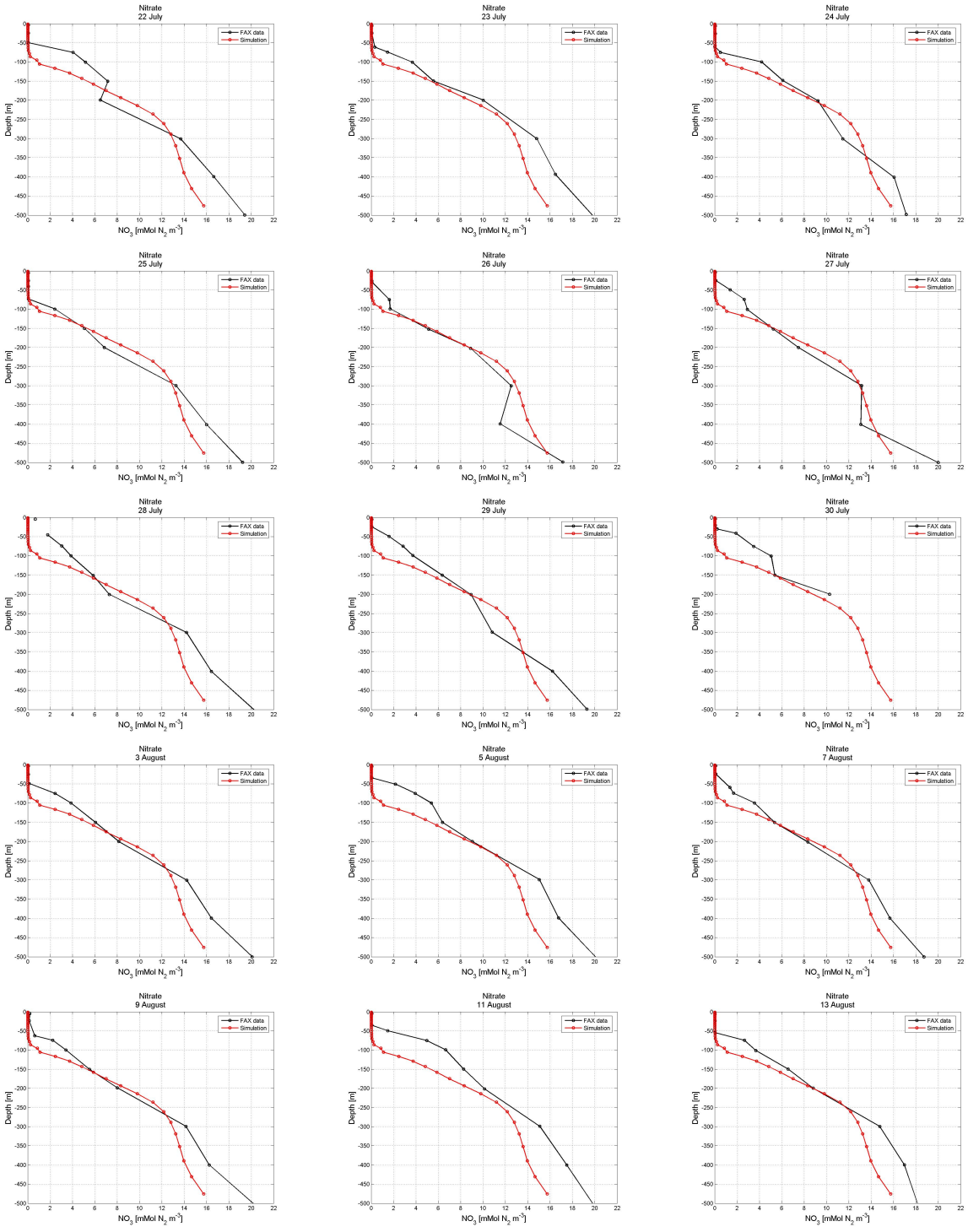

Figure 6.9: *Nitrate profiles: in situ data (black line) and simulations results (red line)*

6.2.2 Chlorophyll a

The chlorophyll is an interesting variable for the validation, because contrary to the others, we did not specify an initial profile for the initialization, we just chose a constant value for the whole water column.

A good agreement with the data for the 6 and 7 August can be observed on fig. 6.10. For the 8 and 9 of August, we observe large differences with *in situ* data, the deep chlorophyll maximum (see section 5.2.6) being much deeper ($-100\,m$) in the simulation than in reality ($-50\,m$).

The strong variations from one day to another cannot be explained by the one-dimensional model, as they may come from the complex circulation pattern of the region, such as cyclonic or anticyclonic eddies, upwelling filament etc (see [Arístegui et al. (1997)] and [Basterretxea et al. (2002)] for more details about the interactions between the hydrodynamic and chlorophyll concentrations).

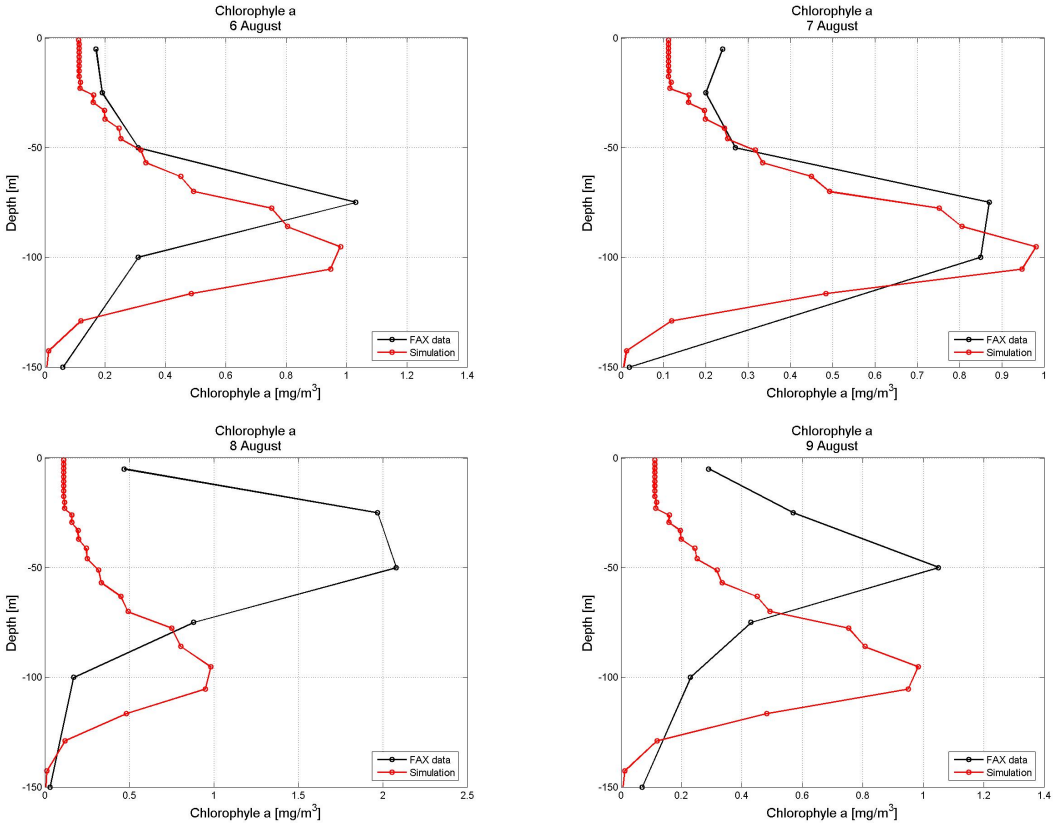

Figure 6.10: *Chlorophylle a profiles.*

6.2.3 Oxygen

We can see numerous differences between the two oxygen fields (fig. 6.11), mainly in the shape of the lines of equal $[O_2]$, but the figure does not allow us to draw qualitative conclusions. We can simply check that the order of magnitude of $[O_2]$, around $5\,mMol\,O_2 m^{-3}$ is compatible between the two figures.

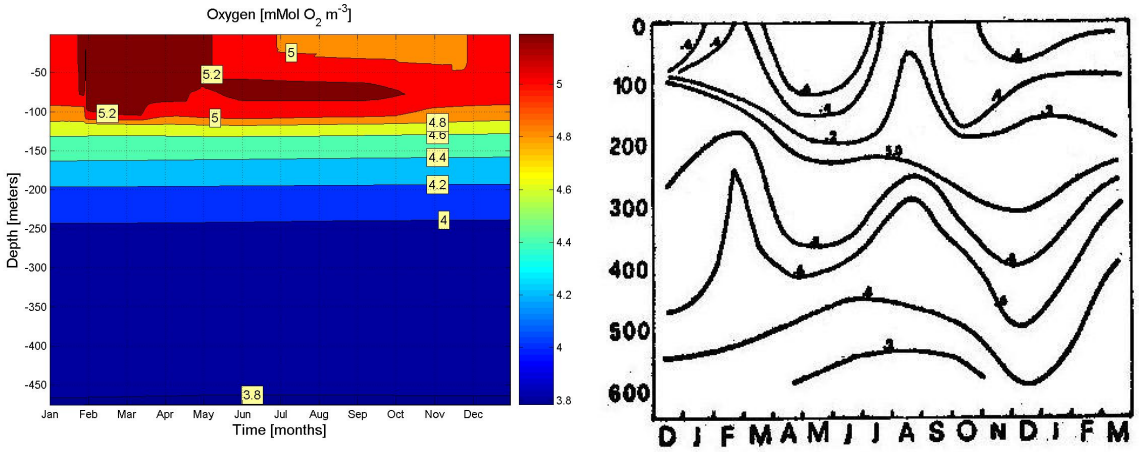

(a) (b)

Figure 6.11: *Oxygen: (a) Model results, (b) measurements (reproduced from [Braun (1976)]).*

Oxygen profiles

The vertical profiles (fig. 6.12) show an interesting qualitative agreement between numerical experiments and reality. The profiles can be decomposed into three parts:

1. in a thin layer near the surface (from 0 to $15-20$ meters), the oxygen concentration is quasi constant.
2. a zone of increase ((from $15-20$ to $80-90$ meters) where the oxygen concentration reaches its maximal value around $5.2\, mMol\, O_2 m^{-3}$.
3. a zone of decrease extending to the bottom.

The explanations regarding this evolution were treated in section 5.2.7.

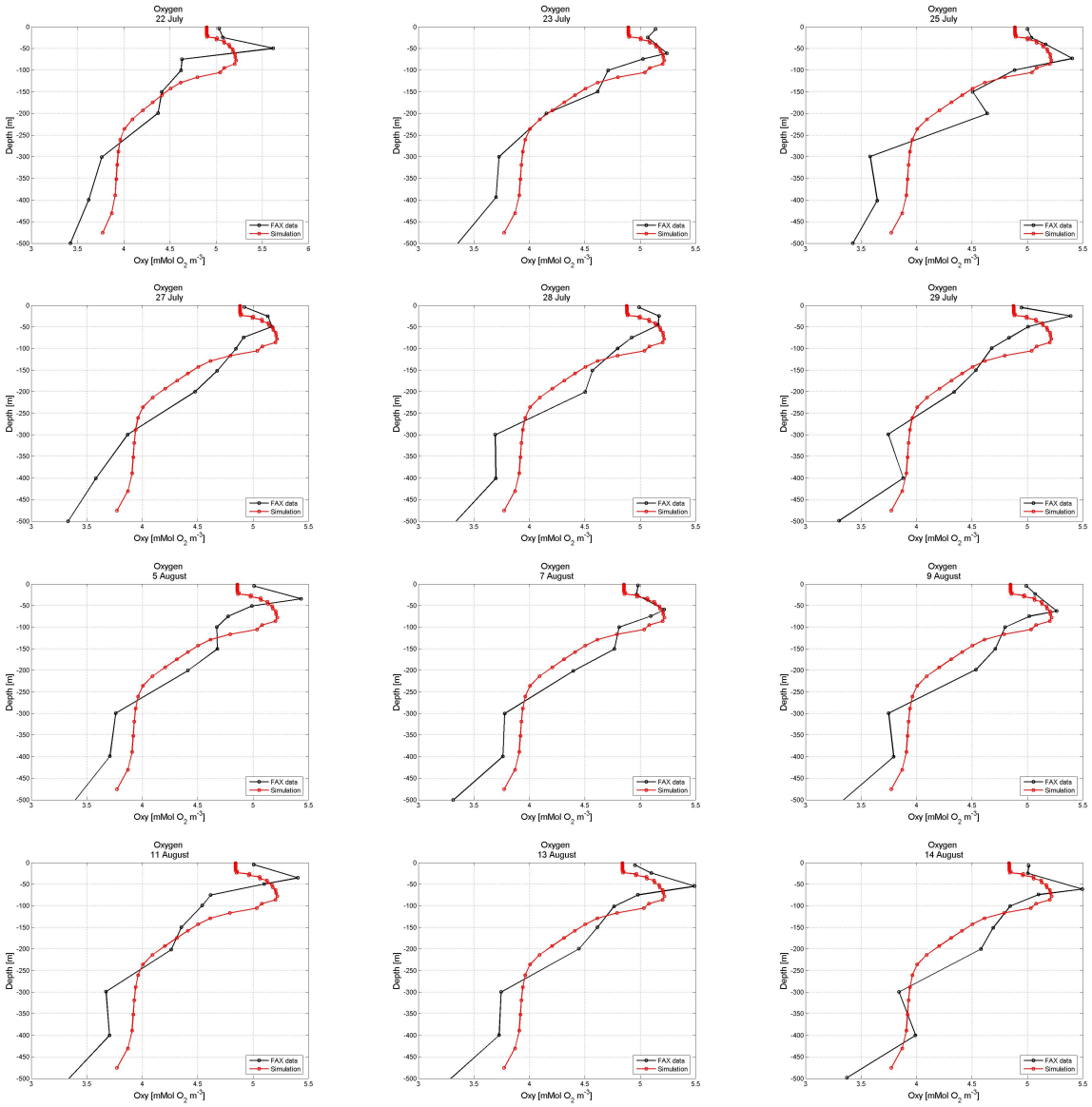

Figure 6.12: *Oxygen profiles.*

Summary

The model is validated by comparing its results with fields taken either from climatic database or from *in situ* data.

Overall, our results have always the same order of magnitude than the observed and the climatic values, and the vertical profiles have similar shapes. We may distingush two main kinds of differences:

- differences in stratification: in the layer between $-200\,m$ and the bottom, the model systematically yields fields (temperature, salinity, nitrate, oxygen) with weaker stratification than in reality.
- differences in the form of the iso-lines: real data clearly shows vertical deformation of the iso-lines (isotherms, isohalines, iso-NO_3 and iso-oxygen). Those deformations cannot be reproduced by the present one-dimensional model, for the vertical component of the velocity is always null, according to the continuity equation.

Vertical profiles of chlorophyll are in agreement with the *in situ* measurements, and the concentrations values are conform to the ones found in the litterature.

CONCLUSIONS

General conclusion

To conclude this work, we can say that we were successful in achieving our major goal, which was modelling the annual cycles of phytoplankton, zooplankton and nutrients to the south of Gran Canaria Island. Every step of the modelling process was covered and the main objectives were met, namely:

1. the understanding and the running of the ROMS 1D model,
2. the gathering of climatological data and vertical profiles needed for forcing and initialization, respectively,
3. the testing with idealized forcing and the sensitivity analysis,
4. the application of the model to the region of interest,
5. the discussion and validation of results.

Moreover, the Sverdrup's theory was applied successfully to interpret the numerical results, despite the numerous approximations made.

Results

Globally, we can say that the model provides satisfying results, according to the following facts:

- the annual evolution of the mixed layer was correctly reproduced, both qualitatively and quantitatively;
- the spatio-temporal structures of the physical fields (temperature and salinity) were similar to the oceanic data for this region;
- the late-winter bloom was well simulated and appeared clearly in the phytoplankton annual field;
- the maximum chlorophyll depth was similar to the *in situ* measurements;
- each variable of the model was found to have values close to the data we could find for the region.

Model efficiency

There are numerous one-dimensional models available, so we may ask ourselves what distinguish the ROMS model with the other ones. We cannot really speak about "weak points" or "strong points" of a model, because the way a model works depends on the purpose that the scientists who create it strive for. We should rather say that a particular model is adapted or not adapted to our study.

In the present case, our needs for modelling annual cycles were met by ROMS model. We can informally mention as "weaker points" that there is only one turbulence closure scheme available, while some models [3] offer several possibilities, and also that the monthly forcing may sometimes be insufficient when we need to work on shorter time scales.

Perspectives and enhancements

After having devoted several months on this project, we have noticed some aspects that need to be explored or detailed: here are some suggestions for future works about the same topic:

- modelling the same cycles, but at different location, for example to the north of Gran Canaria, in order to examine the influence of the atmospheric forcing on the physical and biological variables;
- to make adjustment of the biological model by searching more realistic parameters in the litterature;
- to include the upwelling forcing, which creates artificial vertical velocities and could bring more realistic results;
- to use a more elaborated model for the compensation depth. This depth should depend on the phytoplankton species present in the area.

To put the final point to this work, I would like to express again my gratitude to all the people who contribute directly or indirectly to the achievement of this project, which allowed me to make significant progress in physical oceanography, ocean modelling, as well as in English and Spanish. *Gracias a todos.*

[3] GOTM (General Ocean Turbulence Model) for example.

Appendix A

Biological model formulation

This part is dedicated to the biological model which is effectively used: the equations are made explicit, as well as the source/ sink terms. More details can be found in the related publications. In the following, [...] represents variables concentrations, $Q_{...}$ stands for the source/sink terms and $K_{...}$ are the half-saturation constants of the Michaelis-Menten equations. The vertical sinking is symbolized by L_{vs}. Meanings of the other symbols are made explicit in tab. A.1.

A.1 Differential equations for the nitrogen cycle

A.1.1 Nitrate

$$\frac{\partial[NO_3]}{\partial t} = -t_{PPmax} Q_{NP}[Phyto] + Q_{nitr}[NH4] \tag{A.1}$$

with Q_{NP}, the new production term (production driven by nitrate) and Q_{nitr}, the term which takes into account the conversion of ammonium into nitrate.

$$t_{PPmax} = \frac{V_p \alpha \, PAR \, \theta}{\sqrt{V_p^2 + \alpha^2 \theta^2 PAR^2}},$$
$$V_p = 0.59 \, 1.066^T$$

where PAR, is the photosynthetically active radiation, θ the chlorophyll to carbon ratio and α the initial slope of the P-I curve.

A.1.2 Ammonium

$$\begin{aligned} \frac{\partial[NH4]}{\partial t} &= -t_{PPmax} Q_{RP}[Phyto] - Q_{nitr}[NH4] + t_{Zbmet} Q_{excr}[Zoo] \\ &+ t_{SDremin}[SDet] + t_{LDremin}[LDet], \end{aligned} \tag{A.2}$$

where Q_{RP} is the recycled production term (production driven by ammonium), Q_{excr} the term that parameterizes the excretion, t_{Zbmet} the zooplankton specific excretion rate, $t_{SDremin}$ and $t_{LDremin}$, the rates of small and large detritus breakdown to ammonium, respectively.

A.1.3 Phytoplankton

$$\begin{aligned}\frac{\partial[Phyto]}{\partial t} &= t_{PPmax}(Q_{NP}+Q_{RP})\,[Phyto] - t_{Pmort}[Phyto] - Q_{coag}[Phyto] \\ &- Q_{graze}[Zoo] + L_{vs} \end{aligned} \tag{A.3}$$

with Q_{coag}, the coagulation term, which is function of an aggregation rate between phytoplankton and small detritus, Q_{graze}, the grazing term, t_{Pmort} the rate of phytoplankton mortality to small detritus and L_{vs} the vertical sinking term.

A.1.4 Zooplankton

$$\frac{\partial[Zoo]}{\partial t} = Q_{graze}AE\,[Zoo] - t_{Zbmet}[Zoo] - t_{Zmort}[Zoo] - Q_{excr}[Zoo] \tag{A.4}$$

where AE is the zooplankton assimilation efficiency, t_{Zmort} is the zooplankton quadratic mortality to detritus and Q_{excr} is the ammonium production term due to excretion.

A.1.5 Small detritus

$$\begin{aligned}\frac{\partial[SDet]}{\partial t} &= Q_{graze}(1-AE)\,[Zoo] + t_{Pmort}[Phyto] + t_{Zmort}[Zoo] \\ &- t_{coag}([SDet]+[Phyto])\,[SDet] - t_{SDremin}[SDet] \\ &+ L_{vs}. \end{aligned} \tag{A.5}$$

A.1.6 Large detritus

$$\begin{aligned}\frac{\partial[LDet]}{\partial t} &= t_{coag}.([SDet]+[Phyto])([SDet]+[Phyto]) \\ &- t_{LDremin}.[LDet] + L_{vs}. \end{aligned} \tag{A.6}$$

A.2 Source terms

A.2.1 New production

$$Q_{NP} = \frac{([NO_3]/K_{NO_3})\,I_{NH_4}}{1+[NO_3]/K_{NO_3}}, \tag{A.7}$$

with

$$I_{NH_4} = \frac{1}{1+[NH4]/K_{NH_4}},$$

where K_{NO_3} and K_{NH_4} are the half-saturation constants for phytoplankton uptakes of nitrate and ammonium, respectively.

A.2.2 Regenerated production

$$Q_{RP} = \frac{[NH_4]/K_{NH_4}}{1 + [NH_4]/K_{NH_4}}. \tag{A.8}$$

A.2.3 Nitrification

$$Q_{nitr} = t_{nitri}\left(1 - \max\left[0, \frac{PAR - I_{thNH_4}}{D_{p5NH_4} + PAR - 2\,I_{thNH_4}}\right]\right),$$

with t_{nitri}, the nitrification rate (NH_4 to NO_3), I_{thNH_4}, the threshold PAR for nitrification inhibition, and D_{p5NH_4}, the 0.5 dose for nitrification inhibition.

A.2.4 Grazing

$$Q_{graze} = t_{Zgraze}\frac{[Phyto]}{K_P + [Phyto]}$$

where t_{Zgraze} is the zooplankton specific maximum grazing rate and K_P is the zooplankton half-saturation constant for ingestion.

A.2.5 Excretion

$$Q_{excr} = Q_{graze} r_{C:N,phyto} AE\left(\frac{1}{r_{C:N;phyto}} - \frac{GGE}{AE\, r_{C:N;zoo}}\right),$$

where $r_{C:N,phyto}$ and $r_{C:N,zoo}$ are the carbon to nitrogen ratios for phytoplankton and zooplankton, respectively, and GGE is the zooplankton gross growth efficiency.

A.2.6 Respiration

$$Q_{resp} = Q_{graze} r_{C:N;phyto}(AE - GGE).$$

A.3 Additional equations

A.3.1 Chlorophyll

$$\frac{\partial\theta}{\partial t} = t_{PPmax}(Q_{NP} + Q_{RP})\left(\frac{\theta_m V_p (Q_{NP} + Q_{RP})}{\sqrt{V_p^2 + \alpha^2\theta^2 PAR^2}} - \theta\right) + L_{vs}, \tag{A.9}$$

where θ_m is the maximum cellular chlorophyll to carbon ratio.

A.3.2 Oxygen

$$\begin{aligned}\frac{\partial[O_2]}{\partial t} &= t_{PPmax}(Q_{NP} r_{O_2:NO_3} + Q_{RP} r_{O_2:NH_4})[Phyto] - 2\,Q_{nitr}[NH4] \\ &- (t_{Zbmet} r_{O_2:NH_4} + Q_{resp})[Zoo] - (t_{SDremin}[SDet] + t_{LDremin}[LDet]) r_{O_2:NH_4} \\ &+ Q_{ge}(O_{2,sat} - O_2)\end{aligned} \tag{A.10}$$

where $r_{O_2:NO_3}$ and $r_{O_2:NH_4}$ are ratios to convert nitrate and ammonium concentrations into oxygen concentration, respectively.

Gas exchange rate of oxygen:

$$Q_{ge;O2} = \frac{K_{vO_2}}{\Delta z_N}$$

where Δz_N is the height of the top cell and K_{vO_2} the gas transfer coefficient, calculated by

$$K_{vO_2} = 0.31\, u^2 \sqrt{\frac{660}{Sc}}$$

u is the average wind speed (in cm/h). By default, the Schmidt number Sc is calculated after [Wanninkhof (1992)].

$$Sc = 1953.4 - 128\, T + 3.9918\, T^2 - 0.050091\, T^3$$

The saturation concentration of oxygen is calculated by

$$O_{2,sat} = \frac{e^A.\rho}{22.9316}$$

with

$$\begin{aligned} A &= -177.7888 + \frac{25559.07}{T_K} + 146.4813 \ln\left(\frac{T_K}{100}\right) - 22.204 \frac{T_K}{100} \\ &+ S\left[-0.037362 + \frac{T_K}{100}\left(0.016504 - 0.0020564 \frac{T_K}{100}\right)\right] \end{aligned}$$

with ρ the density, S the salinity and T_K the absolute temperature.

A.4 Parameters values

Parameters values for the oceanic and coastal cases are shown in tab. A.1.

Parameter	Symbol	Values		Unit
		Ocean	Coast	
Light attenuation due to sea water	k_{water}	0.04	0.04	m^{-1}
Light attenuation by chlorophyll a	k_{Chla}	0.025	0.025	$(m^2\, mg\, Chla)^{-1}$
Initial slope of the $P-I$ curve	α	5.00	1.00	$mg\, C(mg\, Chla\, W\, m^{-2} d)^{-1}$
$C:N$ ratio for phytoplankton	$r_{C:N;phyto}$	6.625	6.625	$mMol\, C(mMol N)^{-1}$
Maximum Cellular Chlor to C Ratio	θ_m	0.053	0.053	$mg\, Chla : mg\, C$
Inverse half-saturation for phytoplankton NO_3 uptake	K_{NO_3}	1/0.5	1/0.5	$1/(mMol N m^3)$
Inverse half-saturation for phytoplankton NH_4 uptake	K_{NH_4}	1/0.1	1/0.5	$1/(mMol N m^3)$
Phytoplankton mortality to small detritus rate	t_{Pmort}	0.07	0.07	d^{-1}
Zooplankton-specific maximum grazing rate	t_{Zgraze}	0.75	0.75	d^{-1}
Zooplankton assimilation efficiency	AE	0.75	0.75	$--$
Zooplankton gross growth efficiency	GGE	0.65	0.65	$--$
Zooplankton half-saturation constant for ingestion	Z_P	1.00	1.00	$mMol\, N\, m^3$
Zooplankton specific excretion rate	t_{Zbmet}	0.10	0.10	d^{-1}
Zooplankton quadratic mortality to detritus	t_{Zmort}	0.10	0.10	$d^{-1}(mMol\, N\, m^3)^{-1}$
Small Detrital breakdown to NH_4 rate	$t_{SDremin}$	0.1	0.1	d^{-1}
Specific (Per unit $Phyto$+$SDet$) aggregation rate	t_{coag}	0.005	0.005	$(mMol\, N\, m^3)^{-1} d^{-1}$
Specific rate of large detritus recycling to NH_4	$t_{LDremin}$	0.1	0.05	d^{-1}
Sinking velocity for small detritus	w_{SD}	0.1	1.0	$m\, d^{-1}$
Sinking velocity for large detritus	w_{LD}	10.0	10.0	$m\, d^{-1}$
Sinking velocity for phytoplankton	w_{Phyto}	0.1	0	$m\, d^{-1}$
Sinking velocity for chlorophyll a	w_{Chla}	0.1	0	$m\, d^{-1}$
Oxidation of NH_4 to NO_3 (nitrification)	t_{nitri}	0.1	0.1	d^{-1}

Table A.1: *Parameters of the biological model.*

Bibliography

[Arístegui et al. (1994)] Arístegui, J., P. Sangrà, S. Hernández-León, M. Cantón, A. Hernández-Guerra, J. L. Kerling (1994), Island-induced eddies in the Canary Islands, *Deep-Sea Res. I*, **41**, 1509-1525.

[Arístegui et al. (1997)] Arístegui, J., P. Tett, A. Hernández-Guerra, G. Basterretxea, M. F. Montero, K. Wild, P. Sangrà, S. Hernández-León, M. Cantón, J. García-Braun, M. Pacheco, E. D. Barton (1997), The influence of island-generated eddies on chlorophyll distribution: a study of mesoscale variation around Gran Canaria, *Deep-Sea Res. I*, **44**, 71-96.

[Arístegui et al. (2001)] Arístegui, J., S. Hernández-León, M. F. Montero, M. Gomez (2001), The seasonal planktonic cycle in coastal waters of the Canary Islands, *Sci. Mar.*, **65**, 51-58.

[Arístegui et al. (2004)] Arístegui, J., E. D. Barton, P. Tett, M. F. Montero, M. García-Muñoz, G. Basterretxea, A.-S. Cussatlegras, A. Ojeda , D. de Armas (2004), Variability in plankton community structure, metabolism, and vertical carbon fluxes along an upwelling filament (Cape Juby, NW Africa), *Prog. Oceanogr.*, **62**, 95-113.

[Barton et al. (1998)] Barton, E. D., J. Arístegui, P. Tett, M. Cantón, J. García-Braun, S. Hernández-León, L. Nykjaer, C. Almeida, J. Almunia, S. Ballesteros, G. Basterretxea, J. Escánez, L. García-Weill, A. Hernández-Guerra, F. López-Laatzen, R. Molina, M. F. Montero, E. Navarro-Pérez, J. M. Rodríguez, K. van Lenning, H. Vélez, K. Wild (1998), The transition zone of the Canary Current upwelling region, *Prog. Oceanogr.*, **41** 455-504.

[Barton et al. (2004)] Barton, E. D., J. Arístegui, P. Tett, E. Navarro Pérez (2004), Variability in the Canary Islands area of filament-eddy exchanges, *Prog. Oceanogr.*, **62**, 71-94.

[Basterretxea et al. (2002)] Basterretxea, G., E. D. Barton, P. Tett, P. Sangrà, E. Navarro-Perez, J. Arístegui (2002), Eddy and deep chlorophyl maximum response to wind-shear in the lee of Gran Canaria, *Deep-Sea Res. I*, **49**, 1087-1101.

[Braun (1976)] Braun, J. G. (1976), Production Studies in Canary Islands waters. I. Hydrography, nutrients and primary production, *International Council for the Exploration of the Sea*, 1-10.

[Colella and Woodward (1984)] Colella, P., P. R. Woodward (1984), The piecewise parabolic method (PPM) for gas-dynamical simulations, *J. Comp. Phys.*, **54**, 174-201.

[Dugdale and Goering (1967)] Dugdale, R. C., J. J. Goering (1967), Uptake of new and regenerated forms of nitrogen in primary production, *Limnol. Oceanogr.*, **12**, 196-206.

[Fasham et al. (1990)] Fasham, M. J. R., H. W. Ducklow, S. M. McKelvie (1990), A nitrogen-based model of plankton dynamics in the oceanic mixed layer, *J. Geophys. Res.*, **48**, 591-639.

[Frost (1993)] Frost, B. W. (1993), A modeling study of processes regulating plankton standing stock and production in the open subarctic Pacific Ocean, *Prog. Oceanogr.*, **32**, 17-56.

[García-Muñoz et al. (2004)] García-Muñoz, M., J. Arístegui, M. F. Montero, E. D. Barton (2004), Distribution and transport of organic matter along a filament-eddy system in the Canaries - NW Africa coastal transition zone region, *Prog. Oceanogr.*, **62**, 115-129.

[Garwood (1977)] Garwood, R. W. (1977), An oceanic mixed layer model capable of simulating cyclic states, *J. Phys. Oceanogr.*, **7**, 455-471.

[Haney (1971)] Haney, R. L. (1971), Surface thermal boundary conditions for ocean circulation models, *J. Phys. Oceanogr.*, **1**, 241-248.

[Hernández-León et al. (1984)] Hernández-León, S., O. Llinás, J. G. Braun (1984), Nota sobre la variación de la biomasa del mesozooplancton en aguas de Canarias, *Inv. Pesc.*, **48**, 495-508.

[Jackett and McDougall (1995)] Jackett, D. R., T. J. McDougall (1995), Minimal Adjustment of Hydrostatic Profiles to Achieve Static Stability, *J. Atmos. Oceanic Techn.*, **12**, 381-389.

[Jones and Launder (1972)] Jones, W. P., B. E. Launder (1972), The prediction of laminarization with a two-equation model of turbulence, *Int. J. Heat Mass Transfer*, **15**, 301-314.

[Kanamitsu et al. (2002)] Kanamitsu, M., W. Ebisuzaki, J. Woollen, S.-K. Yang, J. J. Hnilo, M. Fiorino, G. L. Potter (2002), NCEP-DEO AMIP-II Reanalysis (R-2), *Bul. of the Atmos. Met. Soc.*, 1631-1643.

[Killworth et al. (2000)] Killworth, P. D., D. A. Smeed, A. J. George Nurser (2000), The effects on ocean models of relaxation toward observations at the surface, *J. Phys. Oceanogr.*, **30**, 160-174.

[Kolmogorov (1942] Kolmogorov, A.N., (1942), Equations of turbulent motion of an incompressible fluid, *Izvestia Acad. Sci., USSR; Phys.*, **6** (1-2), 56-58.

[Large et al. (1994)] Large, W. G., J. C. McWilliams, S. C. Doney (1994), Oceanic vertical mixing: a review and a model with a nonlocal boundary layer parameterization, *Rev. Geophys.*, **32**, 363-403.

[Marchesiello et al. (2001)] Marchesiello, P., J. C. McWilliams, A. Shchepetkin (2001), Open boundary conditions for long-term integration of regional oceanic models, *Ocean Modelling*, **3** 1-20.

[Mellor and Yamada (1974)] Mellor, G. L., T. Yamada (1974), A hierarchy of turbulence closure models for planetary boundary layers, *Journal of the Atmospheric Sciences*, **31**, 1791-1806.

[Moisan and Hofman (1996)] Moisan, J. R., E. E. Hofmann (1996), Modeling nutrient and plankton processes in the California coastal transition zone. 1. A time- and depth-dependent model, *J. Geophys. Res.*, **101**, 22,647-22,676.

[Monterey and Levitus (1997)] Monterey, G. I., S. Levitus (1997), Climatological cycle of mixed layer depth in the world ocean, *U.S. Gov. Printing Office*, NOAA NESDIS, 5pp.

[Paulson and Simpson (1977)] Paulson, C. A., J. J. Simpson (1977), Irradiance measurements in the upper ocean, *J. Phys. Oceanogr.*, **7**, 952-956.

[Pelegrí and Sangrà (1998)] Pelegrí, J. L., P. Sangrà (1998), A mechanism for layer formation in stratified geophysical flows, *J. of Geophys. Res.*, **103**, 30,679-30693.

[Pelegrí et al. (2005a)] Pelegrí, J. L. , J. Arístegui, L. Cana, M. González-Dávila, A. Hernández-Guerra, S. Hernández-León, A. Marrero-Díaz, M. F. Montero, P. Sangrà, M. Santana-Casiano (2005), Coupling between the open ocean and the coastal upwelling region off northwest Africa: water recirculation and offshore pumping of organic matter, *J. Mar. Syst.*, **54**, 3-37.

[Pelegrí et al. (2005b)] Pelegrí, J. L., A. Marrero-Díaz, A. Ratsimandresy, A. Antoranz, J. Cisneros-Aguirre, C. Gordo, D. Grisolía, A. Hernández-Guerra, I. Laíz, A. Martínez, G. Parrilla, P. Pérez-Rodríguez, A. Rodríguez-Santana, P. Sangrà (2005), Hydrographic cruises off northwest Africa: the Canary Current and the Cape Ghir region, *J. Mar. Syst.*, **54**, 39-63.

[Penven] Penven, P., 1D ROMS Model documentation, available at `http://www.brest.ird.fr/personnel/ppenven/roms1d/`.

[Pérez et al. (2001)] Pérez, F. F., L. Mintrop, O. Llinás, M. Glez-Dávila, C. G. Castro, M. Alvarez, A. Körtzinger, M. Santana-Casiano, M. J. Rueda, A. F. Ríos (2001), Mixing analysis of nutrients, oxygen and inorganic carbon in the Canary Islands region, *J. Mar. Syst.*, **28**, 183-201.

[Plattner et al. (2005)] Plattner, G.-K., N. Gruber, H. Frenzel, J. C. McWilliams (2005), Decoupling marine export production from new production, *Geophys. Res. Let.*, **32**, L11612.

[Price et al. (1986)] Price, J. F., R. F. Weller, R. Pinkel (1986), Diurnal cycling: Observations and models of the upper ocean response to diurnal heating, cooling and wind mixing, *J. Geophys. Res.*, **91**, 8411-8427.

[Ratsimandresy et al. (2001)] Ratsimandresy, A. W., J. L. Pelegrí, A. Marrero-Díaz, A. Hernández- Guerra, A. Antoranz, A. Martínez (2001), Seasonal variability of the upper warmwatersphere in the Canary Basin, *Sci. Mar.*, **65** (S1), 251-258.

[Reynolds et al. (2002)] Reynolds, R. W., N. A. Rayner, T. M. Smith, D. C. Stokes, W. Wang (2002), An improved in situ and satellite SST analysis for climate, *J. Climate*,, **15**, 1609-1625.

[Shchepetkin and McWilliams (2005)] Shchepetkin, A., J. C. McWilliams (2005), The Regional Oceanic Modeling System: A split-explicit, free-surface, topography-following-coordinate ocean model, *Ocean Modelling*, **9**, 347-404.

[Siegel et al (2001)] Siegel, D. A., S. C. Doney, J. A. Yoder (2001), The North Atlantic spring phytoplankton bloom and Sverdrup's critical depth hypothesis, *Science*, **296**, 730-733.

[Sverdrup (1953)] H. U. Sverdrup (1953), On conditions for the vernal blooming of phytoplankton, *J. Cons. Perm. Int. Explor. Mer.*, **18**, 287-295.

[Tett et al. (2002)] Tett, P., J. Arístegui, D. Barton, G. Basterretxea, J. D. De Armas, J. E. Escánez, S. Hernández León, L. M. Lorenzo, N. Montero (2002), Steady-state DCM dynamics in Canaries waters, *Deep-Sea Res. II*, **49**, 3543-3559.

[Uppala et al. (2005)] Uppala, S. M., P. W. Kallberg, A. J. Simmons, U. Andrae, V. da Costa Bechtold, M. Fiorino, J. K. Gibson, J. Haseler, A. Hernandez, G. A. Kelly, X. Li, K. Onogi, S. Saarinen, N. Sokka, R. P. Allan, E. Andersson, K. Arpe, M. A. Balmaseda, A. C. M. Beljaars, L. van de Berg, J. Bidlot, N. Bormann, S. Caires, F. Chevallier, A. Dethof, M. Dragosavac, M. Fisher, M. Fuentes, S. Hagemann, E. Holm, B. J. Hoskins, L. Isaksen, P. A. E. M. Janssen, R. Jenne, A. P. McNally, J.-F. Mahfouf, J.-J. Morcrette, N. A. Rayner, R. W. Saunders, P. Simon, A. Sterl, K. E. Trenberth, A. Untch, D. Vasiljevic, P. Viterbo, J. Woollen (2005), The ERA-40 re-analysis, *Quart. J. R. Meteorol. Soc.*, **131**, 2961-3012.

[Wanninkhof (1992)] Wanninkhof, R. (1992), Relationship between gas exchange and wind speed over the ocean, *J. Geophys. Res.*, **97**, 7373-7381.

[Warner et al. (2005)] Warner, J. C., C. R. Sherwood, H. G. Arango, R. P. Signell (2005), Performance of four turbulence closure models implemented using a generic length scale method, *Ocean Modelling*,, **8**, 81-113.

[Yu et al. (2004)] Yu, L., R. A. Weller, B. Sun (2004), Improving latent and sensible heat flux estimates for the Atlantic Ocean (1988-1999) by a synthesis approach, *J. Clim.*, **17**, 373-393.

[Yu and Weller(2006)] Yu, L., R. A. Weller (2006), Objectively analyzed air-sea heat fluxes for the global oceans. To be submitted.

[Zhang et al. (2004)] Zhang, Y-C., W. B. Rossow, A. A. Lacis, V. Oinas, M. I. Mishchenko (2004), Calculation of radiative fluxes from the surface to top of atmosphere based on ISCCP and other global data sets: Refinements of the radiative transfer model and the input data, *J. Geophys. Res.*, **109**, D19105.

[Zielinski et al. (2002)] Zielinski, O., O. Llinás, A. Oschlies, R. Reuter (2002), Underwater light field and its effect on a one-dimensional ecosystem model at station ESTOC, north of the Canary Islands, *Deep-Sea Res. II*, **49**, 3529-3542.

Books

[Cognetti (2001)] Cognetti, G., M. Sarà and G. Magazzù, *Biología marina*, Barcelona: Ariel Ciencia, 2001.

[Falkowski (1992)] Falkowski, P. G., and A. D. Woodhead, *Primary productivity and biogeochemical cycles in the sea*, New York: Plenum, 1992.

[Jerlov (1968)] Jerlov, N. G., *Optical oceanography*, Elsevier, 1968.

[Kantha (2000)] Kantha, L. H., C. A. Clayson, *Small Scale Processes in Geophysical Fluid Flows*, San Diego: Academic Press, 2000.

[Lalli (1993)] Lalli, C. M., T. R. Parsons, *Biological oceanography, an introduction*, Oxford: Pergamon Press, 1993.

[Niiler (1977)] Niiler, P. P., E. B. Kraus, *One-dimensional models*, *Modelling and Prediction of the Upper Layers of the Ocean*, E. B. Kraus, Ed., Pergamon Press, 1977.

[Nybakken (2001)] Nybakken, J. W., *Marine Biology, An Ecological Approach*, San Francisco: Benjamin Cummings, 2001.

[Parsons (1984)] Parsons, T. R., M. Takahashi, B. Hargrave, *Biological oceanographic processes*, Oxford, New York: Pergamon Press, 1984.

Thesis

[Sangrà (1995)] Sangrà, P. (1995), Disturbance of a geophysical flow by an obstacle: application to the island of Gran Canaria, doctoral thesis, University of Las Palmas de Gran Canaria.

Websites

ROMS model

http://www.atmos.ucla.edu/cesr/ROMS_page.html
http://quercus.igpp.ucla.edu/research/projects/roms/
http://marine.rutgers.edu/po/index.php?model=roms
http://www.brest.ird.fr/personnel/ppenven/roms1d/

Climatic data

- ◇ ECMWF 40 Years Re-Analysis, monthly means:
  [Uppala et al. (2005)],
  http://data.ecmwf.int/data/d/era40_mnth/
- ◇ NOAA Optimum Interpolation (OI) Sea Surface Temperature (SST) V2:
  [Reynolds et al. (2002)],
  http://www.cdc.noaa.gov/cdc/data.noaa.oisst.v2.html
- ◇ NCEP/NCAR Reanalysis Monthly Means and Other Derived Variables:
  [Kanamitsu et al. (2002)],
  http://www.cdc.noaa.gov/cdc/data.ncep.reanalysis.derived.html#surface_gauss
- ◇ Objectively Analysed Air-Sea Fluxes (OAFlux) for the Global Oceans:
  [Yu and Weller(2006)], [Yu and Weller(2006)], [Zhang et al. (2004)],
  http://oaflux.whoi.edu/

Miscellaneous

- American Meteorological Society Glossary of Meteorology:
  http://amsglossary.allenpress.com/glossary
- Unesco Environment and development in coastal regions and in small islands:
  http://www.unesco.org/csi/pub/source/rs10.htm

List of Figures

List of Tables